Fall 2020

Modeling and Analysis of Falling Liquid Films

Yadong Ruan
Claremont Graduate University

Modeling and Analysis of Falling Liquid Films

Yadong Ruan

Institute of Mathematical Sciences

Claremont Graduate University

2020

Approval of the Dissertation Committee

This dissertation has been duly read, reviewed, and critiqued by the committee listed below, which hereby approves the manuscript of Yadong Ruan as fulfilling the scope and quality requirements for meriting the PhD degree in Mathematics.

Marina Chugunova, Co-Chair
Claremont Graduate University
Institute of Mathematical Sciences
Professor

Ali Nadim, Co-Chair
Claremont Graduate University
Institute of Mathematical Sciences
Professor

Alfonso Castro
Harvey Mudd College
Department of Mathematics
Professor

Abstract

Modeling and Analysis of Falling Liquid Films

By

Yadong Ruan

Claremont Graduate University: 2020

In this work, we consider the dynamics of falling liquid films in various geometries. We first examine the dynamics of a thin film formed by a distributed liquid source on a vertical solid wall. The mathematical model is derived using the lubrication approximation and includes the effects of gravity, upward airflow and surface tension. When surface tension is neglected, a critical source strength is found below which the film flows entirely upward due to the airflow, and above which some of the flow is carried downward by gravity. In both cases, a steady state is established over the region where the finite source is located. Shock waves that propagate in both directions away from the source region are analyzed. Numerical simulations are included to validate the analytical results. For models including surface tension, numerical simulations are carried out. The presence of surface tension, even when small, causes a dramatic change in the film profiles and the speed and structure of the shock waves. These are studied in more detail by examining the traveling wave solutions away from the source region. Next, we present several analytical results pertaining to the thin film equation when it includes a source term. The existence of weak solutions, the long-time behavior of solutions for a constant initial condition, and the general qualitative behavior of solutions are all considered. The thin film equation with a source is a highly simplified version of the model derived earlier in the thesis. Finally, we consider a separate model describing the axisymmetric flow corresponding to a falling liquid film around a vertical circular fiber. Recent experimental results have shown that a film exiting a nozzle at the top and falling down a vertical fiber can give rise to individual "droplets," i.e., thicker liquid regions, separated by much thinner zones. The droplets that traverse the circular fiber may exhibit several distinct regimes. Depending on nozzle diameter and flow rate, they may appear as uniformly distributed uniformly sized droplets, as large droplets separated by a series of small droplets in between, or as non-uniformly distributed non-uniformly sized droplets. We present and qualitatively analyze a

novel mathematical model of such flows to supplement this experimental analysis, one capable of showing the convective regime where faster moving droplets collide and sometimes merge with slower moving ones initially, but with a steady travelling state emerging eventually. While previous models of such flows have focused on the slow laminar viscous regime, our model assumes high Reynolds number flow and takes the flow profile to be a plug-flow, but with a thin boundary layer near the fiber providing the drag force on the film. We compare these models and provide various simulations using both inflow-outflow and periodic boundary conditions. We also analyze the linear stability of an initially uniform state and show that there exists a finite range of wavenumbers, including a unique wavenumber with the maximum growth rate, for which the uniform system is unstable.

Acknowledgements

I would like to express my deepest appreciation to my advisors Professor Marina Chugunova and Professor Ali Nadim for all the guidance and insights provided in the research. I must also thank the member of my dissertation committee, Professor Alfonso Castro for reviewing my thesis.

Contents

List of Figures

Chapter 1

Thin liquid film resulting from a distributed source

1.1 Introduction

The motivation for this work was an industrial problem presented by W. L. Gore and Associates at the Mathematical Problems in Industry (MPI) workshop that took place in Claremont, CA in June of 2018. The problem concerned modeling dense porous catalysts in which a gaseous reaction produces liquid in the interior of the catalyst, which gradually pushes its way out to the exterior surface, forming drops or films of liquid on that surface. These block the gaseous reactants from entering the pores and slow down the reaction. In order to remove the liquid drops or films from the surface, one option being considered was to temporarily increase the flow of gas past the surface in the hope of blowing off the liquid film.

In this work, in order to gain insight into some of the underlying physics of that problem, we undertook to model a thin liquid film on a vertical wall, being generated by a finite distributed source of liquid on the wall to represent the liquid that oozes out of the porous catalyst onto the surface. We included the effects of gravity which causes the film to flow downward along the wall, as well as an upward airflow that, if strong enough, could drag the film up the wall. We also included the effects of surface tension in our model.

The evolution of film thickness driven by various external driving forces is of much interest

given its applications in many different areas of physics and engineering involving coating flows. In such flows, if the film is thin in one dimension compared to the others, the so-called lubrication approximation provides a simpler model for analysis, as opposed to solving the full Navier-Stokes equations that govern viscous fluid flow. A review of lubrication theory is provided in [44]. Models in higher dimensions are also being investigated, such as the three-dimensional gravity-driven thin liquid film flow on an inclined plane described in [39].

In some of the thin film mathematical models, solutions of particular form can be constructed, including travelling wave, similarity and steady state solutions. These solutions provide insights for further analysis. For instance, in [23], the authors provided a similarity solution for viscous source flow on inclined plane. Certain properties of the derived thin film model, such as the speed of drop spreading, are also important. For example, analyse of the minimum wetting rate and the corresponding minimum liquid film thickness were presented in [25] and validated with experimental data.

Another aspect of these problems that has received a lot of attention is the stability of the film under different perturbations as well as methods to stabilize the film. Stability of thin wavy films flowing down an inclined plate was studied in [43] and [38]. In [21] and [22], the author introduced several functions for deformed walls to stabilize the film surface with respect to time-dependent perturbations, reporting numerical results. The stability of liquid flow down a heated inclined plane was examined in [1]. References [17] and [16] respectively studied thin viscoelastic liquid films flowing down a vertical wall and a vertical cylinder. In [56], the stability of liquid film flow on a porous inclined plane was examined, while the film stability on a wavy surface was studied in [68].

Many experiments and theoretical analyses have been done on the motion of thin films with a given initial condition. For instance, an accelerating laminar thin-film flow along a vertical wall was investigated in [51], laminar flow on a wavy inclined surface was studied in [10], and liquid films falling vertically on the outer wall of a circular tube were studied experimentally in [63]. Several characteristics of thin film flow on inclined surfaces were studied in [11]. Three-dimensional droplet models and wave dynamics on inclined and vertical walls were studied in [58] and [46], respectively. Experimental studies of viscous, particle-laden thin films were reported in [67]. Flows under obstacles were examined in [9].

2

Few authors have considered source terms in the thin film equation. In [33], a numerical method for the Reynolds equation for a steady liquid layer flowing down a slightly inclined plate from a point source is presented. In [40], the flow of a viscous fluid from a point or line source on an inclined plane is analyzed. The effect of surface tension was neglected in [40]. In our present work, we model thin films formed from a finite source region along a vertical solid wall while considering the effects of gravity, airflow and surface tension. This case is important since some industrial gaseous chemical reactions that occur in porous catalysts give rise to liquids on the exterior surfaces that fit within this model.

Some research has also covered non-Newtonian fluids, including thin-film flow of a power-law liquid on an inclined plate in [42] and stability analysis of travelling wave solutions of power-law liquid films in [49]. A exact solution of the thin film flow problem for a third grade fluid on an inclined plane is provided in [32].

In this work, we derive a mathematical model for film motion along a solid vertical wall in the form of a partial differential equation for film thickness $h(x,t)$ as a function of distance x increasing downward and time t. The final model after scaling turns out to be

$$h_t + (h^3 - h^2 + \alpha h_{xxx})_x = S(x),\qquad(1.1)$$

where $\alpha > 0$ is a dimensionless parameter that characterizes the effect of surface tension. Terms h^3 and $-h^2$ represent the downward flux due to gravity and the upward flux due to airflow, respectively. The right-hand side in this equation is the distributed source which we take to be of the form

$$S = \begin{cases} S_0 & \text{if } x \in (0,1) \\ 0 & \text{otherwise.} \end{cases}\qquad(1.2)$$

The main results for this chapter are in two parts. In the first part we consider the case $\alpha = 0$, which is the case where surface tension can be ignored. In many practical conditions, the dimensionless surface tension parameter is indeed very small. The model then reduce to

$$h_t + (h^3 - h^2)_x = S(x).\qquad(1.3)$$

3

For this first order nonlinear partial differential equation, we use the method of characteristics to analyze its dynamics. With the source given by Eq. (1.2), shock waves will form, with their number and structure depending on S_0. For all values of S_0, an upward propagating shock wave will form as the film is carried up by the airflow. However, we obtain a critical source value S_c, so that if $S_0 > S_c$, a second downward propagating shock wave will also form, as the excess fluid falls downward due to gravity. A steady state solution over the source region $(0,1)$ is also derived, with dramatically different form depending on whether the source strength is below or above the threshold value. A numerical solution is also obtained to validate the results from the method of characteristics.

In the second part of this work, we consider the full model with surface tension effects. Numerical simulations are carried out for various S_0 and α values. The numerical results indicate potential connections between the solutions of the full model (1.1) with travelling wave solutions of the thin film equation without source. Importantly, we find that even for quite small values of the surface tension parameter α, there is a significant change in the profile of the thin film and the speed of the shock waves, as compared to the case with zero surface tension.

1.2 Model Derivation

We model a thin-film driven by gravity and external airflow under the lubrication approximation. We assume the flow to be two-dimensional with coordinate x along the wall and y normal to the wall, with respective velocity components u and v, and take the wall to make angle α with the horizontal direction, which for a vertical wall will become $\alpha = \pi/2$. Let us start with the Navier-Stokes equations with constant viscosity μ and density ρ:

$$\rho(\frac{\partial \vec{u}}{\partial t} + \vec{u} \cdot \nabla \vec{u}) = \rho \vec{g} - \nabla p + \mu \Delta \vec{u}. \tag{1.4}$$

Denote the scale of fluid velocity components $\vec{u} = (u, v)^T$ by U and V respectively, the scale of film thickness by H, and that of the x domain by L. To apply lubrication approximation, we need

$$\epsilon = \frac{H}{L} \ll 1. \tag{1.5}$$

4

The continuity equation for an incompressible liquid reads

$$\nabla \cdot \vec{u} = 0 \quad \Rightarrow \quad \frac{\partial u}{\partial x} + \frac{\partial v}{\partial y} = 0. \tag{1.6}$$

Since the continuity equation needs to be satisfied exactly, upon balancing the respective scales of the two terms we find

$$\frac{U}{L} = \frac{V}{H} \quad \Rightarrow \quad V = \frac{H}{L}U = \epsilon U. \tag{1.7}$$

Now from the x-component of equation (1.4):

$$\rho \frac{\partial u}{\partial t} + \rho u \frac{\partial u}{\partial x} + \rho v \frac{\partial u}{\partial y} = \rho g \sin \alpha - \frac{\partial p}{\partial x} + \mu (\frac{\partial^2}{\partial x^2} + \frac{\partial^2}{\partial y^2})u , \tag{1.8}$$

and using T as the scale for time t and P as that for pressure p, the scales of the seven terms in that equation, in order, become

$$\frac{\rho U}{T}, \quad \frac{\rho U^2}{L}, \quad \frac{\rho V U}{H}, \quad \rho g, \quad \frac{P}{L}, \quad \frac{\mu U}{L^2}, \quad \frac{\mu U}{H^2}. \tag{1.9}$$

Since $H/L \ll 1$, the last term on the RHS of (1.8) is dominant with scale $\mu U/H^2$, and the term $\mu U/L^2$ is smaller by a factor of ϵ^2. To keep the pressure term in balance with the dominant term, we need the scale P for pressure to be

$$P = \frac{\mu U L}{H^2} = \frac{\mu U}{\epsilon^2 L}. \tag{1.10}$$

Also for the gravity term to be of similar magnitude:

$$\rho g \sim \frac{\mu U}{H^2} \quad \Rightarrow \quad U = \frac{\rho g H^2}{\mu} \tag{1.11}$$

which determines the scale U of velocity in the x direction under the model that includes gravity.

On the LHS of (1.8), the second and third terms have scales $\rho U^2/L$ by using the result from

(1.7). We choose the time scales T as

$$T = \frac{L}{U} \tag{1.12}$$

which is the characteristic time for the flow to traverse a distance L at speed U. As such, all the LHS terms have scale $\rho U^2/L$ and the ratio of the LHS to RHS scales turns out to be

$$\frac{\rho U^2/L}{\mu U/H^2} = (\frac{H}{L})^2 \frac{\rho U L}{\mu} = \epsilon^2 \mathrm{Re}_L, \tag{1.13}$$

where $\mathrm{Re}_L = \rho U L/\mu$ is the Reynolds number. Under the assumption that $\epsilon^2 \mathrm{Re}_L \ll 1$, the inertia terms on the LHS of the momentum equation are negligible compared to the terms on the RHS. Hence, to leading order, we can approximate the x-momentum equation by:

$$\rho g \sin \alpha - \frac{\partial p}{\partial x} + \mu \frac{\partial^2 u}{\partial y^2} = 0. \tag{1.14}$$

Similarly, the y-component of equation (1.4) with the same scaling applied to all the terms results in the leading order equation:

$$0 = -\rho g \cos \alpha - \frac{\partial p}{\partial y}. \tag{1.15}$$

We now discuss the boundary conditions on the solid-liquid ($y = 0$) and liquid-air ($y = h(x,t)$) interfaces. No-slip and no-penetration conditions at the solid-liquid interface would normally require:

$$u(x,0,t) = 0, \quad v(x,0,t) = 0. \tag{1.16}$$

However, when a steady fluid source is considered at the interface, with liquid volume emanating from the porous wall, the condition on the velocity component v changes to $v(x,0,t) = S(x)$ where $S(x)$ is the source strength.

At the liquid-air interface $y = h(x,t)$, we have kinematic and dynamic boundary conditions.

The normal stress balance at the interface reads:

$$\hat{n} \cdot \left[\pi_{\text{air}} - \pi_{\text{liquid}}\right] \cdot \hat{n} = \sigma \mathcal{K} \tag{1.17}$$

where $\hat{n}$ is the normal vector pointing from the liquid towards the air, and $\mathcal{K}$ is the local curvature of interface, and we have

$$\pi_{\text{air}} = -p_{\text{atm}} I, \quad \pi_{\text{liquid}} = -pI + \mu \begin{pmatrix} 2u_x & v_x + u_y \\ v_x + u_y & 2v_y \end{pmatrix}$$

The normal vector is well approximated by the unit vector in the y-direction since $\partial h / \partial x$ has scale $H/L = \epsilon \ll 1$:

$$\hat{n} = \frac{\nabla(y - h(x,t))}{|\nabla(y - h(x,t))|} = \frac{1}{\sqrt{1 + (\frac{\partial h}{\partial x})^2}} \begin{pmatrix} -\frac{\partial h}{\partial x} \\ 1 \end{pmatrix} \approx \begin{pmatrix} 0 \\ 1 \end{pmatrix} \tag{1.18}$$

For curvature $\mathcal{K}$ we have

$$\mathcal{K} = \nabla \cdot \hat{n} \approx -\frac{\partial^2 h}{\partial x^2} \tag{1.19}$$

Substituting into (1.17), we find

$$-p_{\text{atm}} + p - 2\mu \frac{\partial v}{\partial y} = -\sigma \frac{\partial^2 h}{\partial x^2}. \tag{1.20}$$

In order for the surface tension term not to be negligible, we need the scale for last term to be comparable to pressure terms; that is, we must have

$$\frac{\sigma H}{L^2} \sim \frac{1}{\epsilon^2} \frac{\mu U}{L} \quad \Rightarrow \quad \frac{\mu U}{\sigma} \sim \epsilon^3. \tag{1.21}$$

This corresponds to having a very small capillary number, requiring surface tension to be relatively large compare to viscous effects. Under this scaling and recognizing that the normal viscous

7

stress $\mu(\partial v / \partial y)$ is also small compared to the other terms, the normal stress balance simplifies to

$$p - p_{\text{atm}} = -\sigma \frac{\partial^2 h}{\partial x^2} \,. \tag{1.22}$$

Now consider the tangential stress balance at the interface which reads

$$\hat{n} \cdot \pi_{\text{liquid}} \cdot \hat{t} + \tau = 0 \tag{1.23}$$

where τ is the upward wind stress exerted by the external airflow and $\hat{t} \approx (1,0)^T$ is the unit tangent at the interface. This equation reduces to

$$\mu \left(\frac{\partial u}{\partial y} + \frac{\partial v}{\partial x} \right) = -\tau \,, \tag{1.24}$$

which, given that the scale of $\partial u / \partial y$ is much larger than that of $\partial v / \partial x$, simplifies to

$$\mu \frac{\partial u}{\partial y} = -\tau \,. \tag{1.25}$$

The kinematic boundary condition at the interface requires

$$\frac{D}{Dt}(y - h(x,t)) = 0 \quad \Rightarrow \quad (y - h(x,t))_t + \vec{u} \cdot \nabla(y - h(x,t)) = 0 \,. \tag{1.26}$$

This results in

$$\frac{\partial h}{\partial t} = v - u \frac{\partial h}{\partial x} \,. \tag{1.27}$$

Based on the scales we determined earlier, including the one for time t, we see that all three terms have comparable scales ϵU.

Summarizing all the equations and boundary conditions and specializing to the case when the

8

wall is vertical, i.e., $\alpha = \pi/2$, we have:

$$0 = \frac{\partial p}{\partial y} \tag{1.28}$$

$$0 = \rho g - \frac{\partial p}{\partial x} + \mu \frac{\partial^2 u}{\partial y^2} \tag{1.29}$$

$$0 = \frac{\partial u}{\partial x} + \frac{\partial v}{\partial y} \tag{1.30}$$

which respectively represent the y- and x-components of the momentum equation and the continuity (incompressibility) equation, subject to boundary conditions at $y = 0$:

$$u = 0 \tag{1.31}$$

$$v = S(x) \tag{1.32}$$

and those at $y = h(x, t)$:

$$p = p_{\text{atm}} - \sigma \frac{\partial^2 h}{\partial x^2} \tag{1.33}$$

$$\mu \frac{\partial u}{\partial y} = -\tau. \tag{1.34}$$

Differentiating (1.33) with respect to x, we find

$$\frac{\partial p}{\partial x} = -\sigma \frac{\partial^3 h}{\partial x^3}. \tag{1.35}$$

This term is also independent of y because of equation (1.28). Integrating (1.29) with respect to y twice, we obtain

$$u(x, y, t) = \frac{1}{\mu}(-\sigma \frac{\partial^3 h}{\partial x^3} - \rho g)\frac{y^2}{2} + \frac{1}{\mu}C_1(x, t)y + C_2(x, t). \tag{1.36}$$

Using (1.31), we have $C_2(x, t) = 0$ and using (1.34), we find

$$C_1 = \frac{h}{\mu}(\rho g + \sigma \frac{\partial^3 h}{\partial x^3}) - \frac{\tau}{\mu}.$$

Integrating (1.30) at a fixed location x with respect to y from 0 to $h(x, t)$, and making use of (1.32)

and (1.27) yields:

$$\frac{\partial h}{\partial t} + \frac{\partial q}{\partial x} = S(x), \tag{1.37}$$

where the volume flux q has been defined as $q = \int_0^h u(x,y,t)dy$. The latter can be found from the velocity profile given above to have the explicit form:

$$q = \frac{\rho g}{3\mu}h^3 - \frac{\tau}{2\mu}h^2 + \frac{\sigma}{3\mu}\frac{\partial^3 h}{\partial x^3}h^3. \tag{1.38}$$

The first term on the RHS represents the downward flow due to gravity and the second term the updard flow due to the airflow. If surface tension is not as large in magnitude as required by the scaling (1.21), we can ignore the effects of surface tension and drop the last term in the expression for the flux.

While we derived the above conservation equation and flux expression in dimensional form, albeit guided by the scaling analysis which indicated which terms could be neglected, at this point we can go ahead and nondimensionalize the system. Define the starred dimensionless variables by

$$h = Hh^*, \quad x = Lx^*, \quad t = Tt^*, \quad S = S_{\text{scale}}S^* \tag{1.39}$$

with

$$H = \frac{3\tau}{2\rho g}, \quad T = \frac{4\mu\rho g L}{3\tau^2}, \quad S_{\text{scale}} = \frac{9\tau^3}{8\mu\rho^2 g^2 L}. \tag{1.40}$$

Here, length scale H corresponds to the film thickness at which the downward flux due to gravity exactly balances the upward flux due to the wind stress associated with airflow; i.e., the film thickness at which the first two terms in the expression for flux q balance each other exactly. The length scale L is associated with the distance along the wall, for instance the length of the region over which the source is nonzero. By assumption, $\epsilon = H/L \ll 1$. The time scale T in the above can be shown to be equivalent to $T = 3L/U$ with velocity scale U given by $U = \rho g H^2/\mu$. The scale for the source emerges naturally from equating the orders of magnitude of the terms in

the conservation equation. Substituting these and and dropping the superscript star from the dimensionless variables for clarity, we finally have

$$h_t + (h^3 - h^2 + \alpha\, h^3 h_{xxx})_x = S(x) \tag{1.41}$$

where $\alpha = \sigma H/(\rho g L^3) = \epsilon^3/\mathrm{Ca}$, where $\mathrm{Ca} = \mu U/\sigma$ is the capillary number based on the velocity scale $U = \rho g H^2/\mu$. As indicated earlier, in order for surface tension not to be negligible, the Capillary number needs to be small, of order ϵ^3, which would make dimensionless parameter α of order unity. The model we derived here is similar to the thin film model with gravity and Marangoni effects in [62] and [7]. In the next section, we first analyze the case where surface tension effects are negligible, by taking coefficient α to be zero. However, since that coefficient multiplies the highest order spatial derivative, one can expect a somewhat singular behavior so that the solution in the presence of α, no matter how small, might be qualitatively different from that in the complete absence of surface tension. We will see that this is indeed the case in a later section where surface tension effects are added back in.

1.3 Model without Surface Tension

To ignore the effect of surface tension, parameter α is set to zero. Furthermore, the source strength $S(x)$ is assumed to be uniform over a finite domain of dimensionless length 1, and zero elsewhere, namely:

$$S(x) = \begin{cases} S_0 & \text{if } x \in [0,1] \\ 0 & \text{otherwise} \end{cases}$$

In this case, we can derive certain results through analysis. We will find that if the source strength S_0 is less than a threshold, the liquid is carried upward by the airflow and none of it falls down due to gravity. The upper front of the film propagates as a shock front, whose speed we can predict. When the source strength exceeds the threshold, some of the liquid produced is still carried upward by the airflow, while the rest falls down due to gravity. Over the region where the source is nonzero, a steady film profile is achieved in both cases. A numerical solution of the nonlinear film equation produces results that agree with the analytical predictions.

11

1.3.1 The Simplified Model

In the absence of surface tension, the expression for the flux becomes $q(h) = h^3 - h^2$ and the film thickness $h(x,t)$ satisfies the simplified equation:

$$\frac{\partial h}{\partial t} + (3h^2 - 2h)\frac{\partial h}{\partial x} = S(x),$$

with initial condition

$$h(x,0) = 0,$$

corresponding to not having any liquid on the wall initially. It will be helpful to notice that as h increases away from zero, the flux $q(h)$ is initially negative (corresponding to upward flow due to airflow), reaches a minimum of $-4/27$ when the height reaches $h = 2/3$ and then increases back to zero at $h = 1$ and into positive values beyond that (corresponding to downward flow due to gravity). At the same time, the wave speed $q'(h) = 3h^2 - 2h$ also initially decreases from zero at $h = 0$ to a minimum of $-1/3$ at $h = 1/3$, increasing beyond that point and changing sign, becoming positive, as h passes the value $h = 2/3$.

1.3.2 Characteristic equations

Define $z(s) \equiv h(x(s))$ and write the above equation along characteristics parameterized by variable s as

$$\frac{dt}{ds} = 1 \tag{1.42}$$

$$\frac{dx}{ds} = 3z^2 - 2z \tag{1.43}$$

$$\frac{dz}{ds} = S(x(s)) \tag{1.44}$$

If x remains in the range $[0,1]$ for which $S(x) = S_0$, where $S_0 > 0$ is constant, and replacing s with t by assuming $s = 0$ when $t = 0$, we have:

$$z(t) = S_0 t \tag{1.45}$$

$$x(t) = S_0^2 t^3 - S_0 t^2 + x_0 \tag{1.46}$$

12

where x_0 is the initial point along the x-axis where the characteristic starts, for now taken to be in the range $[0, 1]$. This solution remains valid until $x(t)$ reaches one of the boundaries $x = 0$ or $x = 1$.

Starting at any value of x_0 in our range, the solution $x(t)$ reaches its minimal value at time $t = 2/(3S_0)$, which is independent of x_0. For the characteristic that starts at the bottom point $x_0 = 1$, this minimum would be at $x = 0$ if $S_0 = 4/27$. Therefore, as long as

$$S_0 \leq \frac{4}{27}$$

all characteristic lines that start with $x_0 \in (0, 1)$ do cross the line $x = 0$ at some finite time. Under this assumption, define t^* to be the time at which a characteristic line that start within $(0, 1)$ first reaches $x = 0$. Once the characteristic line crosses $x = 0$, it becomes a straight line and it will not cross the $x = 0$ line again. We can calculate the straight line expression for $t > t^*$. Since we are now in the range $x \in (-\infty, 0)$ where $S(x) = 0$, the characteristic equations for $t > t^*$ become

$$\frac{dH}{dt} = 0 \tag{1.47}$$

$$\frac{dx}{dt} = 3H^2 - 2H \tag{1.48}$$

where H is the height function in that region, with initial conditions

$$H(t^*) = St^* \tag{1.49}$$

$$x(t^*) = 0. \tag{1.50}$$

Solving these two ODEs, we have

$$x(t) = (3S_0^2(t^*)^2 - 2S_0 t^*)t - 3S_0^2(t^*)^3 + 2S_0(t^*)^2.$$

At a given time t, we can treat the equation above as a third order polynomial with respect to t^*, and solve for t^* for the given t and x. Since these characteristics collide with the horizontal characteristics which emanate from the region $x \in (-\infty, 0)$, a shock forms right away at location $(x, t) = (0, 0)$. If the x-coordinate of the shock is denoted by $c(t)$, the Rankine-Hugoniot condition

13
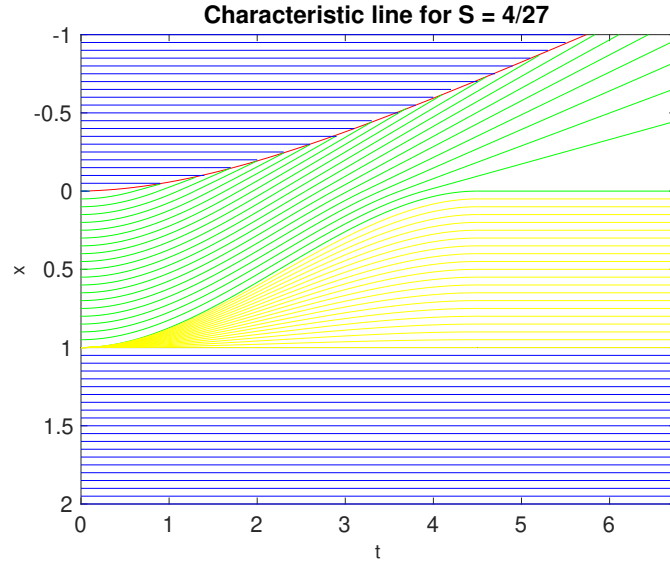
Figure 1.1: A sketch of characteristic lines with $S_0 = 4/27$; note that the vertical axis is the distance x increasing downward, and the horizontal axis represents time t. The red line is the shock curve formed through the intersection of the blue and green characteristics. The blue characteristics emanate outside the source region and are horizontal. The green characteristic curves emanate from the source region and upon passing $x = 0$ become straight lines. The yellow characteristics represent an expansion fan emanating from $x = 1$.

for the shock curve can be used to obtain the speed of the shock, in this case yielding:

$$\frac{dc}{dt} = S_0 t^* (S_0 t^* - 1)$$

with $c(0) = 0$ and with t^* a function of t and c, obtained by solving the cubic equation given above. We applied a forward Euler method to calculate the position of the shock wave numerically. For each iteration in t, we solve the cubic equation to find t^* and update the position of the shock.

Figure 1.1 provides a complete picture of the characteristic curves when the source strength has its threshold value of $S_0 = 4/27$. The numerical results show that as $t \to \infty$, the shock propagate at a constant speed of $1/4$; this is consistent with our numerical simulations of the nonlinear PDE reported below for the given source value.

14

1.3.3 The steady-state solution

If a steady-state solution is reached in the region $x \in (0,1)$, the resulting height function must satisfy $d(h^3 - h^2)/dx = S_0$, which produces the cubic equation

$$h^3 - h^2 = S_0 x + C$$

for $h(x)$. When the source strength $S_0 < 4/27$, the steady-state film height remains zero at $x = 1$, which makes the constant C equal to $-S_0$. Solving the cubic equation for $h(x)$ will then produce the correct steady-state profile over $x \in (0,1)$.

From the method of characteristics, when the source strength exceeds the threshold, i.e., when

$$S_0 \geq \frac{4}{27},$$

the characteristic emanating from the initial point $x_0 = 4/(27 S_0) \in (0,1)$ becomes tangent to the horizontal line $x = 0$ at time $t = 2/(3S_0)$, at which point $h(0, 2/(3S_0)) = 2/3$. Beyond that time, the height at that location remains constant at value $2/3$, which enables us to determine the constant C for that case. Also in that case, the characteristics starting at $x_0 > 4/(27 S_0)$ (but less than 1), do not reach $x = 0$ at any time and instead turn around and exist the domain at $x = 1$, colliding with the horizontal characteristics that emanate from the region $x_0 > 1$. This leads to a second shock front that propagates downward, reflecting the fact that at high source values, some of the flow is carried downward by gravity.

In order for the steady height to remain constant equal to $2/3$ at $x = 0$, the constant C must be given by:

$$C = (\frac{2}{3})^3 - (\frac{2}{3})^2 = -\frac{4}{27}.$$

Then steady-state height profile for $S_0 \geq 4/27$ would be the solution of the new cubic equation:

$$h^3 - h^2 = S_0 x - \frac{4}{27}.$$

The two cases for S_0 below and above the threshold can be combined to write a single cubic

equation whose solution provides the steady-state film profile $h(x)$:

$$h^3 - h^2 = S_0 x - \min\{S_0, \frac{4}{27}\}. \tag{1.51}$$

For source strengths below the threshold 4/27, the steady height remains constant equal to zero at x=1, and for those above the threshold, the steady height remains constant equal to 2/3 at x=0. These can be verified from the numerical simulation of the nonlinear PDE which is described next. Figure 1.2 provides a plot of the family of steady state film profiles over $x \in (0,1)$ for source values below and above the threshold $\frac{4}{27}$.
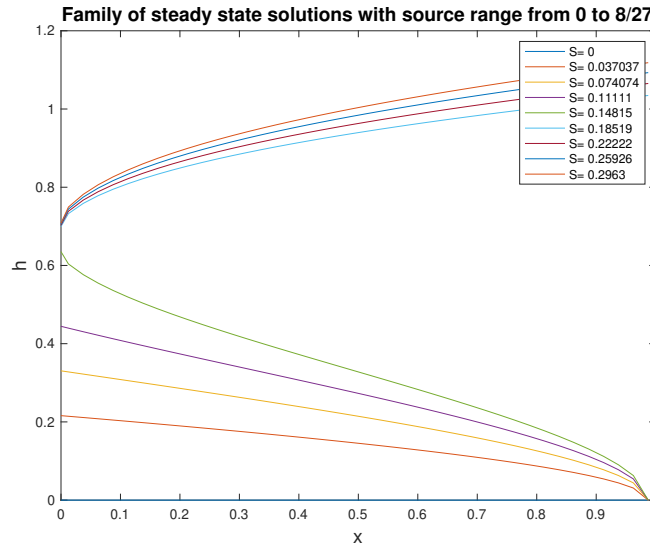
Figure 1.2: The family of steady state solutions with S_0 ranging from 0 to 8/27. The bottom curves are for source strengths below the threshold and the top curves for those above the threshold.

1.3.4   Numerical simulations

For our simplified model without surface tension, we now describe the Godunov method that provides a numerical solution for the time evolution of the film thickness.

Godunov method

We discretize the x-domain into N equally-spaced sub-intervals or cells of size Δx with point x_j referring to the midpoint of the cell j, whose edges are at $x_{j-\frac{1}{2}} = x_j - \Delta x/2$ and $x_{j+\frac{1}{2}} = x_j + \Delta x/2$.

16

Time domain t is also discretized with time-step Δt so that $t_n = n\Delta t$. We denote the average film thickness over cell j at time level n by

$$H_j^n = \frac{1}{\Delta x} \int_{x_{j-\frac{1}{2}}}^{x_{j+\frac{1}{2}}} h(x, t_n)dx.$$

We integrate the conservation equation $h_t + q_x = S(x)$ (with $q = q(h) = h^3 - h^2$) over the domain $[x_{j-\frac{1}{2}}, x_{j+\frac{1}{2}}] \times [t_n, t_{n+1}]$ and simplify to obtain

$$H_j^{n+1} = H_j^n - \frac{1}{\Delta x} \int_{t_n}^{t_{n+1}} q\big(h(x_{j+\frac{1}{2}}, t)\big) - q\big(h(x_{j+\frac{1}{2}}, t)\big)dt + \frac{\Delta t}{\Delta x} \int_{x_{j-\frac{1}{2}}}^{x_{j+\frac{1}{2}}} S(x)dx.$$

Denote the time-average of the flux crossing the edge $x_{j+\frac{1}{2}}$ over the time interval $t \in [t_n, t_{n+1}]$ as

$$\overline{Q}_{j+\frac{1}{2}}^n = \frac{1}{\Delta t} \int_{t_n}^{t_{n+1}} q(u(x_{j+\frac{1}{2}}, t))dt,$$

which produces the discrete conservation equation

$$H_j^{n+1} = H_j^n - \frac{\Delta t}{\Delta x} \left(\overline{Q}_{j+\frac{1}{2}}^n - \overline{Q}_{j-\frac{1}{2}}^n + \int_{x_{j-\frac{1}{2}}}^{x_{j-\frac{1}{2}}} S(x)dx \right).$$

In Godunov's method, the time-averaged flux $\overline{Q}_{j+\frac{1}{2}}^n$ is approximated as follows

$$\overline{Q}_{j+\frac{1}{2}}^n = Q(H_j^n, H_{j+1}^n) = \begin{cases} \min_{H_j^n \leq \theta \leq H_{j+1}^n} q(\theta) & \text{if} \quad H_j^n \leq H_{j+1}^n \\[2mm] \max_{H_{j+1}^n \leq \theta \leq H_j^n} q(\theta) & \text{if} \quad H_j^n > H_{j+1}^n \end{cases}$$

relating the flux to the average heights on either side of the edge at time level n. In our case, since $q(h) = h^3 - h^2$ and $h \geq 0$, the only minimum in $q(h)$ occurs at $h = 2/3$ and the formula simplifies to

$$\overline{Q}_{j+\frac{1}{2}}^n = \max\left(q\big(\max(H_j^n, \frac{2}{3})\big), q\big(\min(H_{j+1}^n, \frac{2}{3})\big) \right).$$

For numerical stability, one must require the time step to be small enough, according to the stability condition

$$\frac{\Delta t}{\Delta x} \leq \frac{1}{2\max_j |q'(H_j^n)|}.$$
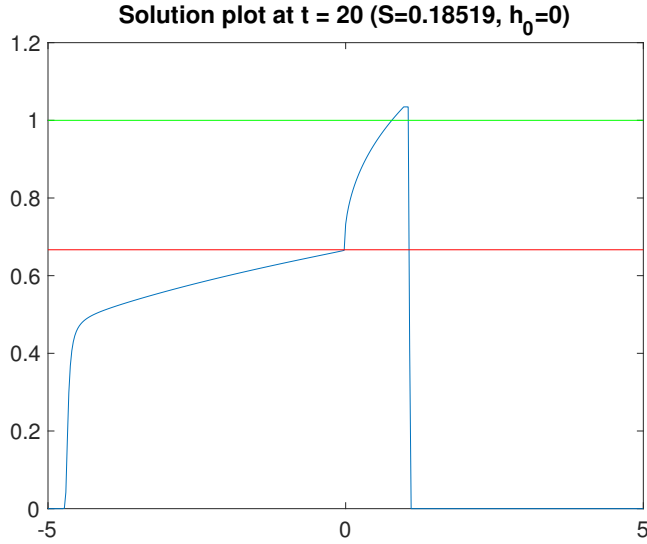
Figure 1.3: Plot of the numerical solution at time $T = 20$, with $S_0 = \frac{5}{27}$ and $h_0 = 0$. The horizontal axis represents the x-coordinate along the vertical wall, with the positive direction being downward. The vertical axis is the height of fluid film. Since this source value is larger than critical value $\frac{4}{27}$, we can see two shock waves, one going upward and one downward.

In the simulations presented below, we take $\Delta t / \Delta x = 1/8$.

Results

In the following, we present results for the case $S_0 = 5/27$, which is above the threshold value of $4/27$. We thus expect some of the flow to be carried downward by gravity, while some portion is still carried upward by the airflow. We simulate the equation over the region $x \in [-5, 5]$ with $\Delta x = 0.025$.

Figure 1.3 presents the film profile at time $t = 20$ starting with no liquid film for a source strength of $S_0 = 5/27$ acting over $x \in [0, 1]$. The horizontal lines at heights 1 and 2/3 are drawn for visual references. Once the film height reaches a value of 2/3 at $x = 0$, it stays at that value, while the excess liquid is carried upward (toward negative x values) by the airflow. Some of the liquid also flows downward (toward positive x values) due to gravity although at time $t = 20$, only a small amount has gone past the edge $x = 1$.

Figure 1.4 presents the evolution of the film profile from time $t = 0$ to $t = 20$ starting with zero initial film thickness and with a source strength of $S_0 = 5/27$ confined to the region $x \in [0, 1]$. It is

18
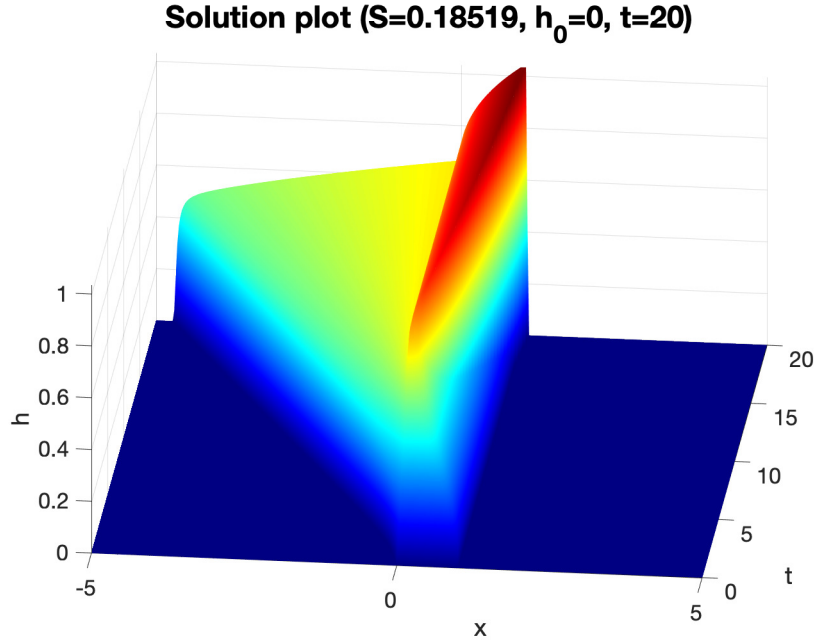
Figure 1.4: Evolution of the film profiles from $T = 0$ to 20 for $S_0 = \frac{5}{27}$ and $h_0 = 0$. The film height is plotted as a function of x and t.

seen that the shock traveling upward (toward negative x values) achieves a fairly constant speed of propagation.

In Figure 1.5 we compare the numerical solution at large times over the range $x \in [0,1]$ to the steady state solution over that range which solves Eq. (1.51). The two results are in excellent agreement.

1.4 Model with Surface Tension

In Section 1.2 we derived the model with surface tension in the form of Eq. (1.41) in which dimensionless parameter $\alpha = \sigma H / (\rho g L^3)$ measured the relative importance of surface tension. While the previous section analysed the system when $\alpha = 0$, here we will examine the solution when that parameter is nonzero.
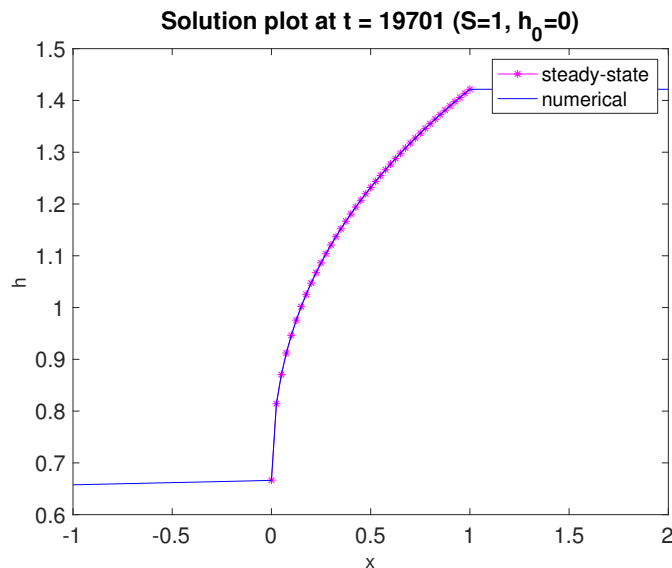
Figure 1.5: Comparison of numerical simulation results at large times with the steady state solution calculated from Eq. (1.51) over the range $x \in [0, 1]$.

1.4.1 Numerical Simulations using COMSOL

For the full model with surface tension, we conduct numerical simulations using the software COMSOL MultiPhysics for various source strengths S_0. We observe some similarities with the simplified model; however, there are significant differences also.

Figure 1.6 provides a series of simulations over the domain $(-15, 15)$ corresponding to weak source strengths (below the threshold of $4/27$ predicted for zero surface tension). In the top picture, the dashed lines present the early time evolution snapshots for parameter values: $S_0 = 4/35$ and $\alpha = 0.001$, at times: $t = 0.8; 2.8; 5.6$. The solid lines present the later time evolution snapshots at times $t = 17.2; 37.2; 54.0$. A steady state is established over the source region $(0, 1)$. For these weak source values, none of the fluid falls due to gravity (i.e., none moves to the right beyond the edge $x = 1$). The fluid that gets transported to the left (upward due to airflow) has a leftmost front that looks like a typical shock, but the relatively flat region next to that front jumps down to a lower value (more evident in the middle and bottom panels) across an oscillatory front that propagates at a different speed from the leftmost front. The left front wave has height 0.783, moving to the left at speed 0.166; the second left wave is very slow with a speed of about 0.012 and a peak height of about 0.845. The height of the left front wave does not depend on the source strength, as
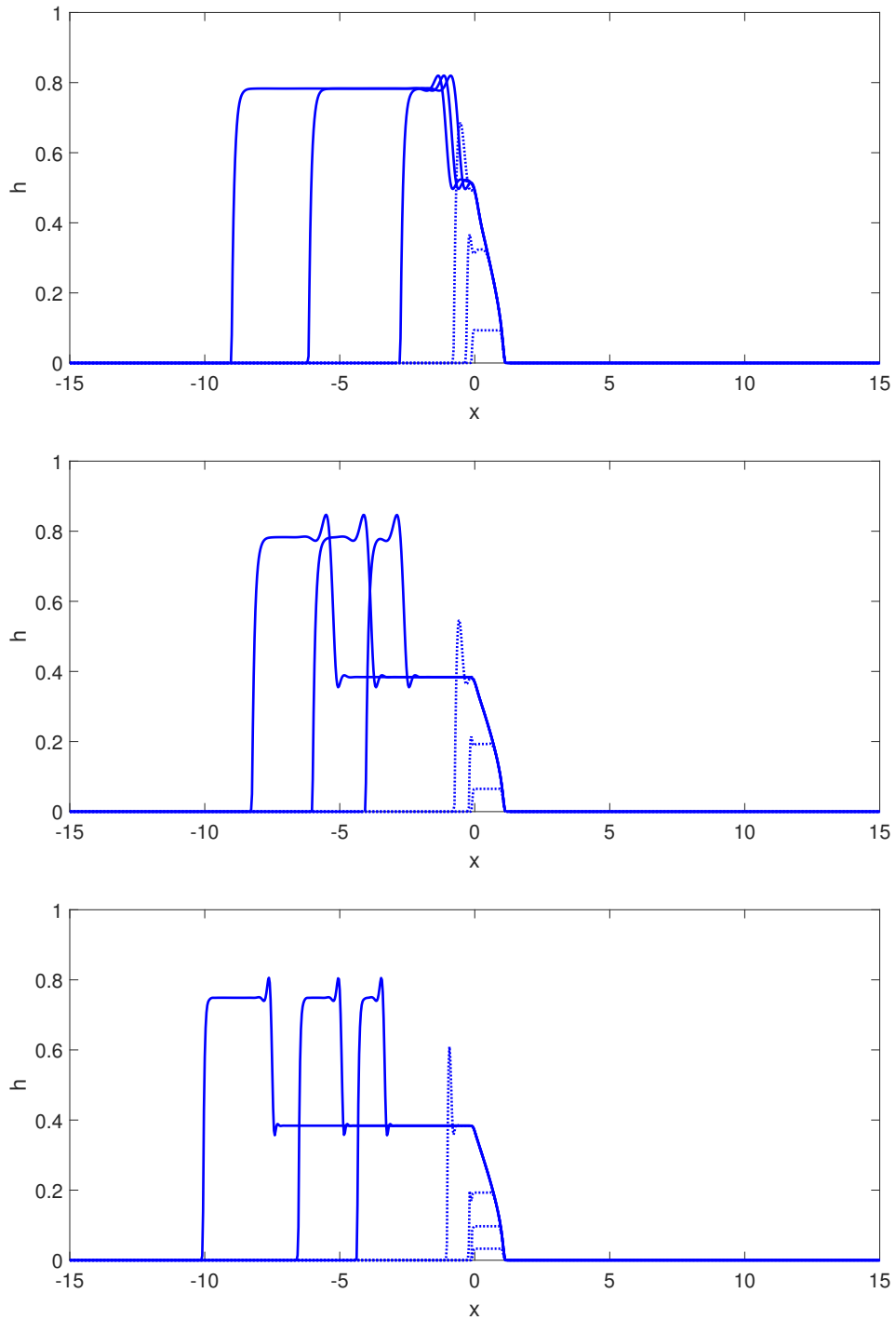
Figure 1.6: Weak source simulations indicate the propagation of waves in one direction only: to the left due to airflow. Top picture: $S_0 = 4/35$, $\alpha = 0.001$; middle picture: $S_0 = 4/50$, $\alpha = 0.001$; bottom picture: $S_0 = 4/50$, $\alpha = 0.0001$. Refer to the text for more detailed descriptions.

will be seen in the middle panel.

In the middle picture, the dashed lines provide the early time evolution snapshots for $S_0 = 4/50$ and $\alpha = 0.001$ at times: $t = 0.8; 2.4; 6$. The solid lines show the later time evolution snapshots at times: $t = 25.2; 36.8; 50.0$. The left front wave has height 0.783 and moves to the left with speed 0.173. The second left-going wave is slower with a speed of about 0.107 and a peak height of about 0.845, connecting to a flat part of height 0.384. Changing the source strength does not influence the height of the left front wave but it moves a bit faster, the height of the second left wave is also unchanged but it is moving much faster to the left as we decrease the source strength away from its threshold value.

In the bottom panel, the dashed lines give the early time evolution snapshots for an even smaller surface tension case, with parameter values: $S_0 = 4/50$ and $\alpha = 0.0001$ at times: $t = 0.4; 1.2; 2.4; 7.2$. The solid lines provide the later time evolution snapshots at times $t = 24.8; 36.4; 55.2$. The left front wave has height 0.749 and moves with speed 0.188. The second left wave is slower with a speed of about 0.138 and a peak height of about 0.806, connecting to a flat part of height 0.384. Reducing surface tension speeds up the front left wave and lowers its height, but contrary to the strong source case (presented next) the second wave also speeds up.

It follows from the simulations that the height of the left front wave is not controlled by the source term and only depends on the surface tension coefficient, as does its speed. The second wave speed and direction, however, are controlled by the source strength.

Figure 1.7 presents a set of simulations with stronger source strengths (above the threshold) that result in two fronts moving in opposite directions. In the top panel, the dashed lines provides the early time snapshots for parameter values: $S_0 = 4/15$, $\alpha = 0.001$, at times $t = 1.2; 2.0; 2.8; 4.8$. The solid lines are the later time snapshots at $t = 16.4; 36.8; 55.6$. The left-going front has a height of approximately 0.783, moving with an approximate speed of 0.168. The right-going front has a flat part of height 1.132 (peak at 1.573) and it is moving a little slower with a speed of about 0.163.

In the middle panel, the dashed lines are the early time snapshots for parameter values: $S_0 = 4/15$ and $\alpha = 0.0001$ (a factor of ten smaller than the top panel) at $t = 1.2; 2.8; 5.2; 7.2$. The solid lines are the later snapshots for parameter at times $t = 15.6; 35.2; 54.8$. The left-going front has an approximate height of 0.749 and moves with an approximate speed of 0.188. The right-going front has a flat region of height 1.127 (peak at 1.510) and it is moving a little slower at a speed
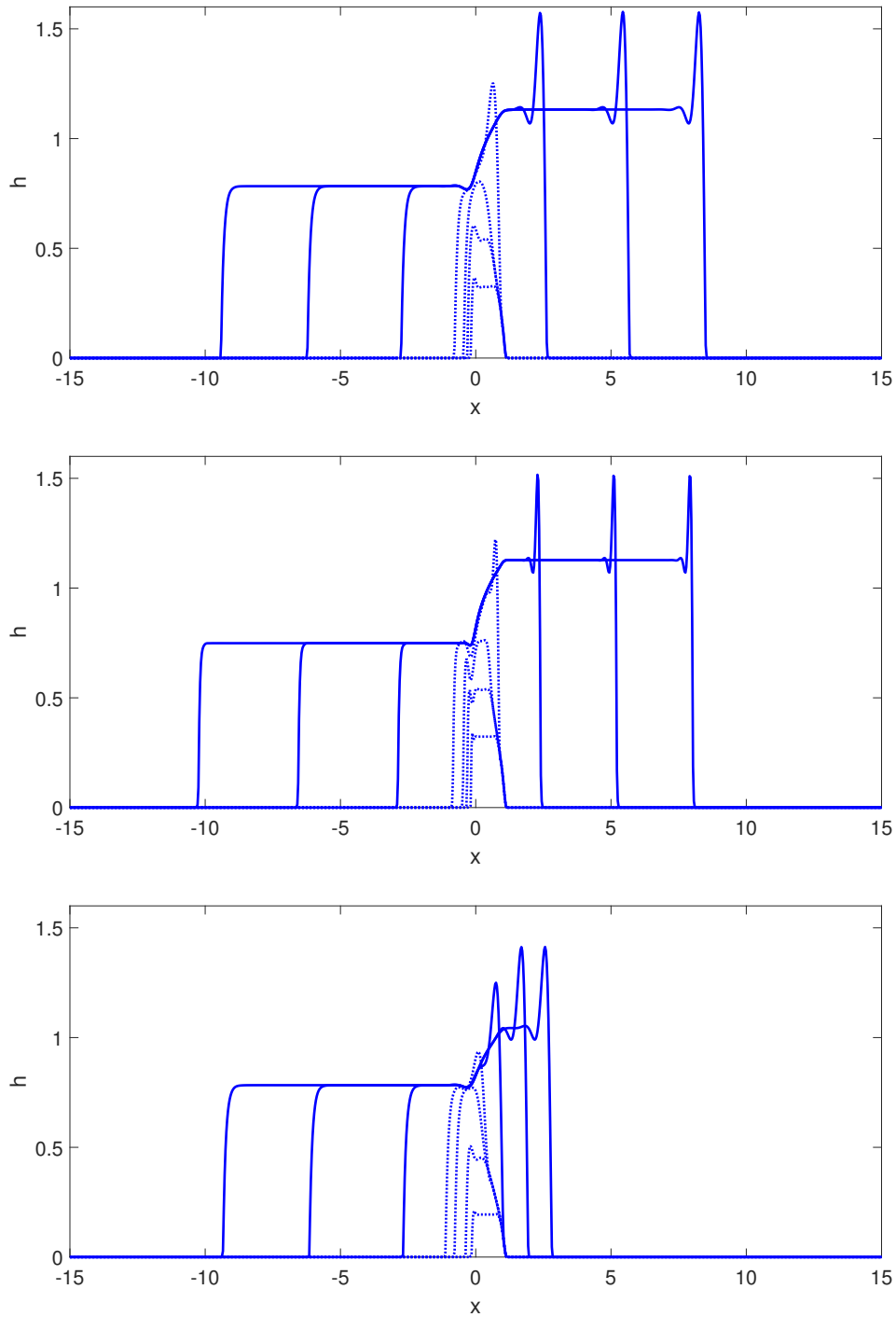
Figure 1.7: Strong source simulations indicate propagation of waves in both directions: left-going due to airflow and right-going due to gravity. Top picture: $S_0 = 4/15$, $\alpha = 0.001$; middle picture: $S_0 = 4/15$, $\alpha = 0.0001$; bottom picture: $S_0 = 4/25$, $\alpha = 0.001$. Refer to the text for more detailed descriptions.

of about 0.143. The ten-fold reduction in surface tension from 0.001 to 0.0001 resulted in a faster propagation of the left front while lowering its height. The right-moving front also has a lower height but, contrary to the left wave, it slows down.

In the bottom panel, the dashed lines are the early time snapshots for parameter values: $S_0 = 4/25$ and $\alpha = 0.001$, at $t = 1.2; 2.8; 5.2; 7.2$. The solid lines are the later time snapshots at times $t = 16.4; 36.8; 55.6$. The left-going front has height 0.783 and moves with speed 0.173. The right-going front has a flat part of height 1.132 (peak at 1.573) and it moves slower at a speed of about 0.047. Reducing the source from 4/15 to 4/25 does not affect the height of the left-going front but increases its speed, while the right-moving front does not change its height either, but slows down appreciably.

By examining both Figures 1.6 and 1.7 combined, it becomes apparent that for weak source strengths below the threshold, we have the left-going front and the second left-moving wave. The latter moves to the left more and more slowly as the source strength approaches the threshold and eventually changes directions and becomes a right-moving wave as the source-strength increases above the threshold value. While both of these waves exhibit oscillations before connecting two flat regions, when the wave moves to the right (due to gravity), it connects a flat region of zero, whereas when it was moving to the left, it connected two flat regions of finite heights.

Another important observation one can make by comparing the results with surface tension with those in the complete absence of surface tension (i.e., Figure 1.3 from the previous section), is that even a small amount surface tension ($\alpha = 0.001$) appreciably slows down the left-moving front and makes the region behind the left front flat, as opposed to having a clear slope apparent in Figure 1.3.

To explore the effect of surface tension on the front propagation, we examine the height and speed of the left-going wave for a larger set of surface tension parameter values α. Figure 1.8 ($S_0 = 4/15$) shows that left-going front speed decreases with height and that as surface tension parameter α becomes larger, the front height approaches an approximate value of 0.8 (for an even higher value of $\alpha = 0.1$ the height is about 0.806, and for $\alpha = 0.5$ the height is about 0.805). The relation between the front speed and height seen on the left plot in Fig. 1.8 can be explained by seeking a traveling wave solution of Eq. (1.41) away from the source region. For a left-going wave, if we take $h(x, t)$ to have the traveling wave form $h(x + ct)$ with $c > 0$, the PDE away from the
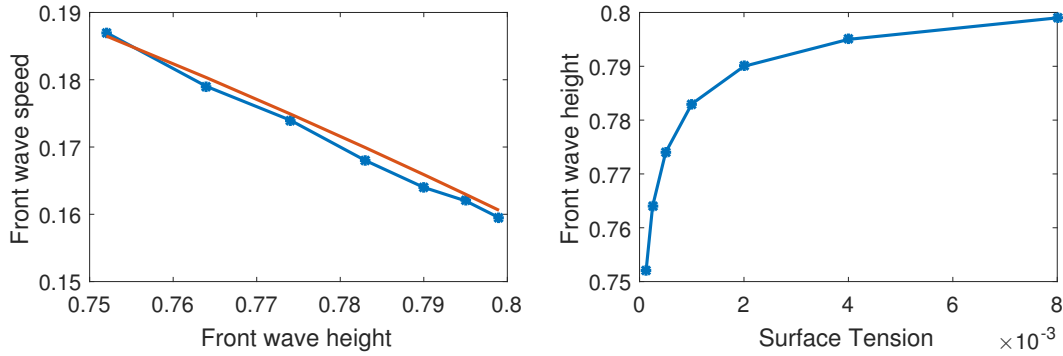
Figure 1.8: The plot of the left front wave speed versus its height is on the left and the plot of the left front wave height versus values of α (surface tension coefficient) is on the right.

source reduces to

$$ch + (h^3 - h^2 + \alpha h^3 h''') = \text{constant}\,.$$

In the flat regions on either side of the front, h''' is zero, and to the left of the front, $h = 0$. This makes the constant on the RHS equal to zero and for the flat region of height h, the traveling wave speed is evaluated to be $c = h - h^2$ (see the red curve on the figure). This is in approximate agreement with the data points plotted in the figure.

1.5 Discussion and Conclusions

Let us first compare the cases with and without surface tension to highlight their key differences. Figure 1.9 shows two sets of simulations for a source strength of $S_0 = 4/20$ that produces traveling waves in both direction, with liquid climbing the wall due to airflow (going left in the plots) and excess liquid falling down due to gravity (going right in the plots). In the top panel, surface tension is zero ($\alpha = 0$), while in the bottom panel surface tension is nonzero but rather small ($\alpha = 0.001$). The profiles are plotted at the same times indicated in the legend. It is obvious that even for quite small values of the surface tension parameter, the profiles are strongly affected. In the absence of surface tension, the left-going waves in the top figure advance at a higher speed and the profiles behind them have positive slopes that decrease as the front advances. In contrast, in the presence of surface tension, that front moves left more slowly and behind the front, the profile is flat and maintains a constant somewhat higher height. On the other hand, the right going waves move

a little faster when surface tension is present, and the constant part of the profile behind those waves connects to the zero region in front through an oscillatory section with a large peak, to be compared to the flat profile of the right-going waves without surface tension in the top figure. Since the surface tension parameter α multiplies the highest (fourth order) spatial derivative term in the governing equation, it is not too surprising that from a perturbation standpoint, the problem is singular and even quite small values of the surface tension parameter α significantly modify the behavior of the solution.

When the source strength is large enough, this model generates two travelling waves moving left and right away from the source region, connected through a steady state film profile directly over the source area. For sub-threshold source strengths, only left-going waves are observed, but there are two such waves that travel at different speeds. For any of the traveling waves that connect two flat regions (one possibly of zero height far to the left or right), a Rankine-Hugoniot equation can be obtained that relates the speed of the moving front to the constant heights on either side of the traveling "shock." This is easy to see by substituting a travelling wave ansatz $h(x,t) = h(z), z = x - ct$ into the PDE

$$h_t + (h^3 - h^2 + \alpha h^3 h_{xxx})_x = 0$$

away from the source region. This yields

$$-ch' + (h^3 - h^2 + \alpha h^3 h''')' = 0$$

with the prime denoting a z-derivative. Integrating the equation once, we have

$$h^3 - h^2 + \alpha h^3 h''' = ch + C,$$

where C is an integration constant. When a travelling wave connects uniform left and right regions with heights h_- and h_+, since $h(z)''' = 0$ as $z \to \pm\infty$, we find that

$$h_-^3 - h_-^2 - ch_- = h_+^3 - h_+^2 - ch_+ = C.$$

Film Height vs Distance at Various Times (S=4/20, α=0)

Film Height vs Distance at Various Times (S=4/20, α=0.001)
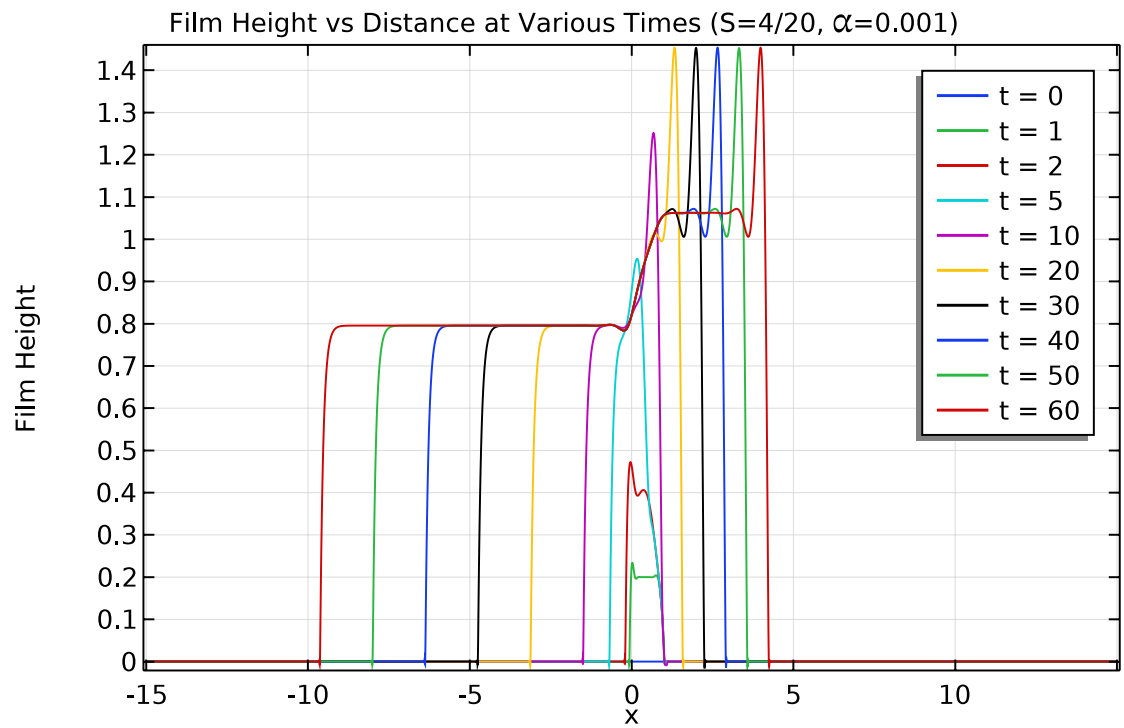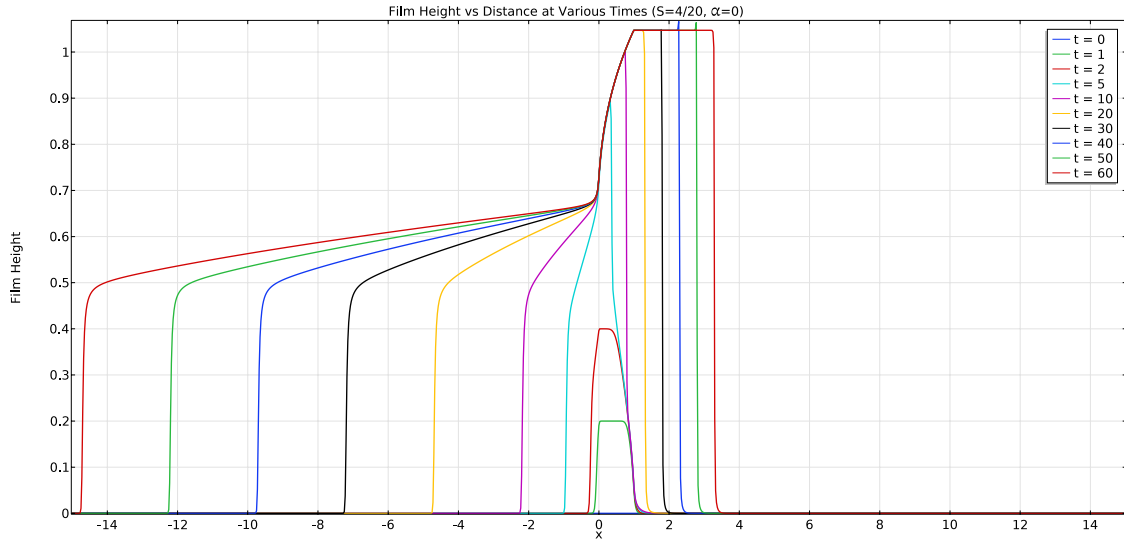
Figure 1.9: Comparison of models without and with surface tension.

The wave speed c can thus be obtained:

$$c = \frac{(h_-^3 - h_-^2) - (h_+^3 - h_+^2)}{h_- - h_+} = h_-^2 + h_- h_+ + h_+^2 - h_- - h_+$$

This is consistent with the Rankine-Hugoniot condition that $c = [\![q(h)]\!] / [\![h]\!]$, where $q(h)$ is the flux and double square brackets indicate the jump in the value of their argument from one side to the other.

From our numerical simulation results, we can verify that the travelling wave speed is indeed given by this equation. For instance, consider the small source condition depicted in the middle panel of Figure 1.6. We see two travelling waves both traveling to the left. Denote the flat part of the height profile from left to right as h_1, h_2, h_3; in that case:

$$h_1 = 0, \quad h_2 = 0.783, \quad h_3 = 0.384.$$

Denote the two wave speed from left to right as c_1 and c_2. The predicted wave speeds would thus be:

$$c_1 = h_1^2 + h_1 h_2 + h_2^2 - h_1 - h_2 = -0.170$$
$$c_2 = h_2^2 + h_2 h_3 + h_3^2 - h_2 - h_3 = -0.106.$$

These values closely match the results obtained from studying the plot and extracting the velocities.

In order to get some sense of the orders of magnitude of the parameters and the applicability of the lubrication approximation, let us consider a hypothetical case with the following physical parameters. Take the liquid and gas to be water and air at 25°C with respective properties: $\rho_w = 997$ kg/m^3, $\mu_w = 8.9 \times 10^{-4}$ kg/(m s), $\rho_a = 1.18$ kg/m^3 and $\mu_a = 1.85 \times 10^{-5}$ kg/(m s). Take the upward airflow velocity to be $U_a = 15$ m/s and suppose that a uniform flow of that speed encounters the vertical plate, developing a laminar (Blasius) boundary layer, reaching the liquid film about $\ell = 5$ cm from the bottom of the plate. In that case, the wall shear stress is given from

the standard expression for a laminar boundary layer on a flat plate, namely:

$$\tau = 0.332 \rho_a U_a^2 / \sqrt{Re_\ell}$$

in which the Reynolds number for the airflow is defined by $Re_\ell = \rho_a U_a \ell / \mu_a$. The resulting shear stress turns out to be $\tau = 0.404$ kg/(m s^2). The characteristic thickness of the film which is determined by a balance of gravity and airflow is thus calculated to be

$$H = \frac{3\tau}{2\rho_w g} \approx 62 \text{ microns}$$

and if the length of the source region is taken to be $L = 1$ cm, the lubrication parameter will be $\epsilon = H/L \approx 0.0062 \ll 1$. The velocity scale for the downward draining of the water film under gravity is given by $U = \rho_w g H^2 / \mu_w \approx 0.042$ m/s, making the Reynolds number for water flow to be $Re = \rho_w UL / \mu_w \approx 472$. While this value is not small, the product $\epsilon^2 Re = 0.018 \ll 1$, so the neglect of inertial terms in the thin film equation can be justified. Based on these values, the dimensional threshold value for the source strength is found to be

$$S_0 = \left(\frac{4}{27} \right) \left(\frac{9\tau^3}{8\mu_w \rho_w^2 g^2 L} \right) \approx 12.9 \text{ microns per second.}$$

Finally, for the dimensionless parameter $\alpha = \sigma H / (\rho_w g L^3)$ to have value 10^{-4}, the surface tension would have to be $\sigma = 0.0158$ kg/s^2, or ten times higher if $\alpha = 10^{-3}$. This is in the right range for water which has a surface tension of about 0.072 kg/s^2. So, although the dimensionless surface tension parameter α is indeed small for water, our analysis shows that the thin films that advance upward due to airflow, or fall due to gravity are still significantly affected by surface tension.

1.6 Appendix

1.6.1   MATLAB implementation of Godunov method for solving the simplified model

```
1  % Godunov  scheme
2  S_0  =  5/27;
```

```matlab
3   h_0 = 0;

4

5   xmin = -5;
6   xmax = 5;
7   dx = 0.025;
8   N = (xmax-xmin)/dx;
9   x = linspace(xmin,xmax,N+1);

10

11  x1 = linspace(xmin-dx,xmax+dx,N+3);

12

13  u = x.*0;
14  for i = 2:length(x1)-1
15      R = min(x1(i), 1);
16      L = max(x1(i-1), 0);
17      if R < L
18          u(i-1) = 0;
19      else
20          u(i-1) = 1/dx*(R - L)*h_0;
21      end

22

23  end

24

25

26  dt = 1/8*dx;
27  T = 20;
28  t_step = T/dt;

29

30  [X,Y] = meshgrid(x,0:dt:T);

31
```

```matlab
32  U_mesh = zeros(size(X));
33  U_mesh(1,:) = u;
34  for i = 1:t_step
35      for j = 2:N
36          R = min(x(j+1), 1);
37          L = max(x(j), 0);
38          if R >= L
39              u(j) = u(j) - dt/dx*( Q(u(j), u(j+1)) - Q(u(j-1), u(j)) -
                        (R - L)*S_0 );
40          else
41              u(j) = u(j) - dt/dx*( Q(u(j), u(j+1)) - Q(u(j-1), u(j)));
42          end
43          U_mesh(i+1,j) = u(j);
44      end
45  end
46
47  % figure;
48  % plot(x, u)
49  % xlim([-5, 5])
50  % ylim([0, 1.2])
51  % ax = gca; % current axes
52  % ax.FontSize = 16;
53  % l = line([-5,5],[2/3,2/3]);
54  % l.Color = 'r';
55  % l2 = line([-5,5],[1,1]);
56  % l2.Color = 'g';
57  % title(['Solution plot at t = ', num2str(T,'%d'), ' (S=', num2str(S_0)
          , ', h_0=', num2str(h_0,'%d'), ')'])
58  % saveas(gcf,['../../figure/final_step_plot_(T=', num2str(T,'%d'), '|S
```

```
     =',num2str(S_0),'|h_0=',num2str(h_0), ').png'])
59
60 % mesh plot
61 % surf(X, Y, U_mesh)
62 figure;
63 mesh(X, Y, U_mesh)
64 colormap(jet)     % change color map
65 shading interp
```

Chapter 2

Analysis of thin film equation with source

2.1 Introduction

The initial-boundary value problem:

$$
\begin{cases}
h_t = -(h^n h_{xxx})_x & \text{in } \Omega \times (0, T), \\
h_x = h_{xxx} = 0 & \text{on } \partial\Omega \times (0, T), \\
h(\cdot, 0) = h_0 & \text{in } \Omega
\end{cases}
\tag{2.1}
$$

is widely used to model time-evolution of the thickness $h(x, t)$ of a viscous liquid droplet spreading over a flat substrate. The value of the exponent n depends on a boundary condition imposed at the solid-liquid interface. For example, $n = 3$ corresponds to a no-slip boundary condition [45]. The case $n = 1$ appears in the modelling of the Darcy's flow inside the Hele-Shaw cell [30]. Different values of $n \in (1, 3)$ are also suggested to introduce the effects of strong or weak slippage [31]. Because the non-linear coefficient for the fourth-order derivative can be equal to zero (that corresponds to a dry area or a touchdown point) the problem above belongs to the wide class of higher order degenerate parabolic equations and has been studied extensively over last 30 years. The existence of generalized non-negative weak solutions, their qualitative behaviour, and regularity were rigorously analysed in [2, 3, 4, 6, 47]. The asymptotic properties of classical and weak solu-

tions for this thin-film model were obtained in [12, 13, 14]. Existence and qualitative behaviour of self-similar solutions were considered in [60, 61]. Thin-film equations on graphs were recently studied in [64]. One of the most well known and still open questions is the uniqueness of strong non-negative solutions (non-negative weak solutions with extra regularity properties). Some results in this direction, for particular classes of initial data, can be found in [18, 19]. Finite speed of the support propagation for the solution $h(x, t)$ and the existence of waiting time phenomenon were proved in [8, 48, 26, 27, 29].

Some modeling and experimental results were obtained for thin viscous liquid flows spreading from different type of sources. In [40], the author considered long-time and short-time asymptotic behaviour of a viscous flow down an inclined plane with point and line type sources. Numerical simulations in [40] were compared with experimental results. In [59], an evolution model was derived to fit data obtained from experiments with two fluids of different viscosity spreading over a solid surface with varying inclination angles from point sources. In [57], thin-film type model and numerical simulations were presented for the time-dependent three dimensional viscous liquid flow spreading down an inclined plane and originated from a continuous injection of liquid through a circular source.

Our motivation for introducing an additional source term to the classical thin-film model (2.1) originated from an industrial problem presented on the Mathematical Problems in Industry (MPI) workshop (Claremont, CA, June 2018). The problem concerned modelling dense porous catalysts in which a gaseous reaction constantly produces liquid in the interior of the catalyst (the source term), through the pores this liquid finds its way to the exterior surface, that results into forming and spreading droplets all over the surface. These droplets block the gaseous reactants from entering the pores and slow down the reaction.

To the best of the authors knowledge qualitative properties of weak solutions for an initial-boundary value problem for a thin-film equation with a source term has not been rigorously studied before. For the rest of this article, we are concerned with the following thin-film problem (one-dimensional version of the thin-film model with a source that was derived in [57]):

$$u_t + (u^n u_{xxx})_x = S(x) \text{ in } Q_T, \tag{2.2}$$

34

$$u_x = u_{xxx} = 0 \text{ on } \partial\Omega \times (0, T), \tag{2.3}$$

$$u(x, 0) = u_0(x), \tag{2.4}$$

where $\Omega \subset \mathbb{R}^1$ is bounded domain, $n > 0$ and $T > 0$. Assume that

$$0 \leqslant u_0(x) \in H^1(\Omega), \ S(x) \in H^1(\Omega). \tag{2.5}$$

Let us denote the initial total mass by $\mathcal{M} := \int_{\tilde{\Omega}} u_0(x) \, dx$ and the total source by $\mathcal{S} := \int_{\Omega} S(x) \, dx$.

Integrating (2.2) in Q_t and using boundary conditions, we obtain the total liquid mass at time t:

$$\int_{\Omega} u(x, t) \, dx = \mathcal{M} + t \, \mathcal{S}. \tag{2.6}$$

The chapter is structured as follows: in Section 2 we prove existence of weak solutions for $n > 0$ and show that under some restrictions on initial data these solutions can not deviate from a linear function. We provide an explicit example of initial data which satisfy our conditions. In Section 3 we consider a special case of a constant source term $S(x) = S_0$ and derive a long-time asymptotic behaviour of the non-negative solution. In Section 4 we study interface propagation properties for $1 < n < 2$. Numerical simulations of main results are presented in Section 5.

2.2 Existence of weak solutions

In this section, we define a generalized weak solution and prove its existence under some restrictions on the L^2-norm of the gradient of initial data. We do not assume positivity of the source term $S(x)$. Following [4] we define a weak solution.

Definition 2.2.1. *A generalized weak solution of problem (2.2)–(2.4) is a function $u(x,t)$ satisfying*

$$u \in C_{x,t}^{1/2,1/8}(\overline{Q}_T) \cap L^\infty(0,T;H^1(\Omega)), \tag{2.7}$$

$$u_t \in L^2(0,T;(H^1(\Omega))^*), \tag{2.8}$$

$$u \in C_{x,t}^{4,1}(\mathcal{P}_T), \quad |u|^{\frac{n}{2}} u_{xxx} \in L^2(\mathcal{P}_T), \tag{2.9}$$

where $\mathcal{P}_T = \overline{Q}_T \setminus (\{u = 0\} \cup \{t = 0\})$ and u satisfies (2.2) in the following sense:

$$\int_0^T \langle u_t(\cdot,t), \phi \rangle_{(H^1)^*,H^1} \, dt - \iint_{\mathcal{P}_T} |u|^n u_{xxx} \phi_x \, dxdt = \iint_{Q_T} S(x)\phi \, dxdt \tag{2.10}$$

for all $\phi \in L^2(0,T;H^1(\Omega))$;

$$u(\cdot,t) \to u(\cdot,0) = u_0 \text{ strongly in } H^1(\Omega) \text{ as } t \to 0, \tag{2.11}$$

$$\text{(2.3) hold at all points of the lateral boundary, where } \{u \neq 0\}. \tag{2.12}$$

Let us denote by $G_0(z)$ the following function

$$G_0(z) := \begin{cases} \frac{z^{2-n}}{(n-1)(n-2)} + \frac{A^{1-n}z}{n-1} + \frac{A^{2-n}}{2-n} & \text{if } n \neq \{1,2\}, \\ z \ln(\frac{z}{A}) - z + A & \text{if } n = 1, \\ \frac{z}{A} - \ln(\frac{z}{A}) - 1 & \text{if } n = 2, \end{cases} \tag{2.13}$$

where A is a positive constant.

Theorem 1. *Let $n > 1$. Then problem (2.2)—(2.4) has a weak solution $u(x,t)$ defined in Q_T for any $T > 0$, in the sense of Definition 1. Assume that the initial function u_0 satisfies*

$$\int_\Omega G_0(u_0) \, dx < \infty \text{ and } \|u_{0,x}\|_2 < \frac{\mathcal{M}}{|\Omega|}(\frac{\pi}{|\Omega|})^{\frac{1}{2}}.$$

Then there exists $T_{loc} > 0$ such that $u \in L^2(0,T_{loc};H^2(\Omega))$ is non-negative, where $T_{loc} = +\infty$ if $\|S'\|_2 <$

$\frac{\mathcal{S}}{|\Omega|}(\frac{\pi}{|\Omega|})^{\frac{1}{2}}$. *Moreover, if $\mathcal{S} > 0$ then there exists a constant $K_0 > 0$ such that*

$$\|u - \tfrac{\mathcal{M}}{|\Omega|} - t\tfrac{\mathcal{S}}{|\Omega|}\|_{H^1(\Omega)} \leqslant K_0 \quad \forall t > 0. \tag{2.14}$$

Note that, in the case of $S(x) \geqslant 0$, the condition $\|u_{0,x}\|_2 < \frac{\mathcal{M}}{|\Omega|}(\frac{\pi}{|\Omega|})^{\frac{1}{2}}$ and the restriction $\|S'\|_2 < \frac{\mathcal{S}}{|\Omega|}(\frac{\pi}{|\Omega|})^{\frac{1}{2}}$ can be eliminated.

Remark 2.2.1. *To compare to the existence result for the classical thin-film equation without a source term our Theorem 1 imposes the additional restrictions for the initial data and the source term in order to construct more regular (strong) non-negative solutions. This restrictions can be omitted in the proof of existence of weak solutions. The condition $\|u_{0,x}\|_2 < \frac{\mathcal{M}}{|\Omega|}(\frac{\pi}{|\Omega|})^{\frac{1}{2}}$ is true, for example, if $u_0(x) = A + B\sin(x)$ in $\Omega = (-\pi, \pi)$ with $A > |B|\sqrt{2\pi}$.*

Proof. Following [4], for a given $\varepsilon > 0$ we consider the following regularized problem:

$$u_t + (f_{\varepsilon\delta}(u)u_{xxx})_x = S_\varepsilon(x) \text{ in } Q_T, \tag{2.15}$$

$$u_x = u_{xxx} = 0 \text{ on } \partial\Omega \times (0, T), \tag{2.16}$$

$$u(x, 0) = u_{0,\varepsilon\delta}(x), \tag{2.17}$$

where

$$f_{\varepsilon\delta}(z) := \tfrac{|z|^{n+4}}{|z|^4 + \delta|z|^n} + \varepsilon, \ S_\varepsilon(x) \in C^{4+\gamma}(\bar{\Omega}),$$

$$u_{0,\varepsilon\delta}(x) \geqslant u_0(x) + \delta^\theta, \ u_{0,\varepsilon\delta}(x) \to u_0(x) \text{ strongly in } H^1(\Omega) \text{ as } \varepsilon, \delta \to 0,$$

$$S_\varepsilon(x) \to S(x) \text{ strongly in } H^1(\Omega) \text{ as } \varepsilon \to 0,$$

where $\gamma \in (0, 1)$ and $\theta \in (0, \frac{1}{2})$.

The existence of classical solutions for the regularized parabolic equation follows from [24]. To pass to the limits $\varepsilon \to 0$, $\delta \to 0$ we first need to obtain uniform in ε, δ a priori estimates [4].

37

Integrating (2.15) in Q_t, we get

$$\int_\Omega (u - \tfrac{\mathcal{M}_{\varepsilon\delta}}{|\Omega|} - t\tfrac{\mathcal{S}_\varepsilon}{|\Omega|})\,dx = 0. \tag{2.18}$$

By (2.18) and the Poincare inequality we find that

$$|u - \tfrac{\mathcal{M}_{\varepsilon\delta}}{|\Omega|} - t\tfrac{\mathcal{S}_\varepsilon}{|\Omega|}| \leqslant (\tfrac{|\Omega|}{\pi})^{\frac12}\left(\int_\Omega u_x^2\,dx\right)^{\frac12}, \tag{2.19}$$

$$\int_\Omega (u - \tfrac{\mathcal{M}_{\varepsilon\delta}}{|\Omega|} - t\tfrac{\mathcal{S}_\varepsilon}{|\Omega|})^2\,dx \leqslant (\tfrac{|\Omega|}{\pi})^2 \int_\Omega u_x^2\,dx. \tag{2.20}$$

Multiplying (2.15) by $-u_{xx}$ and integrating over Ω, we obtain

$$\tfrac12 \tfrac{d}{dt}\|u_x\|_2^2 + \int_\Omega f_{\varepsilon\delta}(u)u_{xxx}^2\,dx = -\int_\Omega S_\varepsilon(x)u_{xx}\,dx \leqslant \|S_\varepsilon'\|_2\|u_x\|_2. \tag{2.21}$$

Next, a solution of inequality (2.21) compares with the corresponding equation. As a result, we deduce that

$$\|u_x\|_2 \leqslant \|u_{0\varepsilon\delta,x}\|_2 + t\,\|S_\varepsilon'\|_2 \quad \forall\, t \geqslant 0. \tag{2.22}$$

By (2.19), (2.20), and (2.22) we get

$$\|u\|_{H^1(\Omega)}^2 \leqslant (1 + (\tfrac{|\Omega|}{\pi})^2)(\|u_{0\varepsilon\delta,x}\|_2 + t\,\|S_\varepsilon'\|_2)^2 + \tfrac{(\mathcal{M}_{\varepsilon\delta}+t\mathcal{S}_\varepsilon)^2}{|\Omega|} \quad \forall\, t \geqslant 0, \tag{2.23}$$

$$v_{\varepsilon\delta}(t) := \tfrac{\mathcal{M}_{\varepsilon\delta}}{|\Omega|} + t\tfrac{\mathcal{S}_\varepsilon}{|\Omega|} - (\tfrac{|\Omega|}{\pi})^{\frac12}(\|u_{0\varepsilon\delta,x}\|_2 + t\,\|S_\varepsilon'\|_2) \leqslant u(x,t) \leqslant$$
$$\Lambda_{\varepsilon\delta}(t) := \tfrac{\mathcal{M}_{\varepsilon\delta}}{|\Omega|} + t\tfrac{\mathcal{S}_\varepsilon}{|\Omega|} + (\tfrac{|\Omega|}{\pi})^{\frac12}(\|u_{0\varepsilon\delta,x}\|_2 + t\,\|S_\varepsilon'\|_2) \quad \forall\, t \geqslant 0. \tag{2.24}$$

Next, we will assume that

$$v_{\varepsilon\delta}(t) \to v_\delta(t) > 0 \text{ as } \varepsilon \to 0. \tag{2.25}$$

Hence,

if $\tfrac{\mathcal{M}_{\varepsilon\delta}}{|\Omega|} > (\tfrac{|\Omega|}{\pi})^{\frac12}\|u_{0\varepsilon\delta,x}\|_2$ and $\tfrac{\mathcal{S}_\varepsilon}{|\Omega|} \geqslant (\tfrac{|\Omega|}{\pi})^{\frac12}\|S_\varepsilon'\|_2$ then (2.25) is true for all $t \geqslant 0$;

if $\frac{\mathcal{M}_{\varepsilon\delta}}{|\Omega|} > (\frac{|\Omega|}{\pi})^{\frac{1}{2}} \|u_{0\varepsilon\delta,x}\|_2$ and $\frac{\mathcal{S}_\varepsilon}{|\Omega|} < (\frac{|\Omega|}{\pi})^{\frac{1}{2}} \|S'_\varepsilon\|_2$ then (2.25) holds for all $0 \leqslant t \leqslant T^*$,

where $T^* := \dfrac{\frac{\mathcal{M}_{\varepsilon\delta}}{|\Omega|} - (\frac{|\Omega|}{\pi})^{\frac{1}{2}} \|u_{0\varepsilon\delta,x}\|_2}{(\frac{|\Omega|}{\pi})^{\frac{1}{2}} \|S'_\varepsilon\|_2 - \frac{\mathcal{S}_\varepsilon}{|\Omega|}}$. Note that $T^* \leqslant -\frac{\mathcal{M}_{\varepsilon\delta}}{\mathcal{S}_\varepsilon}$ if $\mathcal{S}_\varepsilon < 0$.

Let us denote by

$$G_{\varepsilon\delta}(z) := \int\limits_A^z \int\limits_A^v \frac{ds\,dv}{f_{\varepsilon\delta}(s)} \geqslant 0 : G'_{\varepsilon\delta}(z) = \int\limits_A^z \frac{dv}{f_{\varepsilon\delta}(v)} \leqslant 0 \ \forall z \leqslant A, \ G''_{\varepsilon\delta}(z) = \frac{1}{f_{\varepsilon\delta}(z)} \ \forall z \in \mathbb{R}^1,$$

where $A > 0$. Multiplying (2.15) by $G'_{\varepsilon\delta}(u)$ and integrating over Ω, we obtain

$$\frac{d}{dt} \int\limits_\Omega G_{\varepsilon\delta}(u)\,dx + \int\limits_\Omega u_{xx}^2\,dx = \int\limits_\Omega S_\varepsilon(x) G'_{\varepsilon\delta}(u)\,dx.$$

Note that if $\mathcal{S} > 0$ and $n > 1$ then

$$\int\limits_\Omega S(x) G'_0(u)\,dx = \frac{1}{n-1} \int\limits_\Omega S(x)(A^{1-n} - u^{1-n})\,dx \leqslant 0 \Leftrightarrow$$

$$A^{1-n}\mathcal{S} \leqslant \int\limits_\Omega S_+(x) u^{1-n}\,dx + \int\limits_\Omega S_-(x) u^{1-n}\,dx \leqslant v^{1-n}(t) \int\limits_\Omega S_+(x)\,dx +$$

$$\Lambda^{1-n}(t) \int\limits_\Omega S_-(x)\,dx = \Lambda^{1-n}\mathcal{S} + (v^{1-n}(t) - \Lambda^{1-n}(t)) \int\limits_\Omega S_+(x)\,dx \text{ provided } A = \Lambda(t).$$

Similarly, if $\mathcal{S} < 0$ and $n > 1$ then

$$\int\limits_\Omega S(x) G'_0(u)\,dx \geqslant 0.$$

As

$$|G'_{\varepsilon\delta}(u)| \leqslant L_{\varepsilon\delta}(t) := \frac{1}{|n-1|}(v_{\varepsilon\delta}^{1-n}(t) + A^{1-n}) + \frac{\delta}{3}(v_{\varepsilon\delta}^{-3}(t) + A^{-3})$$

then we find that

$$\int\limits_\Omega G_{\varepsilon\delta}(u)\,dx + \iint\limits_{Q_t} u_{xx}^2\,dxdt \leqslant \int\limits_\Omega G_{\varepsilon\delta}(u_{0,\varepsilon\delta})\,dx + \|S_\varepsilon\|_1 \int\limits_0^t L_{\varepsilon\delta}(s)\,ds. \qquad (2.26)$$

In the case of $\mathcal{S} > 0$, we can refine (2.26). Really, if we take $A = \Lambda(t)$ then

$$\int\limits_\Omega G_{\varepsilon\delta}(u)\,dx + \iint\limits_{Q_t} u_{xx}^2\,dxdt - \iint\limits_{Q_t} S_\varepsilon(x) G'_{\varepsilon\delta}(u)\,dxdt = \int\limits_\Omega G_{\varepsilon\delta}(u_{0,\varepsilon\delta})\,dx. \qquad (2.27)$$

39

Letting $\varepsilon \to 0$, due to (2.22) and (2.26) (or (2.27)), we obtain an unique classical solution $u_\delta > 0$ in $Q_{T_{loc}}$.

Following [4], we will refine (2.22) for $u_\delta > 0$, in the case $\mathcal{S} > 0$. Applying [66, Lemma 1] to $u_\delta > 0$, due to (2.27) with $\varepsilon = 0$, we have

$$\tfrac{9}{16}\left(\int\limits_\Omega u_x^2\, dx\right)^2 \leqslant \int\limits_\Omega f_\delta(u)u_{xxx}^2\, dx \int\limits_\Omega \tfrac{u^2}{f_\delta(u)}\, dx \leqslant C_n \int\limits_\Omega G_\delta(u_{0,\delta})\, dx \int\limits_\Omega f_\delta(u)u_{xxx}^2\, dx. \tag{2.28}$$

Let us denote by

$$J[u] := \int\limits_\Omega u_x^2\, dx.$$

Also, following [66], we can show that there exists $C_1 > 0$ such that

$$\int\limits_\Omega f_\delta(u)u_{xxx}^2\, dx \geqslant C_1 J[u]. \tag{2.29}$$

Using (2.21) with $\varepsilon = 0$, due to (2.29), we deduce that

$$\tfrac{d}{dt}J[u] + 2C_1 J[u] \leqslant 2\|S'\|_2 J^{\frac{1}{2}}[u]. \tag{2.30}$$

Next, a solution of inequality (2.30) compares with a one of Bernoulli equation. By (2.30) it follows that

$$\|u_x\|_2 \leqslant e^{-C_1 t}\|u_{0\delta,x}\|_2 + \tfrac{\|S'\|_2}{C_1}(1 - e^{-C_1 t}) \to \tfrac{\|S'\|_2}{C_1} \text{ as } t \to +\infty. \tag{2.31}$$

By (2.20) and (2.31) the estimate (2.14) follows. $\qquad\square$

2.3 Long-time behaviour of solutions for the constant source

In this section, for a special case when the source term is a constant, we obtain stronger results for a long-time asymptotic behaviour of a solution. We would like to point out that due to non-linearity the constant source term can not be eliminated by some simple change of variables.

Let $S(x) = S_0$ and $u_s(t)$ be such that

$$u_s(t) = \tfrac{\mathcal{M}}{|\Omega|} + t\, S_0, \text{ where } S_0 \geqslant 0. \tag{2.32}$$

If $S_0 < 0$ and a weak solution $u(x,t)$ is non-negative then, due to (2.6), we obtain that

$$u(x,t) \to 0 \text{ as } t \to T^* := -\frac{\mathcal{M}}{S_0|\Omega|}$$

that means that the thin-film will completely dry out over the finite time T^*.

Theorem 2. *Let u_s be defined in (2.32), and u be a weak solution from Theorem 1. Then*

$$u(x,t) \to u_s(t) \text{ strongly in } H^1(\Omega) \text{ as } t \to +\infty.$$

Proof. We want to show the following convergence

$$w(x,t) := u(x,t) - u_s(t) \to 0 \text{ as } t \to +\infty. \tag{2.33}$$

Note that $w = w_\delta(x,t)$ is a solution to the following problem

$$w_t + (f_\delta(u)w_{xxx})_x = 0 \text{ in } Q_T, \tag{2.34}$$

$$w_x = w_{xxx} = 0 \text{ on } \partial\Omega \times (0,T),$$

$$w(x,0) = w_{0\delta}(x) := u_{0\delta}(x) - \frac{\mathcal{M}_\delta}{|\Omega|}.$$

Also, we have

$$\int_\Omega w(x,t)\,dx = 0. \tag{2.35}$$

Multiplying (2.34) by $-w_{xx}$, we obtain

$$\tfrac{1}{2}\tfrac{d}{dt}\int_\Omega w_x^2\,dx + \int_\Omega f_\delta(u)w_{xxx}^2\,dx = 0. \tag{2.36}$$

As

$$\|u_x(t)\|_2 \leqslant \|u_{0\delta,x}\|_2$$

then by (2.19)

$$u(x,t) \geqslant v_\delta(t) := \frac{\mathcal{M}_\delta}{|\Omega|} + t\,S_0 - \left(\frac{|\Omega|}{\pi}\right)^{\frac{1}{2}}\|u_{0\delta,x}\|_2 > 0 \tag{2.37}$$

41

for all

$$t \geqslant T_0 := S_0^{-1}\big[\big(\tfrac{|\Omega|}{\pi}\big)^{\frac{1}{2}}\|u_{0,x}\|_2 - \tfrac{\mathcal{M}}{|\Omega|}\big]_+.$$

Applying the Poincaré inequality twice, we find that

$$\int_\Omega w_x^2 \, dx \leqslant \big(\tfrac{|\Omega|}{\pi}\big)^4 \int_\Omega w_{xxx}^2 \, dx. \tag{2.38}$$

Now, using (2.37) and (2.38), by (2.36) we get

$$\tfrac{d}{dt} \int_\Omega w_x^2 \, dx + a_\delta(t) \int_\Omega w_x^2 \, dx \leqslant 0 \quad \forall\, t \geqslant T_0, \tag{2.39}$$

where

$$a_\delta(t) := \big(\tfrac{\pi}{|\Omega|}\big)^4 f_\delta(\nu_\delta(t)).$$

From (2.39) we find that

$$\int_\Omega w_x^2 \, dx \leqslant \|w_x(T_0)\|_2^2 \, e^{-\int_{T_0}^t a_\delta(s)\,ds} \leqslant \|u_{0\delta,x}\|_2^2 \, e^{-\int_{T_0}^t a_\delta(s)\,ds} \quad \forall\, t \geqslant T_0. \tag{2.40}$$

By (2.40) and the Poincaré inequality we deduce that

$$\|w(t)\|_{H^1}^2 \leqslant \big(1 + \big(\tfrac{|\Omega|}{\pi}\big)^2\big)\|u_{0\delta,x}\|_2^2 \, e^{-\int_{T_0}^t a_\delta(s)\,ds} \quad \forall\, t \geqslant T_0. \tag{2.41}$$

Hence, letting $\delta \to 0$ in (2.41), we have

$$\|w\|_{H^1}^2 \leqslant A\,e^{-B(t)} \to 0 \text{ as } t \to +\infty,$$

where

$$A := \big(1 + \big(\tfrac{|\Omega|}{\pi}\big)^2\big)\|u_{0x}\|_2^2, \; B(t) := \int_{T_0}^t a_0(s)\,ds.$$

As a result, we obtain that

$$w(x,t) \to 0 \text{ strongly in } H^1(\Omega) \text{ as } t \to +\infty.$$

42

2.4 Qualitative behaviour of solutions

In this section, we will prove finite speed of support propagation and also find sufficient conditions for a waiting phenomenon.

2.4.1 Local entropy estimate

Let us denote by

$$\tilde{G}_\delta(z) := \int_A^z \int_A^v \frac{s^\alpha \, ds \, dv}{f_\delta(s)} \geqslant 0 : \tilde{G}'_\delta(z) = \int_A^z \frac{v^\alpha dv}{f_\delta(v)} \leqslant 0 \; \forall \, z \in [0, A], \; \tilde{G}''_\delta(z) = \frac{z^\alpha}{f_\delta(z)} \; \forall \, z \in \mathbb{R}^+.$$

Lemma 2.4.1. *Let $n \in (0, 2)$. Let be $\zeta \in C_{t,x}^{1,2}(\bar{Q}_T)$ such that $\text{supp} \, \zeta \subset \Omega$, $(\zeta^4)' = 0$ on $\partial\Omega$. Assume that $-\frac{1}{2} < \alpha < 1$, and $\alpha \neq 0$. Then there exist constants $C_i \; (i = 1, 2)$ dependent on α and n, independent of Ω, such that for all $T > 0$*

$$\int_\Omega v^{\frac{2(\alpha-n+2)}{\alpha+2}} \zeta^4(x, T) \, dx - \iint_{Q_T} v^{\frac{2(\alpha-n+2)}{\alpha+2}} (\zeta^4)_t \, dxdt + C_1 \iint_{Q_T} v_{xx}^2 \zeta^4 \, dxdt -$$

$$\iint_{Q_T} S(x) v^{\frac{2(\alpha-n+1)}{\alpha+2}} \zeta^4 \, dxdt \leqslant \int_\Omega v_0^{\frac{2(\alpha-n+2)}{\alpha+2}} \zeta^4(x, 0) \, dx + C_2 \iint_{Q_T} v^2 (\zeta_x^4 + \zeta^2 \zeta_{xx}^2) \, dxdt \quad (2.42)$$

for any $\alpha \in (\max\{-\frac{1}{2}, n-1\}, 1)$, where $v := u^{\frac{\alpha+2}{2}}$.

Proof. Let $u := u_\delta > 0$. Multiplying (2.2) by $\tilde{G}'_\delta(u)\varphi$ and integrating over Ω, we have

$$\frac{d}{dt} \int_\Omega \tilde{G}_\delta(u)\varphi \, dx - \int_\Omega \tilde{G}_\delta(u)\varphi_t \, dx + \int_\Omega u^\alpha u_{xx}^2 \varphi \, dx - \frac{\alpha(\alpha-1)}{3} \int_\Omega u^{\alpha-2} u_x^4 \varphi \, dx -$$

$$\int_\Omega S(x)\tilde{G}'_\delta(u)\varphi \, dx = \frac{\alpha}{6} \int_\Omega u^{\alpha-1} u_x^3 \varphi_x \, dx + \frac{1}{2} \int_\Omega u^\alpha u_x^2 \varphi_{xx} \, dx. \quad (2.43)$$

Note that

$$\frac{\alpha}{6} \int_\Omega u^{\alpha-1} u_x^3 \varphi_x \, dx \leqslant \epsilon_1 \int_\Omega u^{\alpha-2} u_x^4 \varphi \, dx + C(\epsilon_1) \int_\Omega u^{\alpha+2} \frac{\varphi_x^4}{\varphi^3} \, dx \; \forall \, \epsilon_1 > 0,$$

43

$$\frac{1}{2}\int_\Omega u^\alpha u_x^2 \varphi_{xx}\, dx \leqslant \epsilon_2 \int_\Omega u^{\alpha-2}u_x^4 \varphi\, dx + C(\epsilon_2) \int_\Omega u^{\alpha+2}\frac{\varphi_{xx}^2}{\varphi}\, dx \ \forall\, \epsilon_2 > 0.$$

Using these estimates in (2.43), we obtain

$$\frac{d}{dt}\int_\Omega \tilde{G}_\delta(u)\varphi\, dx - \int_\Omega \tilde{G}_\delta(u)\varphi_t\, dx + \int_\Omega u^\alpha u_{xx}^2 \varphi\, dx + \left(\frac{\alpha(1-\alpha)}{3} - \epsilon_1 - \epsilon_2\right)\int_\Omega u^{\alpha-2}u_x^4 \varphi\, dx -$$

$$\int_\Omega S(x)\tilde{G}_\delta'(u)\varphi\, dx \leqslant C(\epsilon_1)\int_\Omega u^{\alpha+2}\frac{\varphi_x^4}{\varphi^3}\, dx + C(\epsilon_2)\int_\Omega u^{\alpha+2}\frac{\varphi_{xx}^2}{\varphi}\, dx. \quad (2.44)$$

As

$$u^\alpha u_{xx}^2 = \left(\frac{2}{\alpha+2}\right)^2 \left(u^{\frac{\alpha+2}{2}}\right)_{xx}^2 - \alpha u^{\alpha-1}u_x^2 u_{xx} - \left(\frac{\alpha}{2}\right)^2 u^{\alpha-2}u_x^4$$

then

$$\int_\Omega u^\alpha u_{xx}^2 \varphi\, dx = \left(\frac{2}{\alpha+2}\right)^2 \int_\Omega \left(u^{\frac{\alpha+2}{2}}\right)_{xx}^2 \varphi\, dx - \alpha \int_\Omega u^{\alpha-1}u_x^2 u_{xx}\varphi\, dx -$$

$$\left(\frac{\alpha}{2}\right)^2 \int_\Omega u^{\alpha-2}u_x^4 \varphi\, dx = \left(\frac{2}{\alpha+2}\right)^2 \int_\Omega \left(u^{\frac{\alpha+2}{2}}\right)_{xx}^2 \varphi\, dx + \left(\frac{\alpha(\alpha-1)}{3} - \left(\frac{\alpha}{2}\right)^2\right)\int_\Omega u^{\alpha-2}u_x^4 \varphi\, dx +$$

$$\frac{\alpha}{3}\int_\Omega u^{\alpha-1}u_x^3 \varphi_x\, dx \geqslant \left(\frac{2}{\alpha+2}\right)^2 \int_\Omega \left(u^{\frac{\alpha+2}{2}}\right)_{xx}^2 \varphi\, dx + \left(\frac{\alpha(\alpha-4)}{12} - \epsilon\right)\int_\Omega u^{\alpha-2}u_x^4 \varphi\, dx -$$

$$C_\epsilon(\alpha)\int_\Omega u^{\alpha+2}\frac{\varphi_x^4}{\varphi^3}\, dx. \quad (2.45)$$

By (2.45), using in the case $\alpha \in [0, 4] \setminus \{1\}$ the following estimate

$$\int_\Omega u^{\alpha-2}u_x^4 \varphi\, dx \leqslant C(\alpha)\int_\Omega u^{\alpha+2}\frac{\varphi_x^4}{\varphi^3}\, dx + \frac{9(1+\epsilon_0)}{(\alpha-1)^2}\int_\Omega u^\alpha u_{xx}^2 \varphi\, dx \ \forall\, \epsilon_0 \in (0,1), \quad (2.46)$$

we have

$$\left(\frac{2}{\alpha+2}\right)^2 \left(1 + \frac{9(1+\epsilon_0)}{(\alpha-1)^2}\left(\frac{\alpha(\alpha-4)}{12}\right)_+\right)^{-1}\int_\Omega \left(u^{\frac{\alpha+2}{2}}\right)_{xx}^2 \varphi\, dx - C(\alpha)\int_\Omega u^{\alpha+2}\frac{\varphi_x^4}{\varphi^3}\, dx \leqslant \int_\Omega u^\alpha u_{xx}^2 \varphi\, dx. \quad (2.47)$$

Using (2.47) in (2.44), we deduce that

$$\frac{d}{dt}\int_\Omega \tilde{G}_\delta(u)\varphi\,dx - \int_\Omega \tilde{G}_\delta(u)\varphi_t\,dx + C_1\int_\Omega (u^{\frac{\alpha+2}{2}})^2_{xx}\varphi\,dx - \int_\Omega S(x)\tilde{G}'_\delta(u)\varphi\,dx \leqslant$$

$$C_2\int_\Omega u^{\alpha+2}\big(\tfrac{\varphi_x^4}{\varphi^3} + \tfrac{\varphi_{xx}^2}{\varphi}\big)\,dx \quad (2.48)$$

provided $\alpha \in (0,1)$. If $\alpha \leqslant 0$ then, using (2.46) in (2.44), we get (2.48) provided

$$1 - \tfrac{\alpha(\alpha-1)}{3}\tfrac{9(1+\epsilon_0)}{(\alpha-1)^2} = \tfrac{1+\alpha(2+3\epsilon_0)}{1-\alpha} > 0 \Rightarrow \alpha > -\tfrac{1}{2+3\epsilon_0}.$$

After integrating (2.48) in time, we have

$$\int_\Omega \tilde{G}_\delta(u)\varphi\,dx - \iint_{Q_T} \tilde{G}_\delta(u)\varphi_t\,dxdt + C_1\iint_{Q_T} (u^{\frac{\alpha+2}{2}})^2_{xx}\varphi\,dxdt - \iint_{Q_T} S(x)\tilde{G}'_\delta(u)\varphi\,dxdt \leqslant$$

$$\int_\Omega \tilde{G}_\delta(u_0)\varphi(x,0)\,dx + C_2\iint_{Q_T} u^{\alpha+2}\big(\tfrac{\varphi_x^4}{\varphi^3} + \tfrac{\varphi_{xx}^2}{\varphi}\big)\,dxdt \quad (2.49)$$

for any $\alpha \in (-\tfrac{1}{2},1)$. Taking $\varphi(x,t) = \zeta^4(x,t)$ in (2.49) and letting $\delta \to 0$, we obtain (2.42). $\qquad\square$

2.4.2 Finite speed of propagation

Let $\Omega = (-a,a)$. Assume that

$$\operatorname{supp} u_0 \subseteq \Omega \setminus (-b,b), \text{ and } \operatorname{supp} S(x) \subseteq \Omega \setminus (-b,b), \quad b \in (0,a). \quad (2.50)$$

Theorem 3. *Let $1 < n < 2$. Assume that $0 \leqslant u_0 \in H^1(\Omega)$ and $0 \leqslant S(x) \in H^1(\Omega)$ satisfy (2.50).*
Then the solution u of Theorem 1 has finite speed of propagation for all $t \geqslant 0$, i.e. there exists a continuous
function $\Gamma(t)$, $\Gamma(0) = b$ such that $\operatorname{supp} u(t,.) \subset \Omega \setminus (-\Gamma(t), \Gamma(t))$.

Proof. For an arbitrary $s \in [0,a)$ and $\delta \in (0,s)$ we consider the families of sets

$$\Omega(s) := \{x \in \bar{\Omega} : |x| \leqslant s\}, \; Q_T(s) = (0,T) \times \Omega(s),$$

$$K_T(s,\delta) = Q_T(s) \setminus Q_T(s-\delta). \quad (2.51)$$

We introduce a non-negative cut-off function $\eta(\tau)$ from the space $C^2(\mathbb{R}^1)$ with the following properties:

$$\eta(\tau) = \begin{cases} 1 & \text{if } \tau \leqslant 0, \\ -\tau^3(6\tau^2 - 15\tau + 10) + 1 & \text{if } 0 < \tau < 1, \\ 0 & \text{if } \tau \geqslant 1. \end{cases} \tag{2.52}$$

Next we introduce our main cut-off functions $\eta_{s,\delta}(x) \in C^2(\bar{\Omega})$ such that $0 \leqslant \eta_{s,\delta}(x) \leqslant 1 \ \forall\, x \in \bar{\Omega}$ and possess the following properties:

$$\eta_{s,\delta}(x) = \eta\left(\frac{|x| - s + \delta}{\delta}\right) = \begin{cases} 1, x \in \Omega(s - \delta), \\ 0, x \in \Omega \setminus \Omega(s), \end{cases} \tag{2.53}$$

$$|(\eta_{s,\delta})_x| \leqslant \tfrac{15}{8\delta}, \ |(\eta_{s,\delta})_{xx}| \leqslant \tfrac{5(\sqrt{3}-1)}{\delta^2}$$

for all $s \in [0, a)$ and $\delta \in (0, s)$. Taking into account

$$\iint\limits_{Q_T(s)} S(x) v^{\frac{2(\alpha - n + 1)}{\alpha + 2}} \zeta^4 \, dx dt \leqslant \epsilon \sup_{t \in (0,T)} \int\limits_{\Omega(s)} v^{\frac{2(\alpha - n + 2)}{\alpha + 2}} \zeta^4 \, dx dt +$$

$$C(\epsilon) T^{\alpha - n + 2} \int\limits_{\Omega(s)} S^{\alpha - n + 2}(x) \zeta^4 \, dx$$

and choosing $\zeta^4(x, t) = \eta_{s,\delta}(x) e^{-\frac{t}{T}}$ in (2.42), we arrive at

$$\sup_{t \in (0,T)} \int\limits_{\Omega(s-\delta)} v^{\frac{2(\alpha - n + 2)}{\alpha + 2}}(t)\, dx + \tfrac{C}{T} \iint\limits_{Q_T(s-\delta)} v^{\frac{2(\alpha - n + 2)}{\alpha + 2}} \, dx dt + C_1 \iint\limits_{Q_T(s-\delta)} v_{xx}^2 \, dx dt$$

$$\leqslant e \int\limits_{\Omega(s)} v_0^{\frac{2(\alpha - n + 2)}{\alpha + 2}} \, dx + \tfrac{C_2}{\delta^4} \iint\limits_{K_T(s,\delta)} v^2 \, dx dt + C_3 T^{\alpha - n + 2} \int\limits_{\Omega(s)} S^{\alpha - n + 2}(x)\, dx \quad (2.54)$$

for all $s \in [0, a)$ and $\delta \in (0, s)$, where $\alpha \in (n - 1, 1)$.

By (2.50) from (2.54) we deduce that

$$\int\limits_{\Omega(s-\delta)} v^{\frac{2(\alpha-n+2)}{\alpha+2}}(T)\,dx + \frac{C}{T}\iint\limits_{Q_T(s-\delta)} v^{\frac{2(\alpha-n+2)}{\alpha+2}}\,dxdt +$$

$$C_1 \iint\limits_{Q_T(s-\delta)} v_{xx}^2\,dxdt \leqslant R_T(s) := \frac{C_2}{\delta^4}\iint\limits_{Q_T(s)} v^2\,dxdt \quad (2.55)$$

for all $s \in [0, b]$, $\delta \in (0, s)$, and for any $\alpha \in (n-1, 1)$.

We apply Lemma A.1 in the region $\Omega(s-\delta)$ to a function v with $a = d = j = 2$, $b_1 = \frac{2(\alpha-n+2)}{\alpha+2}$, $k = 0$, $N = 1$, and $\theta_1 = \frac{n}{4(\alpha+2)-3n}$. Integrating the resulted inequality with respect to time and taking into account (2.55), we arrive at the following relation:

$$A_T(s-\delta) \leqslant C\,T^{1-\theta_1}\big(R_T(s)\big)^{1+\kappa_1} + C\,T\big(R_T(s)\big)^{1+\kappa_2}, \quad (2.56)$$

where

$$A_T(s) := \iint\limits_{Q_T(s)} v^2 dxdt, \quad \kappa_1 = \frac{n(1-\theta_1)}{\alpha-n+2} = \frac{4n}{4(\alpha+2)-3n}, \quad \kappa_2 = \frac{n}{\alpha-n+2}.$$

By (2.56) we have

$$A_T(s-\delta) \leqslant \frac{C_0\,T^{1-\theta_1}}{\delta^{4(1+\kappa_1)}} A_T^{1+\kappa_1}(s), \quad (2.57)$$

where C_0 is independent of T. Applying Lemma A.2 to (2.57), we deduce that

$$A_T(s) \equiv 0\ \forall s \leqslant b - 2^{\frac{1+\kappa_1}{\kappa_1}}\big(C_0\,T^{1-\theta_1}\big)^{\frac{1}{4(1+\kappa_1)}} A_T^{\frac{\kappa_1}{4(1+\kappa_1)}}(b).$$

As

$$A_T(b) \leqslant A_T(a) \leqslant C_0\,T^{1-\theta_1}\big(\|u_0\|_{\alpha-n+2}^{\alpha-n+2} + C_3 T^{\alpha-n+2}\|S\|_{\alpha-n+2}^{\alpha-n+2}\big)^{1+\kappa_1}$$

then

$$A_T(s) \equiv 0\ \forall s \leqslant \Gamma(T) := b - \tilde{C}_0\,T^{\frac{1-\theta_1}{4}}\big(\|u_0\|_{\alpha-n+2}^{\alpha-n+2} + C_3 T^{\alpha-n+2}\|S\|_{\alpha-n+2}^{\alpha-n+2}\big)^{\frac{\kappa_1}{4}},$$

whence

$$u(x,t) \equiv 0\ \forall\,(x,t) \in [-\Gamma(T), \Gamma(T)] \times \mathbb{R}^+.$$

47

Letting $\alpha \to n - 1$, we get

$$\Gamma_{opt}(T) = b - \tilde{C}_0 \, T^{\frac{1}{n+4}} (\|u_0\|_1 + T\|S\|_1)^{\frac{n}{n+4}}.$$

Remark 2.4.1. *Without the source term (for $S(x) = 0$) the exact exponent is $\frac{1}{n+4}$ (for small time values) and the exact exponent is 1 that corresponds to a travelling wave behaviour (for long time values). The exact exponent $\frac{1}{n+4}$ was previously obtained for self-similar solutions in [5]. We can also see that the source term $S(x) > 0$ speeds up propagation of the interface to compare to the classical thin-film equation.*

$\square$

2.4.3   Waiting time phenomenon

Assume that

$$h_0(s) := \int_{\Omega(s)} u_0^{\alpha-n+2}(x)dx + C_3 T^{\alpha-n+2} \int_{\Omega(s)} S^{\alpha-n+2}(x)dx \leqslant \chi(s - R_0)^{\sigma-4} \qquad (2.58)$$

$\forall s \in [R_0, a], \ R_0 \in (0, b]$, where

$$\chi > 0 \text{ and } \sigma \geqslant 4 + \frac{4(\alpha+2)-3n}{n} = 5 + \frac{4(\alpha-n+2)}{n}.$$

If u_0, $S \in C(\bar{\Omega})$ then (2.58) can be reduced to

$$\min_{x \in \Omega(s)} u_0(x) + C_3 T^{\alpha-n+2} \min_{x \in \Omega(s)} S(x) \leqslant \chi_0(s - R_0)^{\sigma_0} \ \forall s \in [R_0, a], \ \chi_0 > 0, \ \sigma_0 \geqslant \frac{4}{n}. \qquad (2.59)$$

The exact exponent $\frac{4}{n}$ was previously obtained asymptotically for a thin-film equation without a source in [8].

Theorem 4. *Let $1 < n < 2$. Assume that $0 \leqslant u_0 \in H^1(\Omega)$ and $0 \leqslant S(x) \in H^1(\Omega)$ satisfy (2.50), $meas\{\Omega(s) \cap supp \, u_0\} = \varnothing$ and $meas\{\Omega(s) \cap supp \, S(x)\} = \varnothing$ for all $s \in [0, b]$, and the flatness condition (2.58) holds. Then there exists $T^* > 0$, depending on R_0 and χ, such that for the solution u of Theorem 3 holds the following*

$$supp \, u(t, \cdot) \cap \Omega(R_0) = \varnothing \ \forall t \geqslant [0, T^*]. \qquad (2.60)$$

Proof. Choosing in (2.42) the test function ζ (up to some smooth approximation) in the following form:

$$\zeta(x,t) = (s - |x|)_+ = \begin{cases} s - |x| \text{ if } x \in \Omega(s), \\ 0 \text{ if } x \in \Omega \setminus \Omega(s), \end{cases}$$

we arrive at

$$\int_{\Omega(s)} (s-|x|)^4 v^{\frac{2(\alpha-n+2)}{\alpha+2}} \, dx + C_1 \iint_{Q_T(s)} (s-|x|)^4 v_{xx}^2 \, dxdt \leqslant \int_{\Omega(s)} (s-|x|)^4 v_0^{\frac{2(\alpha-n+2)}{\alpha+2}} \, dx +$$

$$C_2 \iint_{Q_T(s)} v^2 \, dxdt + C_3 T^{\alpha-n+2} \int_{\Omega(s)} (s-|x|)^4 S^{\alpha-n+2}(x) dx. \quad (2.61)$$

As $\Omega(s-\delta) \subset \Omega(s)$ then $s - |x| \geqslant \delta \Leftrightarrow |x| \leqslant s - \delta$, and from (2.61) we find that

$$\delta^4 \int_{\Omega(s-\delta)} v^{\frac{2(\alpha-n+2)}{\alpha+2}} \, dx + C_1 \delta^4 \iint_{Q_T(s-\delta)} v_{xx}^2 \, dxdt \leqslant \int_{\Omega(s)} (s-|x|)^4 v_0^{\frac{2(\alpha-n+2)}{\alpha+2}} \, dx +$$

$$C_2 \iint_{Q_T(s)} v^2 \, dxdt + C_3 T^{\alpha-n+2} \int_{\Omega(s)} (s-|x|)^4 S^{\alpha-n+2}(x) dx, \quad (2.62)$$

whence

$$\int_{\Omega(s-\delta)} v^{\frac{2(\alpha-n+2)}{\alpha+2}} \, dx + C_1 \iint_{Q_T(s-\delta)} v_{xx}^2 \, dxdt \leqslant \frac{C}{\delta^4} \left(\int_{\Omega(s)} (s-|x|)^4 v_0^{\frac{2(\alpha-n+2)}{\alpha+2}} \, dx + \right.$$

$$\left. C_3 T^{\alpha-n+2} \int_{\Omega(s)} (s-|x|)^4 S^{\alpha-n+2} dx + \iint_{Q_T(s)} v^2 \, dxdt \right). \quad (2.63)$$

Using (2.63), similar to (2.57) we find that

$$A_T(s-\delta) \leqslant \frac{C_0 T^{1-\theta_1}}{\delta^{4(1+\kappa_1)}} \left(A_T(s) + \int_{\Omega(s)} (s-|x|)^4 v_0^{\frac{2(\alpha-n+2)}{\alpha+2}} \, dx + \right.$$

$$\left. C_3 T^{\alpha-n+2} \int_{\Omega(s)} (s-|x|)^4 S^{\alpha-n+2} dx \right)^{1+\kappa_1} \quad (2.64)$$

for all $s \in [R_0, a]$ and $\delta \in (0, s)$. Using the assumption (2.58), we have

$$\int_{\Omega(s)} (s - |x|)^4 v_0^{\frac{2(\alpha-n+2)}{\alpha+2}} dx + C_3 T^{\alpha-n+2} \int_{\Omega(s)} (s - |x|)^4 S^{\alpha-n+2} dx \leqslant$$

$$(s - R_0)^4 \left[\int_{\Omega(s)} v_0^{\frac{2(\alpha-n+2)}{\alpha+2}} dx + C_3 T^{\alpha-n+2} \int_{\Omega(s)} S^{\alpha-n+2} dx \right] \leqslant \chi (s - R_0)^\sigma$$

for all $s \in [R_0, a]$, where

$$\sigma \geqslant \frac{4(1+\kappa_1)}{\kappa_1} = 4 + \frac{4(\alpha+2)-3n}{n} = 1 + \frac{4(\alpha+2)}{n}.$$

So, we get

$$A_T(s - \delta) \leqslant \frac{C_0 T^{1-\theta_1}}{\delta^{4(1+\kappa_1)}} \left(A_T(s) + \chi(s - R_0)^\sigma \right)^{1+\kappa_1} \tag{2.65}$$

for all $s \in [R_0, a]$. Applying Lemma A.3 to $A_T(s)$ satisfying (2.65), we obtain that $A_T(R_0) = 0$ provided

$$R_0^{4(1+\kappa_1)} \geqslant C_0 T^{1-\theta_1} 2^{\frac{4(1+\kappa_1)^2}{\kappa_1}} (1 + 2^{\frac{4(1+\kappa_1)}{\kappa_1} - \sigma})^{1+\kappa_1} (A_T(a) + \chi(a - R_0)^\sigma)^{\kappa_1}.$$

As

$$A_T(a) \leqslant C_0 T^{1-\theta_1} h_0^{1+\kappa_1}(a) \leqslant C_0 T^{1-\theta_1} \chi^{1+\kappa_1} (a - R_0)^\sigma$$

then

$$R_0^{4(1+\kappa_1)} \geqslant C_0 \chi^{\kappa_1} T^{1-\theta_1} 2^{\frac{4(1+\kappa_1)^2}{\kappa_1}} (1 + 2^{\frac{4(1+\kappa_1)}{\kappa_1} - \sigma})^{1+\kappa_1} (C_0 \chi^{\kappa_1} T^{1-\theta_1} + 1)^{\kappa_1} (a - R_0)^{\sigma\kappa_1}.$$

As a result, $u(x, t) = 0$ for all $(x, t) \in \Omega(R_0) \times [0, T^*]$. $\qquad \square$

Remark 2.4.2. *Note that even though the source term $S(x) > 0$ changes the speed of the support propagation to compare to the classical thin-film equation it does not influence the flatness condition for the waiting time phenomenon to occur.*

2.5   Numerical Simulations

In this section, we present numerical simulations to illustrate some of our main analytical results. All numerical computations below are done using a general PDE module in COMSOL Multiphysics, i.e the finite-element method is used to obtain solutions. To set up the numerical

50

simulations, we take $n = 1.5$ in the thin-film equation with a source:

$$u_t + (u^n u_{xxx})_x = S(x) \tag{2.66}$$

with boundary conditions

$$u_x = u_{xxx} = 0 \text{ on } \partial\Omega \times (0, T) \tag{2.67}$$

on the domain $\Omega = (-L, L)$ with $L = 10$. Numerical time interval is taken as $t \in [0, 2]$. The initial data correspond to a dry wall as $u_0 = 0$ and the source function $S(x)$ is defined as an H^1-smooth approximation of a step function:

$$\tilde{S}(x) = \begin{cases} 1 & \text{if } x \in (-10, -5) \cap (5, 10) \\ 0 & \text{otherwise} \end{cases}.$$
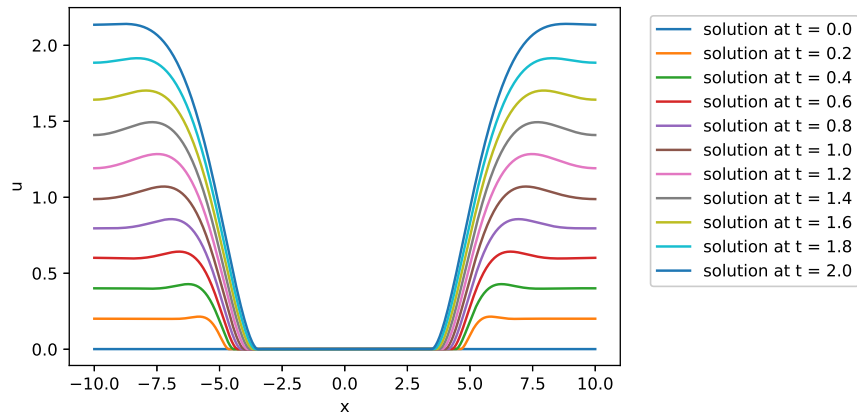
Figure 2.1: Time-evolution of a numerical solution for the equation (2.66) with $u_0 = 0$ and $S(x) = \tilde{S}(x)$.

From our numerical simulations presented in Figure 1 we can roughly estimate how the radius of the support of a numerical solution changes with time (numerical spreading rate) and compare it with $\Gamma(t)$ upper bound that was derived in Theorem 3.
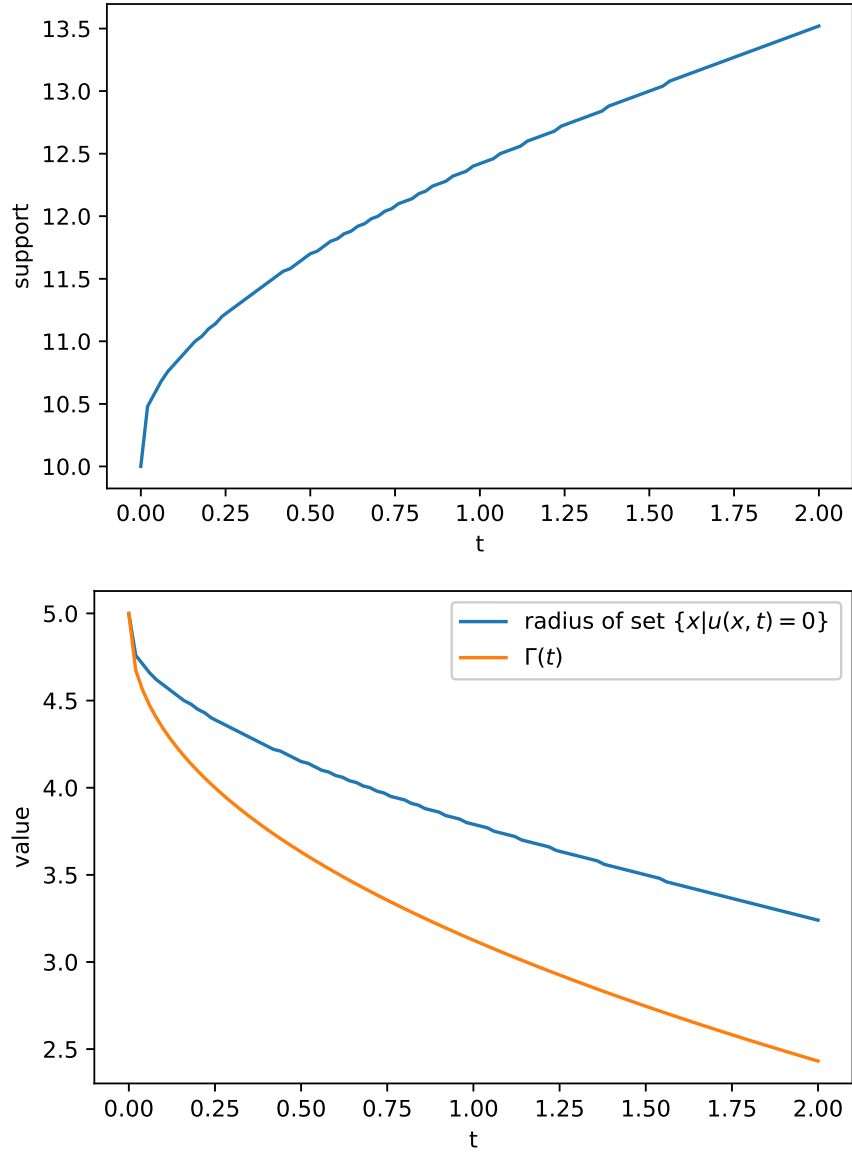
Figure 2.2: Plots of the numerical support propagation versus the upper bound $\Gamma(t)$.

Figure 2 on the top shows the radius of solution's support over time t, in the middle one we plot both the numerical radius of solution's support and $\Gamma(t)$ from the Theorem 3. The graph shows that the size of the numerical support at any time t is bounded by $\Gamma(t)$. Since the derived bound is growing very fast in time it might not be clear that at smaller times the support is bounded by $\Gamma(t)$ as well. The zoomed for smaller times bottom plot provides a better view on the time period near 0. This last plot shows a tighter upper bound as t values are getting closer to 0.

To illustrate another analytical result from Theorem 1 that $\|u - \frac{\mathcal{M}}{|\Omega|} - t\frac{\mathcal{S}}{|\Omega|}\|_{H^1(\Omega)}$ is bounded

by some constant K_0 we should replace the previously chosen initial value $u_0 = 0$, that does not satisfy a sufficient boundness condition from Theorem 1, with $u_0 = 1$ (we use the same source function as above). We also reduce the size of the space domain to $L = 5$, then run simulations until $T = 250$. The source function used in this simulation is

$$\tilde{S}(x) = \begin{cases} 1 & \text{if } x \in (-0.1, 0.1) \\ 0 & \text{otherwise} \end{cases}.$$

Below are time snapshots for the numerical solution. From the numerical time-evolution of the
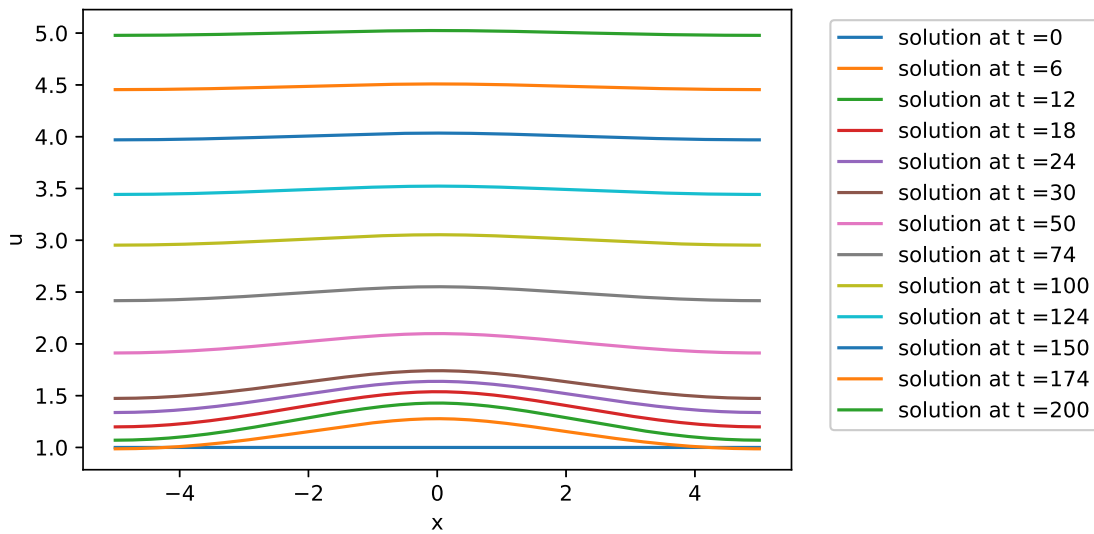
Figure 2.3: Time evolution of the numerical solution for the equation (2.66) with $u_0 = 1$.

solution presented in Figure 3 we can now calculate a numerical approximation for $\|u - \frac{\mathcal{M}}{|\Omega|} - t\frac{\mathcal{S}}{|\Omega|}\|_{H^1(\Omega)}$ at each time step. Below is the graph obtained.

Figure 4 shows the plot of $\|u - \frac{\mathcal{M}}{|\Omega|} - t\frac{\mathcal{S}}{|\Omega|}\|_{H^1(\Omega)}$ and provides a numerical evidence that the bound K_0 does exist. From this plot we can clearly see a constant bound $K_0 = 4.0$ since the value of the norm reaches its maximum around $t = 15$.

Now we would like to illustrate a convergence result given in Theorem 2, i.e we want to show that the solution in long run converges to $\frac{\mathcal{M}}{|\Omega|} + tS_0$. We use $S_0 = 1$ with $u_0 = 1 + \cos(\frac{4\pi x}{L})$ for these numerical simulations. Figure 5 below presents time snapshots of the numerical solution. Using the numerical results presented in Figure 5 we can calculate $\|u - \frac{\mathcal{M}}{|\Omega|} - tS_0\|_{H^1(\Omega)}$. Figure 6 shows the numerical convergence as $t \to \infty$.
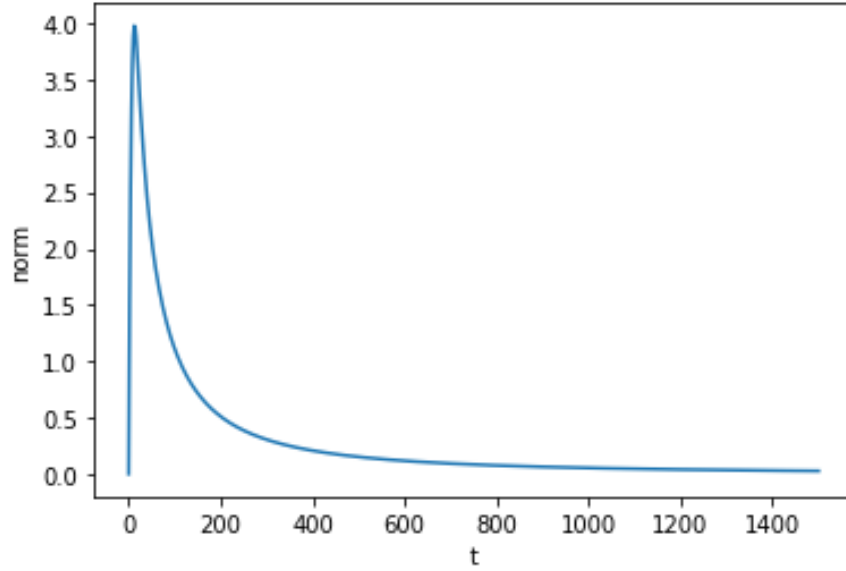
Figure 2.4: Plot of $\|u - \frac{\mathcal{M}}{|\Omega|} - t\frac{\mathcal{S}}{|\Omega|}\|_{H^1(\Omega)}$ over time t
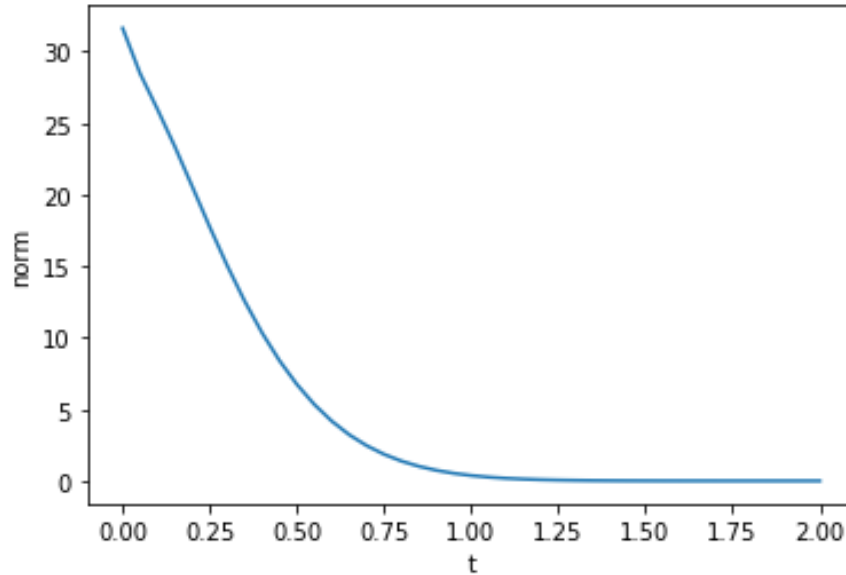
Figure 2.6: Plot of $\|u - \frac{\mathcal{M}}{|\Omega|} - tS_0\|_{H^1(\Omega)}$ versus time t.

We did not explore all possible ranges of the non-linearity exponent n but we believe that our analytical and numerical finite speed propagation results could be extended to $2 < n < 3$. Some interesting future research can also be done by removing the positivity restriction on the source term $S(x)$. For the opposite sign-definite case $S(x) < 0$ (sink term) one can study a shrinkage of the interface and the most complicated case to consider would be a sign indefinite $S(x)$.
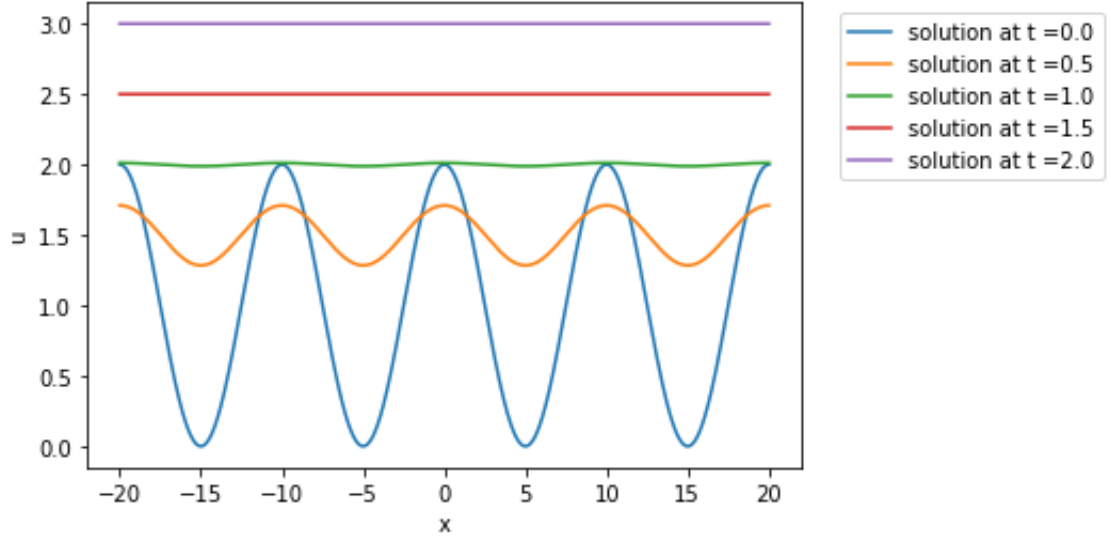
Figure 2.5: Time snapshots of the numerical solution for the equation (2.66) with $u_0 = 1 + \cos(\frac{4\pi x}{L})$ and $S_0 = 1$.

2.6 Appendix

Here we list several theorems and lemmas used in this chapter. The proof can be found in several sources.

1. Stampacchia's lemma: Let $f \geq 0$ be nonincreasing in $[\bar{x}, \infty)$. Assume f satisfies, for some $C > 0, p > 0, \gamma > 1$:

$$(y - x)^p f(y) \leq Cf(x)^\gamma, \text{ for } y \geq x \geq \bar{x}$$

Then $f(y) = 0$ for $y \geq \bar{x} + d$, where: $d^p = Cf(0)^{\gamma-1} 2^{\frac{p\gamma}{\gamma-1}}$

Proof. We may assume $\bar{x} = 0$. Letting $g = (f/f(0))^{1/p}$ and $A = (Cf(0)^{\gamma-1})^{1/p}$ we find:

$$(y - x)g(y) \leq Ag(x)^\gamma \text{ for } y > x, g(0) = 1$$

Fix $y > 0$, and let $x_n = y\left(1 - \frac{1}{2^n}\right), n \geq 0$, so $x_n \uparrow y$. Then $g(x_0) = 1$ and:

$$g(x_{n+1}) \leq \frac{A}{y} 2^{n+1} g(x_n)^\gamma$$

Inductively we find, for $n \geq 1$:

$$g(x_n) \leq \left(\frac{A}{y}\right)^{1+\gamma+\dots+\gamma^{n-1}} 2^{S_n}, \quad S_n = n + (n-1)\gamma + \dots + \gamma^{n-1}$$

It is an exercise to compute the sum:

$$S_n = \sum_{j=0}^{n-1}(n-j)\gamma^j = \frac{\gamma^{n+1} + n - (n+1)\gamma}{(\gamma-1)^2}, n \geq 1$$

Suppose $\frac{y}{A} = 2^{\frac{\beta}{\gamma-1}}$. Then:

$$\left(\frac{A}{y}\right)^{\frac{\gamma^n-1}{\gamma-1}} = 2^{-\beta\frac{\gamma^n-1}{(\gamma-1)^2}}$$

while:

$$\gamma^{n+1} + n - (n+1)\gamma - \beta(\gamma^n - 1) = (\gamma^n - 1)(\gamma - \beta) - n(\gamma - 1)$$

This means that if we choose $\beta = \gamma$, we have, for the choice $y = d = 2^{\frac{\gamma}{\gamma-1}}A$

$$0 \leq g(d) \leq g(x_n) \leq 2^{-\frac{n}{\gamma-1}}, \quad n \geq 1$$

Letting $n \to \infty$, we see $g(d) = 0$, hence $f(d) = 0$, where $d^p = Cf(0)^{\gamma-1}2^{\frac{p\gamma}{\gamma-1}}$

2. Minkowski inequality: Assume $1 \leq p \leq \infty$, and $u, v \in L_p(U)$. Then

$$\|u+v\|_{L_p} \leq \|u\|_{L_p} + \|v\|_{L_p}$$

Proof:

First we show that $u + v \in L_p$,

$$\int(u+v)^p dx \leq \int(|u|+|v|)^p dx \leq \int \frac{1}{2}(2|u|)^p + \frac{1}{2}(2|v|)^p dx = 2^{p-1}\int(|u|^p + |v|^p)dx \leq \infty$$

$$\|u+v\|_{L_p}^p = \int (u+v)^p dx \le \int (u+v)^{p-1}(|u|+|v|)dx$$

$$\le \left(\int (u+v)^p dx\right)^{\frac{p-1}{p}} \left(\left(\int |u|^p dx\right)^{\frac{1}{p}} + \left(\int |v|^p dx\right)^{\frac{1}{p}}\right)$$

$$= \|u+v\|_{L_p}^{p-1} \left(\|u\|_{L_p} + \|v\|_{L_p}\right)$$

Rearrange we have

$$\|u+v\|_{L_p} \le \|u\|_{L_p} + \|v\|_{L_p}$$

Chapter 3

Dynamics of liquid films falling down a vertical fiber

3.1 Introduction

Thin viscous liquid flows along vertical cylindrical fibers exhibit complex and unstable interfacial dynamics with distinct regimes. Driven by the effects of Rayleigh-Plateau instability and gravity, a wide range of dynamics can be observed experimentally. These include the formation of discontinuous bead-like droplets, travelling wave-like patterns, and irregularly coalescing droplets. The study of these dynamics has widespread applications in heat and mass exchangers, desalination [55], and particle capturing systems [54], attracting much attention over the past two decades.

Depending on flow rate, liquid choice, fiber radius, and inlet geometry, three typical flow regimes have been observed [36, 35]: (a) the convective instability regime, where bead coalescence happens repeatedly; (b) the traveling wave regime, where a steady train of beads flow down the fiber at a constant speed; and (c) the isolated droplet regime, where widely spaced large droplets are separated by small wave patterns. If other system parameters are fixed, and flow rate is varied from high to low, this can lead to flow regime transition from (a) to (b), and eventually to (c). Further analysis of the travelling wave patterns in regime (b) is expected to provide insights into many engineering applications that utilize steady trains of beads.

For small flow rates, classical lubrication theory is typically used to model the dynamics of

axisymmetric flow on a cylinder. When the fluid film thickness is significantly smaller than the cylinder radius, Frenkel [28] proposed a weakly nonlinear thin-film equation to calculate the evolution of film thickness h (or the height of the film) and capture both stabilizing and destabilizing effects of the surface tension in the dynamics. This evolution equation was further studied by Kalliadasis & Chang [36], Chang & Demekhin [15], and Marzuola, Swygert & Taranets [41]. Craster & Matar [20] developed an asymptotic model which relaxes the thin film assumption, instead requiring that the film thickness be smaller than the capillary length. In 2000, Kliakhandler [37] extended the thin film model to consider thick layers of viscous fluid by introducing fully nonlinear curvature terms, leading to the following evolution equation for the film thickness $h(x, t)$:

$$h_t + \frac{1}{h+r_0}\left[\sigma^{-1}Q(h)\left(\frac{h_{xx}}{(1+h_x^2)^{3/2}} - \frac{1}{(h+r_0)(1+h_x^2)^{1/2}}\right)_x + Q(h)\right]_x = 0, \tag{3.1}$$

where $\sigma > 0$ is the Bond number (ratio of surface tension to gravity forces), $r_0 > 0$ is the dimensionless fiber radius, and the flow rate $Q(h)$ takes the form

$$Q(h) = \frac{1}{16}\left[4(h+r_0)^4\log\left(\frac{h+r_0}{r_0}\right) - h(3h^3 + 12r_0h^2 + 14r_0^2h + 4r_0^3)\right]. \tag{3.2}$$

The last $Q(h)$ term in (3.1) corresponds to the draining flow due to gravity, while the terms $\frac{h_{xx}}{(1+h_x^2)^{3/2}}$ and $\frac{1}{(h+r_0)(1+h_x^2)^{1/2}}$ describe the stabilizing and destabilizing roles of the surface tension due to axial and azimuthal curvatures of the interface, respectively.

Recently in 2019, Ji et al. [34] investigated a family of full lubrication models that incorporate slip boundary conditions, fully nonlinear curvature terms, and a film stabilization mechanism. The film stabilization term,

$$\Pi(h) = -\frac{A}{h^3}, \quad A > 0, \tag{3.3}$$

is motivated by the form of disjoining pressure widely used in lubrication equations [50] to describe the wetting behavior of a liquid on a solid substrate, and the scaling parameter $A > 0$ is typically selected based on a stable liquid layer in the coating film dynamics. Numerical investigations of experimental results in [34] showed that compared to previous studies, the combined physical effects better describe the propagation speed and the stability transition of the moving droplets. For higher flow rates, coupled evolution equations of both the film thickness and local

flow rate are developed [53, 52, 65]. These equations incorporate inertia effects and streamwise viscous diffusion based on the integral boundary-layer approach. Recently, Ji et al. [35] further extended a weighted-residual integral boundary-layer model to incorporate the film stabilization mechanism to address the effects of the inlet nozzle geometry on the downstream flow dynamics.

In this work we derive a new model that can simulate many of the experimentally observed regimes based only on an assumption of a plug flow velocity profile, which corresponds to high Reynolds number turbulent flows in which due to lateral mixing, the velocity profile approaches a uniform state. A thin boundary layer on the fiber surface imparts the viscous drag upon the liquid film. We analyze linear and nonlinear stability of an initially uniform film on the fiber and use scientific computing and simulations to study their long-term dynamics.

3.2 Model Derivation via Control Volume Analysis

In this section we derive our model for an axisymmetric liquid film flowing down an infinitely long cylindrical fiber. The primary difference between the current model and earlier ones is that we assume the velocity profile within the film represents a plug flow, being uniform within the film cross section. Still, we account for a drag force exerted between the solid surface of the fiber and the flowing film, proportional to the flow velocity, with a constant coefficient. Such a model should be more appropriate for rapid, potentially turbulent flow at high Reynolds numbers, in contrast to the case of highly viscous thin liquid films whose velocity profile is far from uniform and which flow much more slowly. Before deriving the model, it helps to compare and contrast these two cases in more detail, in the simpler situation when the flows are fully developed.

3.2.1 Fully-Developed Flow

Plug Flow

This case is simple to analyze. Consider a cylindrical fiber of radius R and a liquid film whose interface is at distance H from the fiber axis, resulting in a liquid film of thickness $H - R$. Suppose that the fluid is falling down the fiber under the influence of gravity at uniform speed U. At steady state (terminal draining velocity), the weight of any portion of the liquid between two

axial locations is balanced by the drag force exerted by the solid surface of the fiber on the liquid. The weight of the liquid between two axial locations x_1 and x_2, with $\Delta x = x_2 - x_1$, is given by $\rho g \pi (H^2 - R^2) \Delta x$. If the shear stress at the fiber surface is denoted by τ_{rx}, the drag force exerted on that portion of liquid would be $2\pi R \tau_{rx} \Delta x$. From a dimensional reasoning, the form of the shear stress could be assumed to be

$$\tau_{rx} = \frac{\mu U}{\ell},$$

in which parameter ℓ is some quantity with units of length. It could be thought of as some measure of an extremely thin boundary layer thickness that might be separating the plug flow region with velocity U from the fiber surface on which a no-slip boundary condition would exist. Of course, we ignore the boundary layer region when assuming plug flow, but still account for the drag force that the fiber exerts on the liquid. By balancing the weight of the liquid with the drag force, we can obtain a relationship between the flow speed U and the film thickness H. The result is

$$U = \frac{\rho g R \ell}{2\mu} (h^2 - 1),$$

in which $h = H/R$ is the ratio of liquid film radius to the fiber radius. If we assume parameter ℓ to be constant, the velocity scale can be chosen to be $U_o = \rho g R \ell / 2\mu$ and the dimensionless draining velocity $u = U/U_o$ would be given by $u = f(h) = h^2 - 1$. We will compare this quadratic expression for the draining velocity as a function of h with the result for fully developed viscous flow obtained below. We will find that this function $f(h)$ increases much more rapidly with h as compared to the situation with viscous laminar flow.

Viscous Laminar Flow

For the case of fully-developed laminar flow down the fiber, the velocity profile $u(r)$ can be obtained by integrating the axial component of the Navier-Stokes equation which reads

$$\frac{\mu}{r} \frac{d}{dr} \left(r \frac{du}{dr} \right) + \rho g = 0.$$

The boundary conditions are that $u(R) = 0$ (no slip on the fiber surface) and $u'(H) = 0$ (zero shear stress at the free surface). The resulting velocity profile is given by

$$u(r) = \frac{\rho g R^2}{4\mu} \left[1 - (\frac{r}{R})^2 + 2(\frac{H}{R})^2 \ln(\frac{r}{R}) \right] .$$

The mean velocity U can be calculated using the definition

$$U = \frac{\int_R^H r u(r) dr}{\int_R^H r dr}$$

resulting in

$$U = \frac{2\rho g R^2}{\mu} \frac{I(h)}{(h^2 - 1)}$$

with $h = H/R$ and

$$I(h) = \frac{1}{16} \left(4h^4 \ln(h) - 3h^4 + 4h^2 - 1 \right) .$$

The shear stress on the fiber surface $\tau_{rx} = \mu u'(R)$ can be expressed as before in the form

$$\tau_{rx} = \frac{\mu U}{\ell(h)}$$

but with length parameter ℓ now depending on h and given by

$$\frac{\ell(h)}{R} = \frac{4I(h)}{(h^2 - 1)^2} .$$

As such, the main difference between the plug flow model and the viscous laminar flow one is that in the former, ℓ is treated as a constant, whereas in the latter, it depends on the film thickness. With the proportionality constant between the shear stress and the mean velocity being dependent on h, the functional form of the dependence of the mean draining velocity versus film thickness is quite different. In particular, the dimensionless mean velocity, now scaled with velocity scale $U_1 = 2\rho g R^2/\mu$, would be given by

$$u(h) = \frac{U}{U_1} = \frac{I(h)}{h^2 - 1} = f_1(h) ,$$
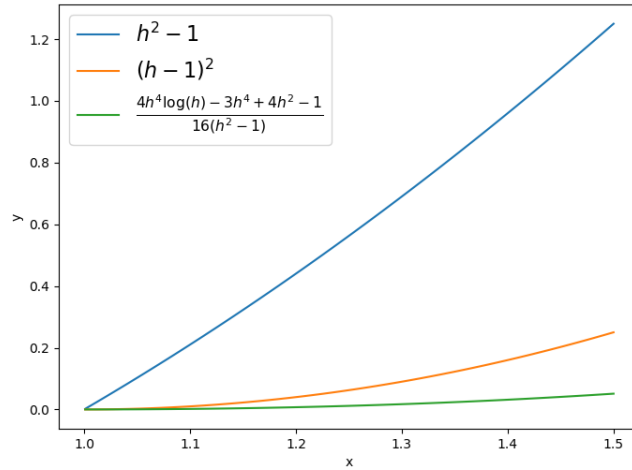
Figure 3.1: Flux function comparison

which can be compared to the result for plug flow, which was $u(h) = f(h) = h^2 - 1$. Figure 3.1 shows simultaneous plots of the two functions $f(h)$ and $f_1(h)$ for h ranging from 1 (which corresponds to a film thickness of zero) to 1.5. As apparent in the figure, for the plug flow case, the mean velocity increases with film thickness much more than it would in the case of viscous laminar flow. This difference makes a large difference in the behavior of the falling film when it is not fully developed and uniform.

3.2.2 Control Volume Analysis

In order to derive the equations of motion for a falling film in which the film thickness varies with axial distance and time, i.e., $H = H(x, t)$, we use a control volume approach as depicted in Figure 3.2. We assume the velocity in the film to remain as plug flow, but allow the latter to vary with axial location and time as well: $U = U(x, t)$. We consider a control volume consisting of the portion of the fluid between two axial locations x and $x + \Delta x$, as shown in the figure. Denote the cross-sectional area of the fluid at any axial position and time x by $A(x, t) = \pi(H^2(x, t) - R^2)$.

The integral form of the conservation of mass in the region between x and $x + \Delta x$ reads

$$\frac{d}{dt} \int_x^{x+\Delta x} \rho A(x, t) dx = \rho A U|_x - \rho A U|_{x+\Delta x},$$

63
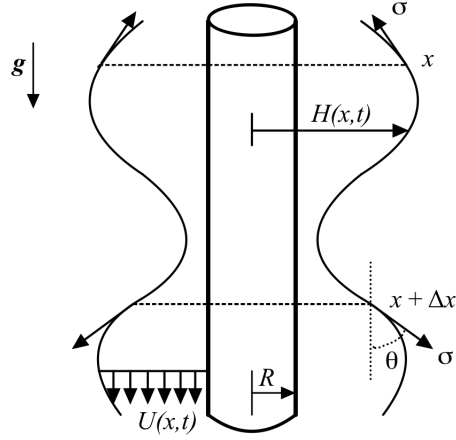
Figure 3.2: Schematic plot of the film on fiber

equating the rate of change of mass to the rate at which mass enters the control volume at position x minus the rate at which it leaves at position $x + \Delta x$. The left-hand side of this equation can be written as

$$\int_x^{x+\Delta x} \rho \frac{\partial A}{\partial t}(x,t)dx = \rho \frac{\partial A}{\partial t}(\xi,t)\Delta x\,,$$

where ξ is somewhere in the interval $[x, x + \Delta x]$. Dividing both sides of the equation by Δx and taking the limit $\Delta x \to 0$ results in the equation

$$\frac{\partial A}{\partial t} + \frac{\partial(UA)}{\partial x} = 0\,,$$

for conservation of volume as expected. Since $A(x,t) = \pi(H^2(x,t) - R^2)$, we can rewrite this equation as

$$2H\frac{\partial H}{\partial t} + \frac{\partial(U(H^2 - R^2))}{\partial x} = 0\,.$$

Moving on to the conservation of linear momentum equation in the axial direction, one can similarly equate the rate of change of total linear momentum in the control volume to the net rate at which momentum flows into the control volume plus the sum of the forces in the axial direction

64

acting on the fluid in that volume. This equation takes the form

$$\rho \Delta x \frac{\partial}{\partial t}(AU)|_{\xi} = \rho(AU^2)|_x - \rho(AU^2)|_{x+\Delta x} + \rho g \Delta x A|_{\xi'}$$

$$+ (pA)|_x - (pA)|_{x+\Delta x} + (A\tau_{xx})|_{x+\Delta x} - (A\tau_{xx})|_x$$

$$- 2\pi R \Delta x\, \tau_{rx}|_{\xi''} + 2\pi\sigma(H\cos(\theta))|_{x+\Delta x} - 2\pi\sigma(H\cos(\theta))|_x\,.$$

The terms on the right-hand side of this equation have the following physical interpretations: The first two terms provide the net rate at which momentum enters the control volume across the two boundaries, the next term is the weight of the volume of fluid in the control volume, the next two capture the contribution from the pressure force acting on the two cross-sections, followed by the two terms that account for any viscous normal stress at those same cross-sections, the next term is the drag force exerted on the fluid by the solid surface of the fiber, and finally, the last two terms capture the effect of surface tension acting on the perimeter of the free surface (since surface tension is tangent to the interface, to project it onto the axial direction, we need the cosine of the angle that the tangent vector makes with the axial direction in those terms). Upon dividing this equation by Δx and taking the limit $\Delta x \to 0$, we get the differential equation

$$\rho \frac{\partial(AU)}{\partial t} + \rho \frac{\partial(AU^2)}{\partial x} = \rho g A - \frac{\partial(pA)}{\partial x} + \frac{\partial(\tau_{xx}A)}{\partial x} - 2\pi R\tau_{rx} + 2\pi\sigma \frac{\partial(H\cos\theta)}{\partial x}\,.$$

Using the conservation of volume equation, the left-hand side of the last equation can be simplified to $\rho A(\partial U/\partial t + U\partial U/\partial x)$. Also, we substitute $\mu U/\ell$ for the shear stress τ_{rx} and $2\mu\partial U/\partial x$ for the normal viscous stress τ_{xx}. Upon dividing the entire equation by the cross-sectional area $A(x,t)$ we thus obtain

$$\rho\left(\frac{\partial U}{\partial t} + U\frac{\partial U}{\partial x}\right) + \frac{1}{A}\frac{\partial(pA)}{\partial x} = \rho g + \frac{2\mu}{A}\frac{\partial}{\partial x}\left(A\frac{\partial U}{\partial x}\right) - \frac{2\pi\mu RU}{\ell A} + \frac{2\pi\sigma}{A}\frac{\partial(H\cos\theta)}{\partial x}\,.$$

In this equation, the cross-sectional area is given by $A(x,t) = \pi(H^2(x,t) - R^2)$, and since $\tan(\theta) = \partial H/\partial x$ (the slope of the free surface), the cosine of that angle is given by $\cos(\theta) = 1/\sqrt{1 + H_x^2}$ in which subscript refers to a partial derivative. The pressure within the film, $p(x,t)$, is taken to be uniform in the cross section and related by the Young-Lapalce equation to the curvature of the free

surface, namely $p(x,t) = \sigma\kappa(x,t)$, in which σ is the surface tension and the curvature κ is given by

$$\kappa(x,t) = \frac{(1 + H_x^2 - HH_{xx})}{H(1 + H_x^2)^{3/2}},$$

with subscripts referring to partial derivatives. Note that ordinarily the pressure in the fluid would be written as $p = p_o + \sigma\kappa$ in which p_o is the constant pressure in the air outside the interface. However, in calculating the force on the control volume, the contribution of the force due to p_o acting all around the control volume (including on the curved free surface) integrates to zero, so that constant part of the pressure is omitted.

The pressure term in the momentum equation can be written as a sum of two terms:

$$\frac{1}{A}\frac{\partial(pA)}{\partial x} = \frac{\partial p}{\partial x} + \sigma\kappa\frac{1}{A}\frac{\partial A}{\partial x}.$$

Interestingly, the second term on the right-hand side is exactly equal to the surface tension term on the right-hand side of the momentum equation, namely the term

$$\frac{2\pi\sigma}{A}\frac{\partial(H\cos\theta)}{\partial x},$$

so those two terms cancel each other leaving simply $\partial p/\partial x$ on the left-hand side of the momentum equation. The above cancellation is a consequence of a relationship that appears to be purely geometrical, involving the curvature κ and the rates of change of area and the perimeter multiplied by the cosine factor, namely: $\kappa\partial A/\partial x = 2\pi\partial(H/\sqrt{1+H_x^2})/\partial x$ in which $\cos\theta = (1 + H_x^2)^{-1/2}$. After this simplification, the momentum equation further divided by density ρ becomes

$$\frac{\partial U}{\partial t} + \frac{\partial}{\partial x}\left(\frac{1}{2}U^2 + \sigma\kappa\right) = g - \frac{2\pi\nu RU}{\ell A} + \frac{2\nu}{A}\frac{\partial}{\partial x}\left(A\frac{\partial U}{\partial x}\right).$$

Here $\nu = \mu/\rho$ is the kinematic viscosity of the fluid. Since $A = \pi(H^2 - R^2) = \pi R^2(h^2 - 1) = \pi R^2 f(h)$, upon choosing the velocity scale $U_o = gR\ell/2\nu$ and defining the dimensionless velocity $u = U/U_0$, and upon scaling time with U_o/g, i.e., with $\hat{t} = gt/U_o$, the first term on the left-hand side and the first two terms on the right-hand side would yield a dimensionless equation of the

66

form

$$\frac{\partial u}{\partial \hat{t}} = 1 - \frac{u}{f(h)} .$$

Such an equation would hold if all x-derivatives were absent. It would suggest that for a given dimensionless film thickness h, the velocity of the film would relax exponentially in time to its terminal velocity $f(h) = h^2 - 1$ with a relaxation time of order one in terms of the dimensionless time $\hat{t}$.

Carrying the scaling further by nondimensionalizing the axial distance x and curvature κ with the fiber radius R so that $\hat{x} = x/R$ and $\hat{\kappa} = R\kappa$, we obtain the fully nondimensional form of the axial momentum equation which, upon dropping the hats for clarity, reads

$$u_t + (au^2/2 + b\kappa)_x = [1 - u/f(h)] + c(h^2 - 1)^{-1}[(h^2 - 1)u_x]_x ,$$

in which subscripts represent partial derivatives. The dimensionless curvature appearing in this equation is given by

$$\kappa = \frac{(1 + h_x^2 - hh_{xx})}{h(1 + h_x^2)^{3/2}} .$$

Three dimensionless parameters, called a, b and c, also appear in this equation, given respectively by:

$$a = \frac{U_o^2}{Rg} , \qquad b = \frac{\sigma_o}{\rho R^2 g} , \qquad c = \frac{2\nu U_o}{R^2 g} .$$

Using the definition of velocity scale U_o, parameters a and c can also be expressed as

$$a = \frac{gR\ell^2}{4\nu^2} , \qquad c = \frac{\ell}{R} .$$

In its original form, parameter a is seen to be the square of the Froude number and parameter b is the reciprocal of the Bond or Eotvos number. Parameter c is the ratio of the characteristic boundary layer thickness to the fiber radius.

Using the same scaling, the dimensionless form of the conservation of volume equation takes the form:

$$2hh_t + a[u(h^2 - 1)]_x = 0 .$$

To sum up, we have the system of PDE with respect to $u(x,t)$ and $h(x,t)$

$$\begin{cases} u_t + (au^2/2 + b\kappa)_x = [1 - u/f(h)] + c(h^2-1)^{-1}[(h^2-1)u_x]_x \\ 2hh_t + a[u(h^2-1)]_x = 0 \end{cases} \tag{3.4}$$

where

$$\kappa = \frac{(1+h_x^2 - hh_{xx})}{h(1+h_x^2)^{3/2}}, \quad f(h) = h^2 - 1, \quad a,b,c > 0$$

for $x \in \Omega = [0,L]$ and $t \in [0,T]$ with a periodic boundary condition. Parameter a,b,c is the coefficients of the inertia, surface tension and viscous drag terms correspondingly.

3.3 Linear Stability Analysis

In this section, we conduct a linear stability analysis about constant solutions of the system in 3.4. Note that any constant h_0 and u_0 that satisfy $u_0 = f(h_0)$ is a solution of the system. We define the perturbed solution in the form below,

$$h(x,t) = h_0 + \epsilon h_1(x,t) + O(\epsilon^2) \tag{3.5}$$

$$u(x,t) = u_0 + \epsilon u_1(x,t) + O(\epsilon^2) \tag{3.6}$$

and h_0 and u_0 are constants satisfying $u_0 = f(h_0)$. Small parameter ϵ is introduced for bookkeeping purposes. We derive a linearized system for the leading perturbations as

$$\frac{\partial u_1}{\partial t} + \frac{\partial}{\partial x}[au_0 u_1 - b(\frac{h_1}{h_0^2} + \frac{\partial^2 h_1}{\partial x^2})] = (\frac{h_1 f'(h_0)}{f(h_0)} - \frac{u_1}{f(h_0)}) + c\frac{\partial^2 u_1}{\partial x^2}$$

$$\frac{\partial h_1}{\partial t} + \frac{\partial}{\partial x}[u_0 h_1 + \frac{1}{2}u_1(h_0 - \frac{1}{h_0})] = 0$$

Using the following form of h_1, u_1 defined,

$$h_1 = \Re\{He^{ikx+\sigma t}\} \tag{3.7}$$

$$u_1 = \Re\{Ue^{ikx+\sigma t}\} \tag{3.8}$$

68
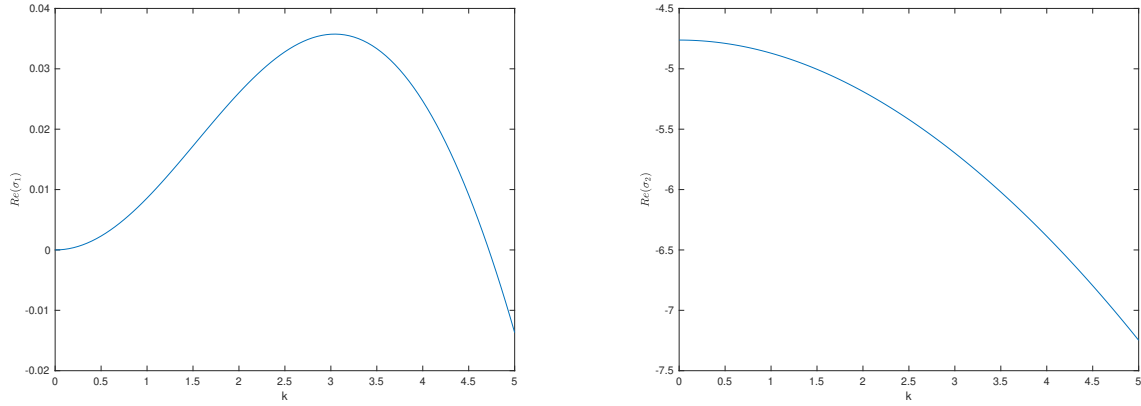
Figure 3.3: Plots of $Re(\sigma_1)$ and $Re(\sigma_2)$ against the wave number k under the constant solution $h_0 = 1.1, u_0 = f(h_0)$ with parameter $a = 1, b = 0.01, c = 0.1$. while $Re(\sigma_2)$ stays negative for all k, σ_1 has a positive real part for small k.

we obtain the linear system

$$
\begin{bmatrix}
i(2aku_0) + 2\sigma & ika(h_0 - \frac{1}{h_0}) \\
i(-\frac{kb}{h_0^2} + bk^3) - \frac{f'(h_0)}{f(h_0)} & i(aku_0) + \sigma + ck^2 + \frac{1}{f(h_0)}
\end{bmatrix}
\begin{bmatrix}
H \\
U
\end{bmatrix} = 0
$$

To have a non-trivial solution of the system for H and U, the determinant of the coefficient matrix needs to be zero. This provides a quadratic equation for the growth rate σ, and we can solve for σ given k, h_0, u_0. Figure 3.3 shows the relationship between wave number k and the real part of σ. If that real part is positive, those particular waves grow and the system is unstable. In the figure, σ_1, σ_2 represent the two roots that are obtained numerically. The results show that constant solutions are unstable to long waves or small wavenumbers.

The stability result can be checked against simulations. We did a comparison between two simulations, one using the full nonlinear model and the other being the linearized one to see the effects of nonlinearity on the film thickness evolution. In the simulation, we have $h_0 = 1.1 + 0.001\sin(kx)$ and the domain is set as $L = \frac{2\pi}{k}$. Here we set $k = 3.05$, the most unstable wavenumber for $h_0 = 1.1$. The results show the rate of increase of the maximum film height is slower in the original nonlinear models as compared with the linearized model. From figure 3.4b we see that after we take the logarithm of the maximum film thickness over domain, the linear model follows an exponential

69
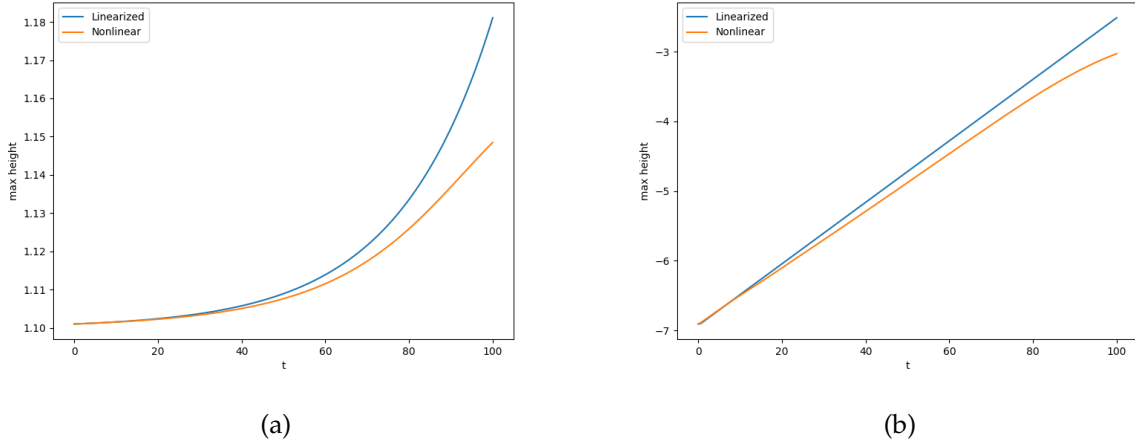
Figure 3.4: Plots of $\max_{x \in \Omega}(h(x,t))$ and $\log(\max_{x \in \Omega}(h(x,t)))$ over time.

growth rate while the nonlinear model slowly deviate from the exponential growth at later times.

The linearized model follows an exponential growth rate, we estimate the slope for $\log(h - h_0)$ as the growth rate. The estimated growth rate is $\sigma \approx 0.044$.

3.4 Short-time and Long-time Dynamics

In this section, we discuss about the long-time dynamics of the system of equations. The simulation displayed in this part is done in the domain $\Omega = [0, 5]$. The initial value is set as a perturbation consisting of multiple sine waves: here we use $h(x, 0) = 1.1 + \epsilon \sum_{n=1}^{3} \sin(\frac{2n\pi x}{5})$. We separate the simulation into two phases. The early phase from $t = 0$ to around $t = 500$ shows an instability developing at the beginning and forming two major waves with different heights, and we can see the maximum wave height of the two increasing over time and then dropping back to some fix height. For t larger than 1000, we can see that the solution reaches a steady state which contains two equal height traveling wave, and the maximum height is not changing over time. A snapshot of solutions at the early phase and the steady phase is displayed in Figure 3.7. The maximum height of fluid over time could better illustrate the dynamics of the two phases and the transition between them, we display the result in Figure 3.8.

To see how our model with plug flow differs from the laminar viscous case, We change the expression for the flux function from $f(h) = h^2 - 1$ to $f(h) = (h - 1)^2$, which more closely approximates the laminar flow profile. In the future, an interpolation between these two functions

70
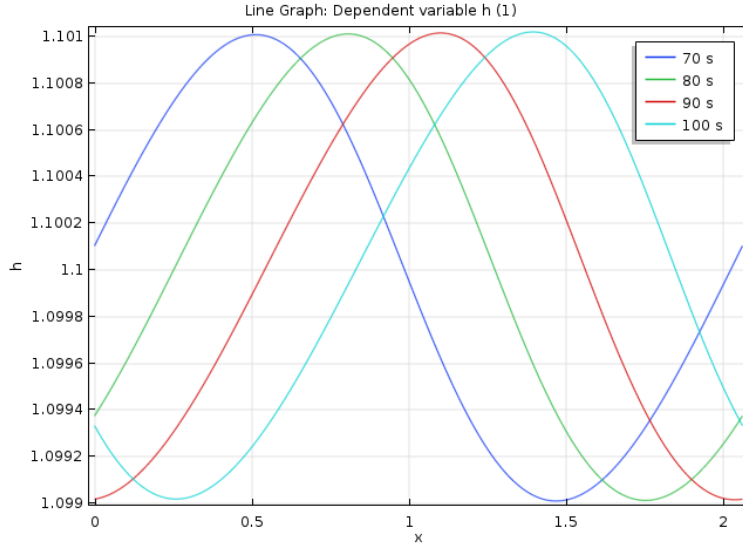
Figure 3.5: Film thickness $h(x,t)$ for model with $f(h) = (h-1)^2$ at various time step t.

for small and large h might capture the transition between the two regimes better. This new flux function leads to different dynamics as those two functions behave differently when h is close to 1. A comparison for those two functions near point $h = 1$ is shown in Figure 3.1

The simulation of the model using $f(h) = (h-1)^2$ is displayed in Figure 3.5. We can see the growth of wave height is almost unnoticeable compare to the $f(h) = h^2 - 1$ case. The stability analysis shows a long wave instability like before but with a very small real part with magnitude close to 10^{-6}, indicating a much slower growth rate. The stability analysis result is visualized in Figure 3.6

3.5 Additional Simulations

In this section, we include several additional simulations carried out for the full model and the linearized model with different parameters. First we plot the simulation results for the linearized model and compared the maximum film height over time with the nonlinear model to see the effect of the nonlinear terms.

Figures 3.9 and 3.10 show the simulation for $h_0 = 1.1 + 0.001 \sin(kx)$ with $k = 3.05$ for the system of equation and the linearized around $h_0 = 1.1$ model.

We also show a simulation with an initial condition which is a Gaussian shape located at $x = 1$

71
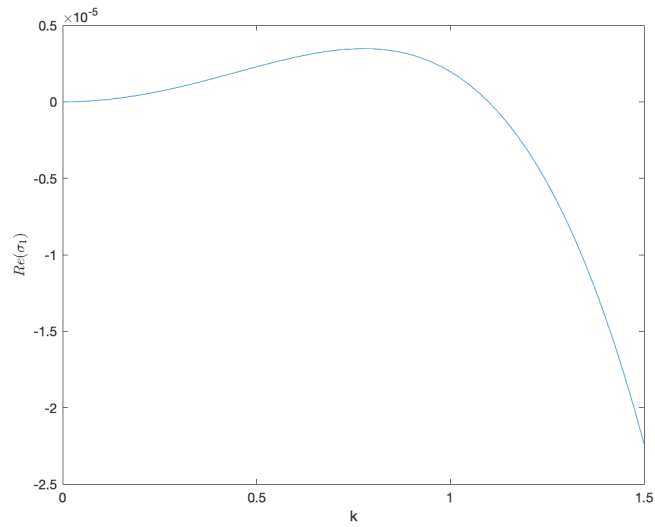
Figure 3.6: Plots of $Re(\sigma_1)$ against the wave number k under the constant solution $h_0 = 1.1, u_0 = f(h_0)$ with parameter $a = 1, b = 0.01, c = 0.1$ and $f(h) = (h-1)^2$.
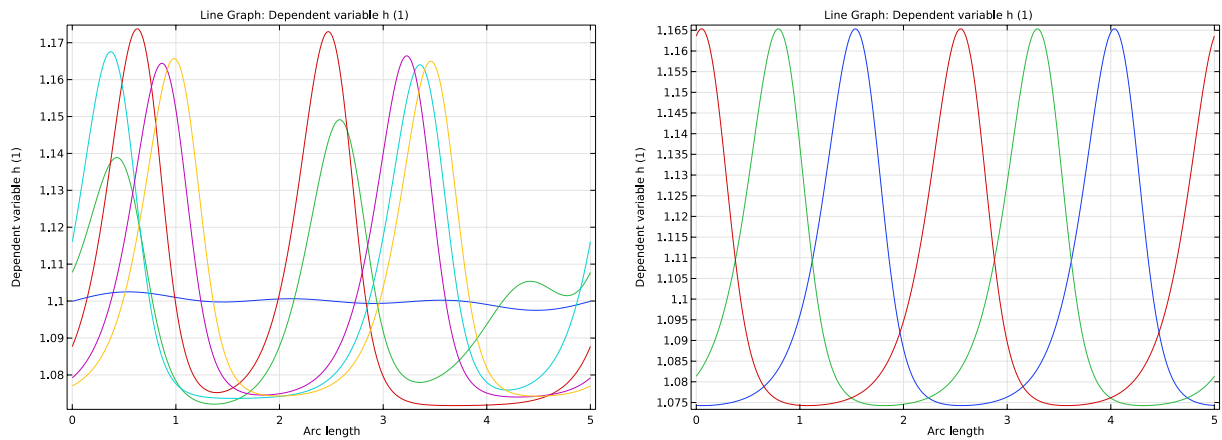
Figure 3.7: Left Plot shows the film thickness $h(x,t)$ over domain x at $t = 0, 100, \cdots, 500$ and the right plot shows the long time dynamics of the solution at $t = 8000, 9000, 10000$
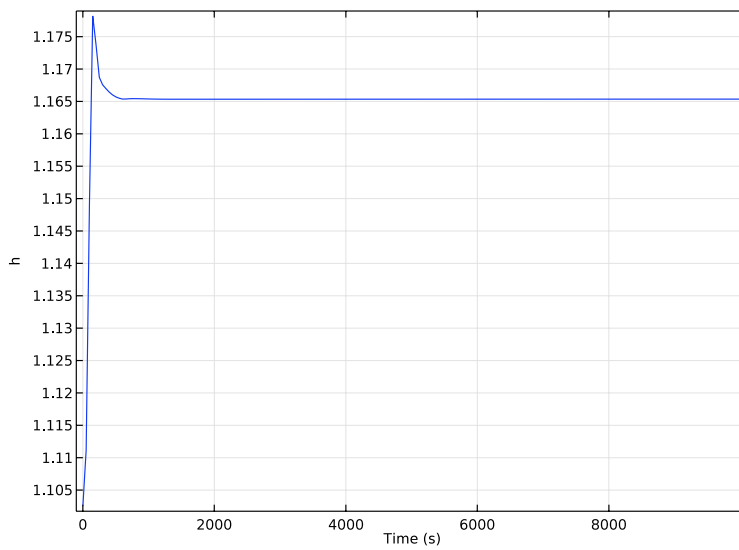
Figure 3.8: Plots of the max film thickness $h(x, t)$ over domain x over time.
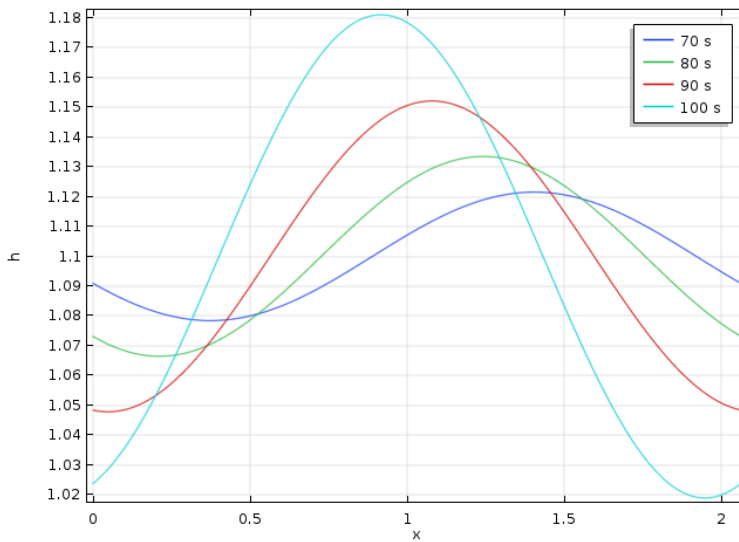
Figure 3.9: Plots of the solution $h(x, t)$ of the linearized system over domain x over time step 70 to 100
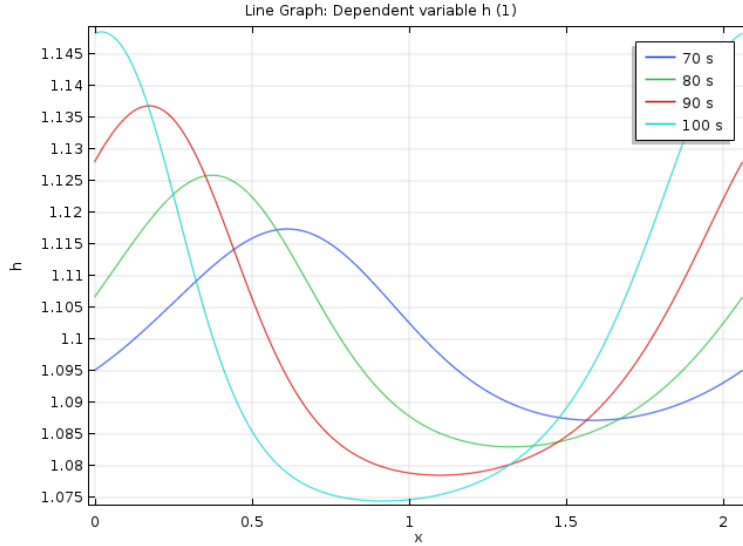
Figure 3.10: Plots of solution $h(x, t)$ over domain x over time step 70 to 100.

with a standard deviation of 0.5. The result shows that the initial Gaussian shape wave will form multiple waves that propagate at different speeds. The Wave height keeps increasing during the simulation. The film profile at different time steps are shown in Figure 3.11

Another type of simulation is shown in Figure 3.12. This case uses Dirichlet boundary conditions at the left and right ends, namely $h_l = 1.1$ and $h_r = 1.05$. We use a smoothed step function $s(x)$ built to smoothly connect h_l and h_r as the initial condition for h and the initial condition for u is set to $s(x)^2 - 1$. The simulation generates a similar pattern for the case with the Gaussian initial conditions.

Simulations under different initial conditions form similar shape film profiles at long times. The wave profile shown in Figure 3.13 is extracted from a simulation run to $t = 3000$ with an initial condition set as $h_0 = 1.1 + 0.1g(x)$, where $g(x)$ is a Gaussian function with $\mu = 5$ and $\sigma = 0.5$.

3.6 Discussion

While most of the models describing films on a fiber assume laminar viscous flows, the model we derived here is primarily applicable under the assumption that the flows around the vertical fiber is a well-mixed turbulent flow with a plug-flow profile. To see whether this is physically feasible,
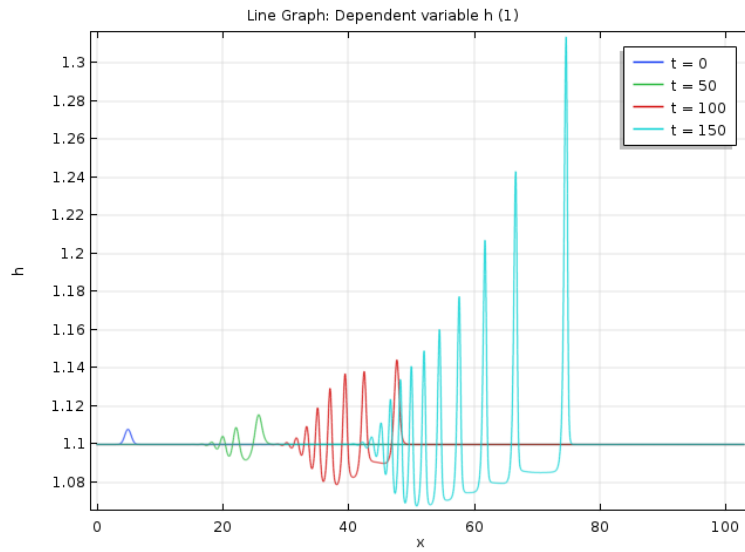
Figure 3.11: Plots of solution $h(x, t)$ over domain x over time step $0, 50, \cdots, 150$.
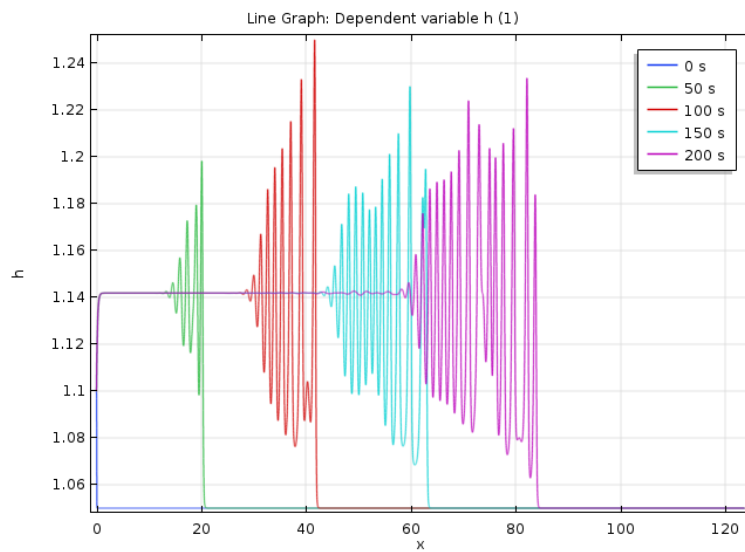
Figure 3.12: Plots of solution $h(x, t)$ over domain x over time step $0, 50, \cdots, 200$.
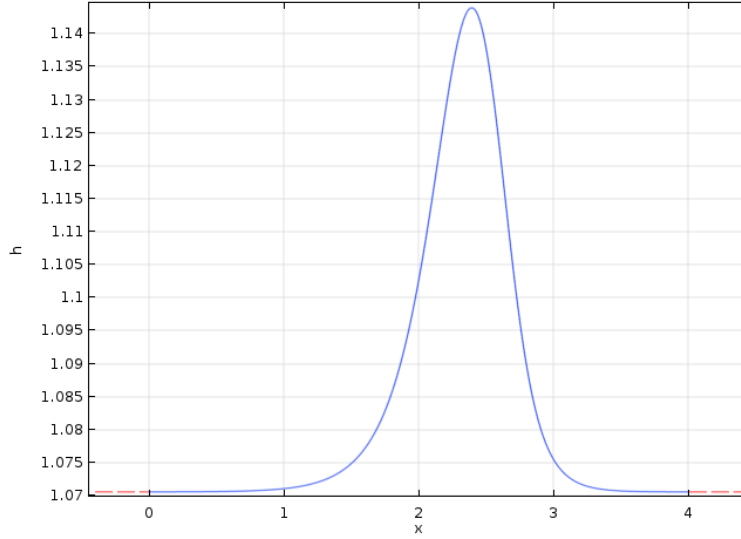
Figure 3.13: Plots of a droplet profile extracted from a solution at $t = 3000$.

assume that the fiber radius R is 2 mm and the film thickness $T = H - R$ is about the same size as the fiber radius. We can approximate the corresponding Reynolds number for the steady state flow of this type. The mean wall shear stress τ is expressed in terms of the Darcy–Weisbach friction factor f_D and average fluid velocity U as

$$\tau = \frac{1}{8} f_D \rho U^2$$

The force balance between the drag force from the wall and gravity gives us

$$2\pi R \tau = \rho g \pi ((R + T)^2 - R^2)$$

which can be solved to obtain $\tau = 78.4$ Pa (we take the density of water to be $\rho = 1000$ kg/m^3 and its viscosity to be $\mu = 0.001$ kg/(m s)). The Colebrook–White correlation for a smooth surface relates the friction factor to the Reynolds number by

$$\frac{1}{\sqrt{f_D}} = -2\log(\frac{2.51}{Re\sqrt{f_D}})$$

76

We substitute the expression for f_D in terms of τ and U, and $Re = \frac{\rho U T}{\mu}$ and obtain a transcendental equation for U, whose solution yields the mean velocity and corresponding Reynolds number as

$$U = 11.31 m/s, \quad Re = 45240.$$

The result shows that under some practical assumptions, the film flow on fiber could be in a turbulent regime. Under the assumptions above, the parameters a, b, c in our model would have values

$$a \approx 102, \quad b \approx 1.84, \quad c \approx 0.072.$$

Exploration of such turbulent regimes and their experimental investigations are left for future researchers.

3.7 Appendix

3.7.1 Derive the Film on Fiber Model Using Depth Averaging Method

In cylindrical coordinates, we have the divergence as

$$\nabla \cdot u = \frac{\partial u_z}{\partial z} + \frac{1}{r}\frac{\partial (r u_r)}{\partial r} + \frac{1}{r}\frac{\partial u_\theta}{\partial \theta}$$

Hence, the continuity equation for imcompressible fluid $\nabla \cdot \vec{u} = 0$ becomes

$$\frac{\partial u_z}{\partial z} + \frac{1}{r}\frac{\partial (r u_r)}{\partial r} + \frac{1}{r}\frac{\partial u_\theta}{\partial \theta} = 0$$

For axisymmetric flow, we have $\frac{\partial u_\theta}{\partial \theta} = 0$, then,

$$\frac{\partial u_z}{\partial z} + \frac{1}{r}\frac{\partial (r u_r)}{\partial r} = 0$$

Introduce dimensionless variables as

$$u_z = U_z \tilde{u}_z, \quad r = R\tilde{r}, \quad u_r = U_r \tilde{u}_r, \quad z = Z\tilde{z}$$

We have

$$\frac{U_z}{Z} \frac{\partial u_z}{\partial z} + \frac{U_r}{R} \frac{1}{r} \frac{\partial (r u_r)}{\partial r} = 0$$

Since continuity equation need to balance exact, we have

$$\frac{U_z}{Z} \sim \frac{U_r}{R}$$

Now from the z-component of Navier-Stokes equation, we have

$$\rho\left(\frac{\partial u_z}{\partial t} + u_r \frac{\partial u_z}{\partial r} + u_z \frac{\partial u_z}{\partial z}\right) = -\frac{\partial p}{\partial z} + \mu\left[\frac{1}{r} \frac{\partial}{\partial r}\left(r \frac{\partial u_z}{\partial r}\right) + \frac{\partial^2 u_z}{\partial z^2}\right] + \rho g_z$$

The scales for each term is

$$\rho\frac{U_z}{T}, \quad \rho\frac{U_r U_z}{R}, \quad \rho\frac{U_z^2}{Z}, \quad \frac{P}{Z}, \quad \frac{\mu U_z}{R^2}, \quad \frac{\mu U_z}{Z^2}, \quad \rho g$$

Here if we make assumptions that $\frac{R}{Z} \ll 1$, then $\frac{\mu U_z}{Z^2}$ terms will be dominated by $\frac{\mu U_z}{R^2}$. Selecting scale for T and P as below, we have,

$$T = \frac{Z}{U_z}, \quad P = \frac{\mu U_z Z}{R^2}$$

Since we want to keep the effect of gravity, then the scale for U_z is determined as

$$\frac{\mu U_z}{R^2} = \rho g \rightarrow U_z = \frac{\rho g R^2}{\mu}$$

Now the LHS scale is

$$LHS_{scale} = \rho\frac{U_z^2}{Z}, \quad RHS_{scale} = \frac{\mu U_z}{R^2}$$

So we have

$$\frac{LHS_{scale}}{RHS_{scale}} = \frac{\rho U_z Z}{\mu}\epsilon^2 = \epsilon^2 Re_Z$$

Let $\alpha := \epsilon^2 Re_Z$, we have the equation becomes

$$\alpha\left(\frac{\partial u_z}{\partial t} + u_r \frac{\partial u_z}{\partial r} + u_z \frac{\partial u_z}{\partial z}\right) = -\frac{\partial p}{\partial z} + \frac{1}{r} \frac{\partial}{\partial r}\left(r \frac{\partial u_z}{\partial r}\right) + 1$$

78

From the r-component of Navier-Stokes equation, we have,

$$\rho\left(\frac{\partial u_r}{\partial t} + u_r\frac{\partial u_r}{\partial r} - \frac{u_\theta^2}{r} + u_z\frac{\partial u_r}{\partial z}\right) = -\frac{\partial p}{\partial r} + \mu\left[\frac{\partial}{\partial r}\left(\frac{1}{r}\frac{\partial}{\partial r}(ru_r)\right) + \frac{\partial^2 u_r}{\partial z^2}\right]$$

Since $U_r = \frac{R}{Z}U_z = \epsilon U_z$, then $\frac{\partial p}{\partial r}$ terms scale would be

$$\frac{P}{R} = \frac{PZ}{RZ} = \frac{P}{Z\epsilon}$$

And all terms on the LHS would be ϵ times the scale smaller than scale of $\frac{P}{Z}$, the second terms on the right would dominate the third terms, and its scale is

$$\mu\frac{U_z}{ZR} = \mu\frac{U_z}{R^2}\epsilon$$

Hence, from the assumptions we used when nondimensionlize z-component of NS, we have, the terms except pressures on r-component NS can be ignored. Hence, we have

$$\frac{\partial p}{\partial r} = 0$$

In summary, we have

$$\alpha\left(\frac{\partial u_z}{\partial t} + u_r\frac{\partial u_z}{\partial r} + u_z\frac{\partial u_z}{\partial z}\right) = -\frac{\partial p}{\partial z} + \frac{1}{r}\frac{\partial}{\partial r}\left(r\frac{\partial u_z}{\partial r}\right) + 1 \tag{3.9}$$

$$\frac{\partial u_z}{\partial z} + \frac{1}{r}\frac{\partial(ru_r)}{\partial r} = 0 \tag{3.10}$$

$$\frac{\partial p}{\partial r} = 0 \tag{3.11}$$

where $\alpha := \epsilon^2 Re_Z$.

Now we need to determine the pressure term p, consider the normal stress balance on liquid-air interface, we have

$$\vec{n} \cdot \left[\pi_{air} - \pi_{liquid}\right] \cdot \vec{n} = \sigma\left(\frac{1}{R_1} + \frac{1}{R_2}\right)$$

where R_1, R_2 are the principal radii of curvature and π_{air}, π_{liquid} is stress tensor corespondingly. Let $h(z,t)$ denote the fluid locations (fluid thickness plus fiber raduis R), From normal stress balance,

we have

$$\frac{2\mu}{1+(\frac{\partial h}{\partial z})^2}[\frac{\partial h}{\partial z}(\frac{\partial u_z}{\partial r} + \frac{\partial u_r}{\partial z}) - \frac{\partial u_r}{\partial r} - \frac{\partial u_z}{\partial z}(\frac{\partial h}{\partial z})^2] + p = \frac{-\sigma\frac{\partial^2 h}{\partial z^2}}{(1+(\frac{\partial h}{\partial z})^2)^{\frac{3}{2}}}$$

Let film thickness has characteristic height H, then $h = (H + R)\tilde{h}$, assume that $\frac{H}{Z} \ll 1$ we have the scale for each terms are

$$\mu\frac{U_z}{Z}\frac{R+H}{R}, \quad \mu\frac{U_z}{Z}\frac{R(R+H)}{Z^2}, \quad \mu\frac{U_r}{R} = \frac{\mu U_z}{z}, \quad \frac{\mu U_z(R+H)^2}{Z^3} = \frac{\mu U_z}{z}(\frac{H+R}{Z})^2, \quad P, \quad \frac{\sigma(R+H)}{Z^2}$$

Now if we assume film thickness and fiber radius is about the same scale, then $R = H$, scales above simplified to

$$\mu\frac{U_z}{Z}, \quad \mu\frac{U_z}{Z}\frac{R^2}{Z^2}, \quad \mu\frac{U_r}{R} = \frac{\mu U_z}{z}, \quad \frac{\mu U_z(R+H)^2}{Z^3} = \frac{\mu U_z}{z}(\frac{R}{Z})^2, \quad P, \quad \frac{\sigma R}{Z^2}$$

From previous steps we have determined the pressure scale as

$$\frac{\mu U_z Z}{R^2} = \frac{\mu U_z}{Z}\frac{Z^2}{R^2} = \frac{\mu U_z}{Z}\frac{1}{\epsilon^2}$$

Hence, all terms on the left except pressure can be ignored, we arrive at

$$p = -\sigma(-\frac{1}{h} + \frac{\partial^2 h}{\partial z^2})$$

Introduce parameter $\sigma = \beta\hat{\sigma}$, This require

$$\frac{\mu U_z}{Z}\frac{1}{\epsilon^2} = 2\frac{\beta\sigma R}{Z^2} = \frac{\beta\sigma}{Z}\epsilon \rightarrow \frac{\mu U_z}{\sigma} = \beta\epsilon^3$$

Plug this into the set of equations, we have

$$\alpha(\frac{\partial u_z}{\partial t} + u_r\frac{\partial u_z}{\partial r} + u_z\frac{\partial u_z}{\partial z}) = \beta(\frac{1}{h^2}\frac{\partial h}{\partial z} + \frac{\partial^3 h}{\partial z^3}) + \frac{1}{r}\frac{\partial}{\partial r}(r\frac{\partial u_z}{\partial r}) + 1 \tag{3.12}$$

$$\frac{\partial u_z}{\partial z} + \frac{1}{r}\frac{\partial(ru_r)}{\partial r} = 0 \tag{3.13}$$

where $\alpha := \epsilon^2 Re_Z, \quad \beta = \frac{\mu U_z}{\sigma\epsilon^3} = \frac{Ca_Z}{\epsilon^3}$.

Now consider fiber radius $r_0 = R$, under the scale R, we have $r_0 = 1$, and let

$$\langle u_z \rangle := \int_{r_0}^{h} u_z r dr = \int_{r_0}^{h} u_z r dr$$

Integrate over continuity equation by $\int_{r_0}^{h} u_z r dr$, we have,

$$\frac{\partial}{\partial z} \int_{r_0}^{h} u_z r dr - (u_z r)|_h \frac{\partial h}{\partial z} + \int_{r_0}^{h} \frac{\partial (r u_r)}{\partial r} dr = 0$$

using new variables $\langle u_z \rangle$ and kinematic BC: $u_r|_h = \frac{\partial h}{\partial t} + \frac{\partial h}{\partial z} u_z|_h$, we have

$$\frac{\partial \langle u_z \rangle}{\partial z} + h \frac{\partial h}{\partial t} = 0$$

Now integrate over NS equations, we have

$$\int_{r_0}^{h} \alpha \left(\frac{\partial u_z}{\partial t} + u_r \frac{\partial u_z}{\partial r} + u_z \frac{\partial u_z}{\partial z} \right) dr = \int_{r_0}^{h} \frac{\partial^3 h}{\partial z^3} + \frac{1}{r} \frac{\partial}{\partial r} \left(r \frac{\partial u_z}{\partial r} \right) + 1 dr$$

First term on the left, we have

$$\int_{r_0}^{h} \alpha \frac{\partial u_z}{\partial t} r dr = \alpha \left(\frac{d}{dt} \int_{r_0}^{h} u_z r dr - h u_z|_h \frac{\partial h}{\partial t} \right) = \alpha \frac{\partial \langle u_z \rangle}{\partial t} - \alpha h u_z|_h \frac{\partial h}{\partial t}$$

Second terms

$$\int_{r_0}^{h} \alpha u_r \frac{\partial u_z}{\partial r} r dr = \alpha h u_z|_h \left(\frac{\partial h}{\partial t} + \frac{\partial h}{\partial z} u_z|_h \right) + \frac{\alpha}{2} \int_{r_0}^{h} \frac{\partial u_z^2}{\partial z} r dr$$

Third terms

$$\int_{r_0}^{h} \alpha u_z \frac{\partial u_z}{\partial z} r dr = \frac{\alpha}{2} \int_{r_0}^{h} \frac{\partial u_z^2}{\partial z} r dr$$

To sum up the LHS, we have,

$$\alpha \left(\frac{\partial \langle u_z \rangle}{\partial t} + h(u_z|_h)^2 \frac{\partial h}{\partial z} + \int_{r_0}^{h} \frac{\partial u_z^2}{\partial z} r dr \right) = \alpha \left(\frac{\partial \langle u \rangle}{\partial t} + h(u_z|_h)^2 \frac{\partial h}{\partial z} + \frac{\partial \langle u_z^2 \rangle}{\partial z} - h \frac{\partial h}{\partial z} u_z^2|_h \right) = \alpha \left(\frac{\partial \langle u \rangle}{\partial t} + \frac{\partial \langle u_z^2 \rangle}{\partial z} \right)$$

Now we deal with terms on the RHS, first term,

$$\int_{r_0}^{h} \frac{\partial^3 h}{\partial z^3} r dr = \frac{\beta}{2} \left(\frac{1}{h^2} \frac{\partial h}{\partial z} + \frac{\partial^3 h}{\partial z^3} \right) (h^2 - r_0^2)$$

81

Second term,

$$\int_{r_0}^{h} \frac{\partial}{\partial r}(r\frac{\partial u_z}{\partial r})dr = -r_0\frac{\partial u_z}{\partial r}|_{r_0}$$

Third term,

$$\int_{r_0}^{h} rdr = \frac{1}{2}(h^2 - r_0^2)$$

To sum up the RHS, we have,

$$\frac{\beta}{2}(\frac{1}{h^2}\frac{\partial h}{\partial z} + \frac{\partial^3 h}{\partial z^3})(h^2 - r_0^2) - r_0\frac{\partial u_z}{\partial r}|_{r_0} + \frac{1}{2}(h^2 - r_0^2)$$

Hence, the equation becomes

$$\alpha(\frac{\partial \langle u_z \rangle}{\partial t} + \frac{\partial \langle u_z^2 \rangle}{\partial z}) = \frac{\beta}{2}(\frac{1}{h^2}\frac{\partial h}{\partial z} + \frac{\partial^3 h}{\partial z^3})(h^2 - r_0^2) - r_0\frac{\partial u_z}{\partial r}|_{r_0} + \frac{1}{2}(h^2 - r_0^2) \qquad (3.14)$$

$$\frac{\partial \langle u_z \rangle}{\partial z} + h\frac{\partial h}{\partial t} = 0 \qquad (3.15)$$

The part remain unknown is

$$u_z^2|_h, \quad u_z|_h \quad \frac{\partial u_z}{\partial r}|_{r_0}, \quad \langle u_z^2 \rangle$$

We derive an approximated expression for those terms from a fully developed flow model.

3.7.2 Fully developed flow on fiber

For fully developed flow, we have,

$$u_r = 0, \quad u_\theta = 0, \quad \frac{\partial u_z}{\partial t} = 0$$

Then continuity and NS equation reduce to

$$\frac{\partial u_z}{\partial z} = 0$$

$$-1 = \frac{1}{r}\frac{\partial}{\partial r}(r\frac{\partial u_z}{\partial r})$$

Rearrange we have,

$$\frac{\partial}{\partial r}(r\frac{\partial u_z}{\partial r}) = -r$$

82

Integrate with respect to r twice, we have,

$$u_z = -\frac{1}{4}r^2 + C_1 \log r + C_2$$

Since we have $u_z = 0$ at $r = r_0$, and $\frac{du_z}{dr} = 0$ at $r = h(z,t)$, plug in, we get

$$C_1 = \frac{h^2}{2}, \quad C_2 = \frac{1}{4}r_0^2 - \frac{h^2}{2}\log r_0$$

Under the proper scale, we also have $r_0 = 1$, hence, we have,

$$C_1 = \frac{h^2}{2}, \quad C_2 = \frac{1}{4}$$

Calculate flux $\langle u_z \rangle$, we have

$$\langle u_z \rangle = \frac{1}{16}\left(4h^4 \log(h) - 3h^4 + 4h^2 - 1\right)$$

expressing u_z in terms of $\langle u_z \rangle$, we have,

$$u_z = \langle u_z \rangle \frac{8h^2 \log(r) - 4r^2 + 4}{4h^4 \log h - 3h^4 + 4h^2 - 1} = f_1(r,h)\langle u_z \rangle$$

From this, we have

$$u_z|_h = f_1(h,h)\langle u_z \rangle$$

$$u_z^2|_h = f_1^2(h,h)\langle u_z \rangle^2$$

$$\frac{\partial u_z}{\partial r}\Big|_{r_0} = \frac{\partial f_1(r_0,h)}{\partial r}\langle u_z \rangle$$

$$\langle u_z^2 \rangle = \langle f_1^2(r,h) \rangle \langle u_z \rangle^2 = f_2(h)\langle u_z \rangle^2$$

$f_2(h) = \langle f_1^2(r,h) \rangle$, we leverage on symbolic calculations for the long expressions of f_1 and f_2.
Since $r_0 = 1$, both f_1, f_2 can be simplified to

$$f_1(r,h) = \frac{4\left(2h^2 \log(r) - r^2 + 1\right)}{4h^4 \log(h) - 3h^4 + 4h^2 - 1}$$

$$f_2(h) = \frac{4\left(24h^6 \log^2(h) - 36h^6 \log(h) + 17h^6 + 24h^4 \log(h) - 30h^4 + 15h^2 - 2\right)}{3\left(16h^8 \log^2(h) - 24h^8 \log(h) + 9h^8 + 32h^6 \log(h) - 24h^6 - 8h^4 \log(h) + 22h^4 - 8h^2 + 1\right)}$$

Now we plug those expression into our original equations, we have

$$\alpha\left(\frac{\partial \langle u_z \rangle}{\partial t} + \frac{\partial (f_2(h) \langle u_z \rangle^2)}{\partial z}\right) = \frac{\beta}{2}\left(\frac{1}{h^2}\frac{\partial h}{\partial z} + \frac{\partial^3 h}{\partial z^3}\right)(h^2 - r_0^2) - r_0 \frac{\partial f_1(r_0, h)}{\partial r}\langle u_z \rangle + \frac{1}{2}(h^2 - r_0^2) \quad (3.16)$$

$$\frac{\partial \langle u_z \rangle}{\partial z} + h\frac{\partial h}{\partial t} = 0 \quad (3.17)$$

where f_1 and f_2 has the expression we derived above.

3.7.3 COMSOL settings for long time simulation of droplets on fiber model

Here we attach the screenshots to show the COMSOL model inputs and settings.
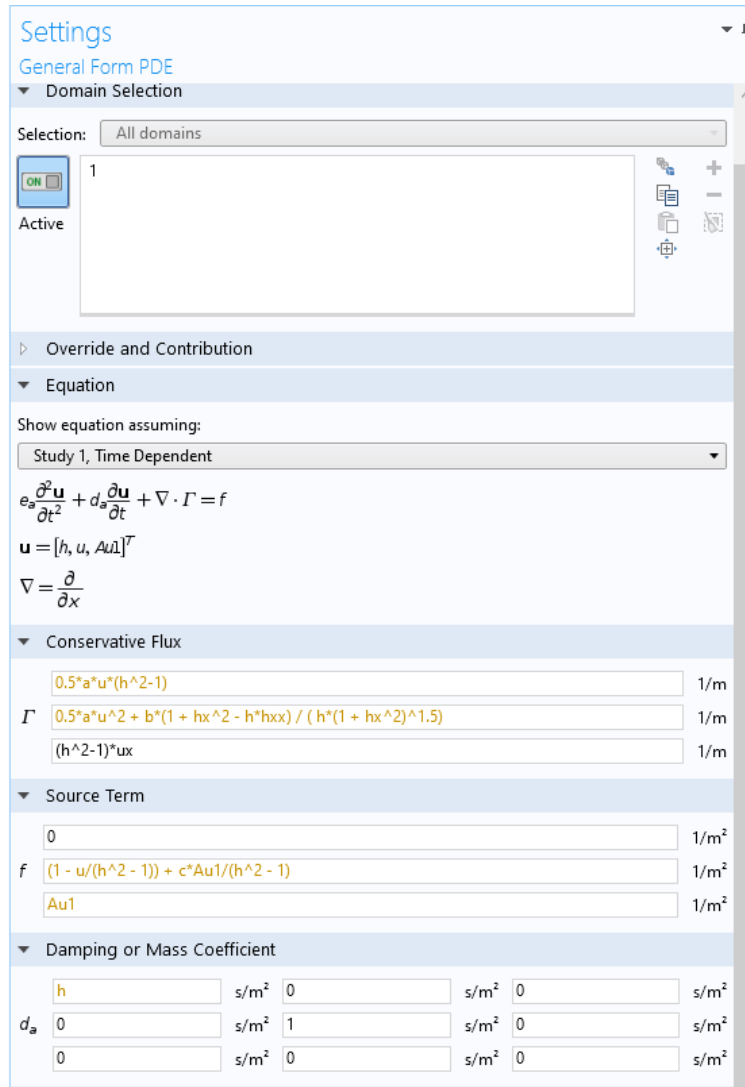
Figure 3.14: COMSOL model equation
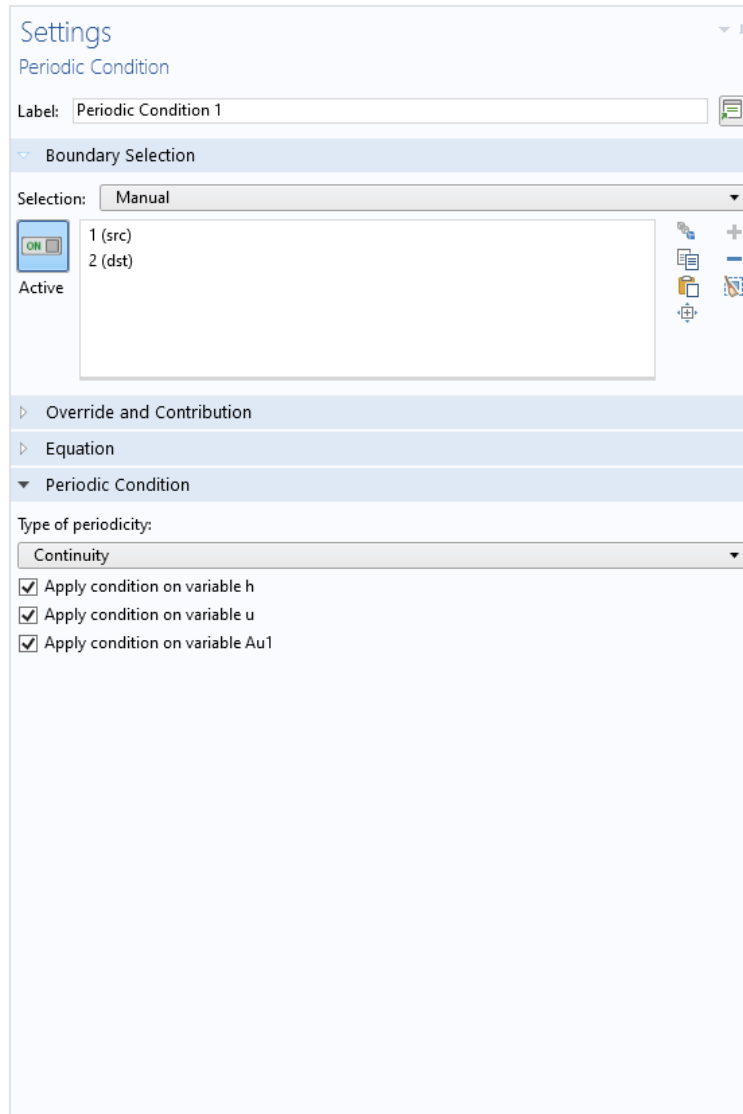
Figure 3.15: COMSOL model boundary conditions
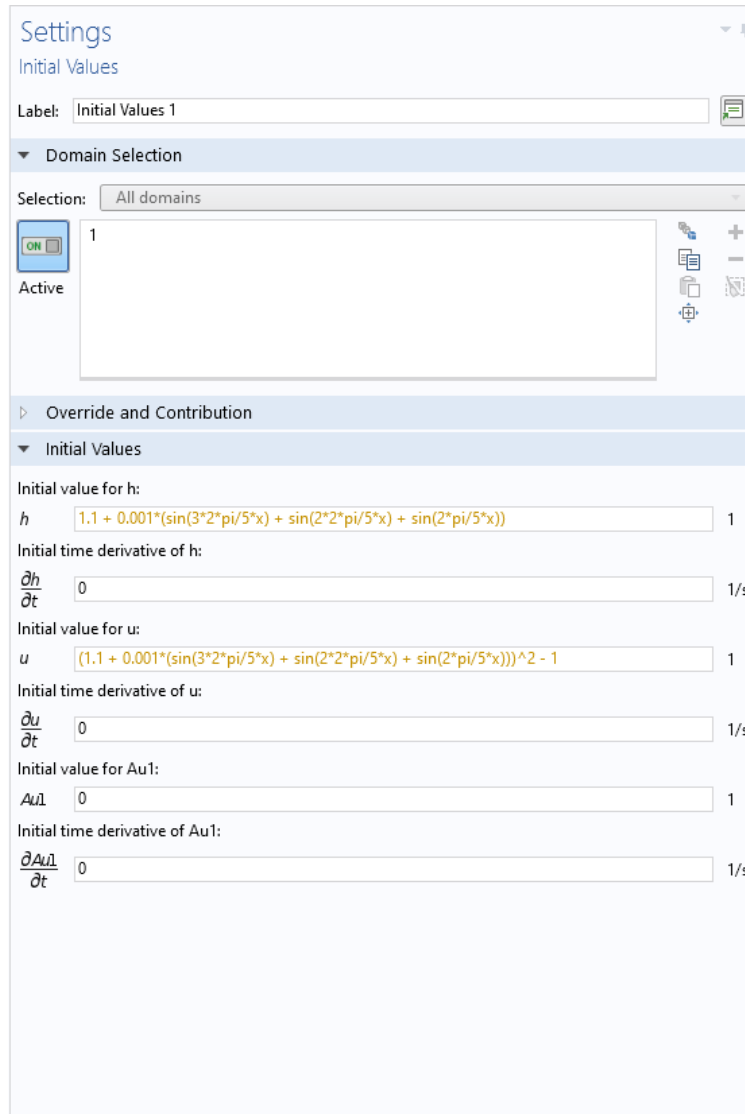
Figure 3.16: COMSOL model initial conditions
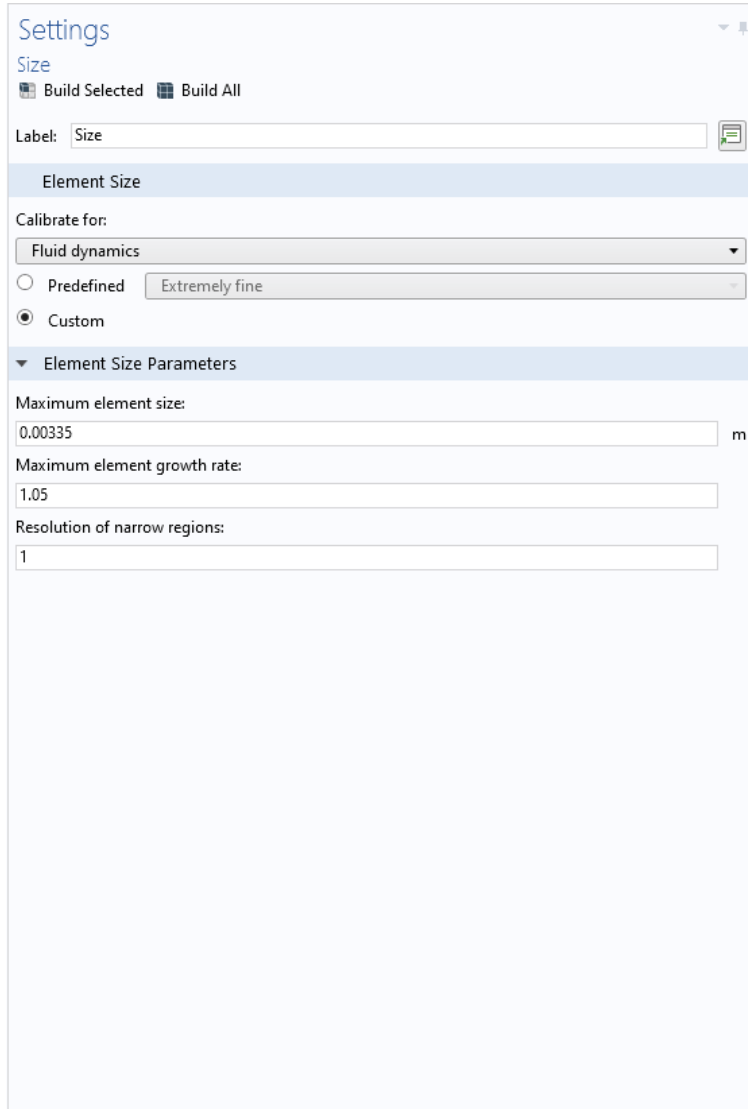
Figure 3.17: COMSOL model mesh setting

Figure 3.18: COMSOL model parameters
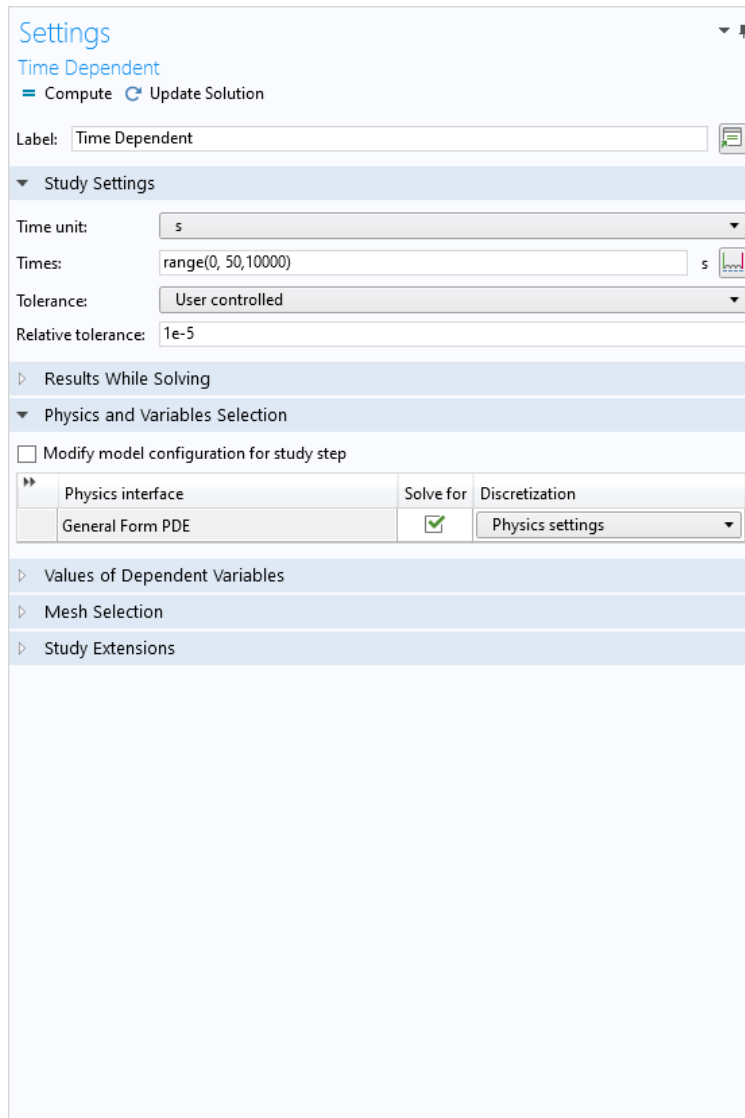
Figure 3.19: COMSOL model time dependent solver seeting

Chapter 4

Conclusions

In the first chapter of this thesis, we examined the dynamics of a thin film formed by a distributed liquid source on a vertical solid wall. The model was derived using the lubrication approximation and includes the effects of gravity, upward airflow and surface tension. When surface tension is neglected, a critical source strength is found below which the film flows entirely upward due to the airflow, and above which some of the flow is carried downward by gravity. In both cases, a steady state is established over the region where the finite source is located. Shock waves that propagate in both directions away from the source region are analysed. Numerical simulations are included to validate the analytical results. For models including surface tension, numerical simulations are carried out and the effects of surface tension is highlighted.

We then present several analytical results in chapter two for the thin film equation with source including existence of weak solutions, long-time behavior of solutions for the constant initial condition and qualitative behavior of solutions. The thin film equation with source can be treated as a simplified version of the model obtained in the first part.

Finally we consider a model for axisymmetric liquid film falling along a circular fiber. Recent experimental results have shown that as droplets form and vertically traverse the circular fibers, they fall into three unique regimes. Depending on nozzle diameter they appear as either uniformly distributed uniformly sized droplets, as large droplets separated by a series of small droplets, or as non-uniformly distributed non-uniformly sized droplets. In this thesis, we present and qualitatively analyze a mathematical model to supplement this experimental analysis, one capable of simulating (a) the convective regime where faster moving droplets collide with slower

moving ones for short to medium time scale, and then (b) Rayleigh-Plateau regime where stable traveling wave propagates without any collisions for long time simulations. Additionally, we study the linear stability of uniform fluid coatings for the fiber, and apply scientific computing tools to study their long-term dynamics.

Bibliography

[1] S George Bankoff. "Stability of liquid flow down a heated inclined plane". In: *International Journal of Heat and Mass Transfer* 14.3 (1971), pp. 377–385.

[2] E. Beretta, M. Bertsch, and R. Dal Passo. "Non-negative solutions of a fourth-order nonlinear degenerate parabolic equation". In: *Archive for Rational Mechanics and Analysis* 129.2 (1995), pp. 175–200.

[3] F. Bernis. "Finite speed of propagation and continuity of the interface for thin viscous flows". In: *Adv. Differential Equations* 1.3 (1996), pp. 337–368.

[4] F. Bernis and A. Friedman. "Higher order nonlinear degenerate parabolic equations". In: *J. Differential Equations* 83.1 (1990), pp. 179–206.

[5] F. Bernis, L. A. Peletier, and S. M. Williams. "Source type solutions of a fourth order nonlinear degenerate parabolic equation". In: *Nonlinear Analysis, Theory, Methods and Applications* 18.3 (1992), pp. 217–234.

[6] A. L. Bertozzi and M. Pugh. "The lubrication approximation for thin viscous films: regularity and long-time behavior of weak solutions". In: *Comm. Pure Appl. Math* 49.2 (1996), pp. 85–123.

[7] Andrea Bertozzi, A Munch, and Michael Shearer. "Undercompressive Shocks in Thin Film Flows". In: *Physica D: Nonlinear Phenomena* 134 (June 1999). DOI: 10.1016/S0167-2789(99)00134-7.

[8] J. F. Blowey, J. R. King, and S. Langdon. "Small- and waiting-time behavior of the thin-film equation". In: *SIAM Journal on Applied Mathematics* 67.6 (2007), pp. 1776–1807.

[9]   MG Blyth and C Pozrikidis. "Film flow down an inclined plane over a three-dimensional obstacle". In: *Physics of Fluids* 18.5 (2006), p. 052104.

[10]   V Bontozoglou and G Papapolymerou. "Laminar film flow down a wavy incline". In: *International journal of multiphase flow* 23.1 (1997), pp. 69–79.

[11]   Neima Brauner and David Moalem Maron. "Characteristics of inclined thin films, waviness and the associated mass transfer". In: *International Journal of Heat and Mass Transfer* 25.1 (1982), pp. 99–110.

[12]   E. A. Carlen and S. Ulusoy. "An entropy dissipation-entropy estimate for a thin film type equation". In: *Communications in Mathematical Sciences* 3.2 (2005), pp. 171–178.

[13]   E. A. Carlen and S. Ulusoy. "Asymptotic equipartition and longtime behavior of solutions of a thin-film equation". In: *Journal of Differential Equations* 241.2 (2007), pp. 279–292.

[14]   J. A. Carrillo and G. Toscani. "Long-Time Asymptotics for Strong Solutions of the Thin Film Equation". In: *Communications in mathematical physics* 225.3 (2002), pp. 551–571.

[15]   Hsueh-Chia Chang and Evgeny A. Demekhin. "Mechanism for drop formation on a coated vertical fibre". In: *Journal of Fluid Mechanics* 380 (1999), pp. 233–255.

[16]   Po-Jen Cheng, Cha'o-Kuang Chen, and Hsin-Yi Lai. "Nonlinear Stability Analysis of Thin Viscoelastic Film Flow Traveling Down along a Vertical Cylinder". In: *Nonlinear Dynamics* 24.3 (Mar. 2001), pp. 305–332. ISSN: 1573-269X. DOI: 10.1023/A:1008304906043. URL: https://doi.org/10.1023/A:1008304906043.

[17]   Po-Jen Cheng, Hsin-Yi Lai, and Cha'o-Kuang Chen. "Stability analysis of thin viscoelastic liquid film flowing down on a vertical wall". In: *Journal of Physics D: Applied Physics* 33.14 (2000), p. 1674.

[18]   M. Chugunova, J. R. King, and R. M. Taranets. "Uniqueness of the regular waiting-time type solution of the thin film equation". In: *European Journal of Applied Mathematics* 23.4 (2012), pp. 537–554.

[19]   M. Chugunova and R. M. Taranets. "New dissipated energy for non-negative weak solution of unstable thin-film equations". In: *Communications in Pure and Applied Analysis* 10.2 (2011), pp. 613–624.

[20] R. V. Craster and O. K. Matar. "On viscous beads flowing down a vertical fibre". In: *Journal of Fluid Mechanics* 553 (2006), pp. 85–105.

[21] LA Dávalos-Orozco. "Nonlinear instability of a thin film flowing down a smoothly deformed surface". In: *Physics of Fluids* 19.7 (2007), p. 074103.

[22] Luis A Dávalos-Orozco. "Instabilities of thin films flowing down flat and smoothly deformed walls". In: *Microgravity Science and Technology* 20.3-4 (2008), pp. 225–229.

[23] BR Duffy and HK Moffatt. "A similarity solution for viscous source flow on a vertical plane". In: *European Journal of Applied Mathematics* 8.1 (1997), pp. 37–47.

[24] S. D. Èĭdel'man. *Parabolic systems*. London. North-Holland Publishing Co., Amsterdam: Translated from the Russian by Scripta Technica, 1969.

[25] Mohamed S El-Genk and Hamed H Saber. "Minimum thickness of a flowing down liquid film on a vertical surface". In: *International Journal of Heat and Mass Transfer* 44.15 (2001), pp. 2809–2825.

[26] J. Fischer. "Optimal lower bounds on asymptotic support propagation rates for the thin-film equation". In: *J. Differ. Equ* 255.10 (2013), pp. 3127–3149.

[27] J. Fischer. "Upper bounds on waiting times for the thin-film equation: the case of weak slippage". In: *Archive for Rational Mechanics and Analysis* 211.3 (2014), pp. 771–818.

[28] A. L. Frenkel. "Nonlinear theory of strongly undulating thin films flowing down vertical cylinders". In: *EPL (Europhysics Letters)* 18 (1992), p. 7.

[29] L. Giacomelli and G. Günther. "Lower bounds on waiting times for degenerate parabolic equations and systems". In: *Interfaces and Free Boundaries* 8.1 (2006), pp. 111–129.

[30] L. Giacomelli and F. Otto. "Variatonal Formulation For The Lubrication Approximation Of The Hele-Shaw Flow". In: *Calculus of Variations* 13 (2001), pp. 377–403.

[31] H. P. Greenspan. "On the motion of a small viscous droplet that wets a surface". In: *Journal of Fluid Mechanics* 84.1 (1978), pp. 125–143.

[32] T Hayat, R Ellahi, and FM Mahomed. "Exact solutions for thin film flow of a third grade fluid down an inclined plane". In: *Chaos, Solitons & Fractals* 38.5 (2008), pp. 1336–1341.

[33] FJ Higuera. "Steady creeping flow down a slope". In: *Physics of Fluids* 7.11 (1995), pp. 2918–2920.

[34] H. Ji et al. "Dynamics of thin liquid films on vertical cylindrical fibres". In: *J. Fluid Mech* 865 (2019), pp. 303–327.

[35] H. Ji et al. "Modeling film flows down a fibre influenced by nozzle geometry". In: *Journal of Fluid Mechanics* 901 (Oct. 2020).

[36] Serafim Kalliadasis and Hsueh-Chia Chang. "Drop formation during coating of vertical fibres". In: *Journal of Fluid Mechanics* 261 (1994), pp. 135–168.

[37] I. L. Kliakhandler, S. H. Davis, and S. G. Bankoff. "Viscous beads on vertical fibre". In: *J. Fluid Mech* 429 (2001), pp. 381–390.

[38] William B Krantz and SL Goren. "Stability of thin liquid films flowing down a plane". In: *Industrial & Engineering Chemistry Fundamentals* 10.1 (1971), pp. 91–101.

[39] Hai Lan et al. "Developing laminar gravity-driven thin liquid film flow down an inclined plane". In: *Journal of Fluids Engineering* 132.8 (2010), p. 081301.

[40] John R Lister. "Viscous flows down an inclined plane from point and line sources". In: *Journal of Fluid Mechanics* 242 (1992), pp. 631–653.

[41] J. L. Marzuola, S. R. Swygert, and R. Taranets. "Nonnegative weak solutions of thin-film equations related to viscous flows in cylindrical geometries". In: *Journal of Evolution Equations* (2019). URL: https://doi.org/10.1007/s00028-019-00553-1.

[42] S Miladinova, G Lebon, and E Toshev. "Thin-film flow of a power-law liquid falling down an inclined plate". In: *Journal of non-Newtonian fluid mechanics* 122.1-3 (2004), pp. 69–78.

[43] AA Nepomnyashchii. "Stability of wavy conditions in a film flowing down an inclined plane". In: *Fluid Dynamics* 9.3 (1974), pp. 354–359.

[44] S. B. G. O'Brien and Leonard W. Schwartz. "Theory and modeling of thin film flows". In: *Encyclopedia of surface and colloid science* 1 (2002), pp. 5283–5297.

[45] A. Oron, S. H. Davis, and S. G. Bankoff. "Long-scale evolution of thin liquid films Rev". In: *Mod. Phys* 69.3 (1997), pp. 931–980.

[46] CD Park and T Nosoko. "Three-dimensional wave dynamics on a falling film and associated mass transfer". In: *AIChE Journal* 49.11 (2003), pp. 2715–2727.

[47] R. Dal Passo, H. Garcke, and G. Grün. "On a fourth-order degenerate parabolic equation: global entropy estimates, existence, and qualitative behavior of solutions". In: *SIAM journal on mathematical analysis* 29.2 (1998), pp. 321–342.

[48] R. Dal Passo, L. Giacomelli, and G. Grün. " Waiting time phenomenon for thin film equations". In: *Ann. Scuola Norm. Sup. Pisa* 30.2 (2001), pp. 437–463.

[49] Carlos A Perazzo and Julio Gratton. "Steady and traveling flows of a power-law liquid over an incline". In: *Journal of non-newtonian fluid mechanics* 118.1 (2004), pp. 57–64.

[50] B. Reisfeld and S. G. Bankoff. "Non-isothermal flow of a liquid film on a horizontal cylinder". In: *Journal of Fluid Mechanics* 236 (1992), pp. 167–196.

[51] TR Roy. "On laminar thin-film flow along a vertical wall". In: *ASME J. Appl. Mech* 51 (1984), pp. 691–692.

[52] C. Ruyer-Quil et al. "Film flows down a fiber: Modeling and influence of streamwise viscous diffusion". In: *The European Physical Journal Special Topics* 166.1 (2009), pp. 89–92.

[53] C. Ruyer-Quil et al. "Modelling film flows down a fibre". In: *Journal of Fluid Mechanics* 603 (2008), pp. 431–462.

[54] A. Sadeghpour, Z. Zeng, and Y. S. Ju. "Effects of nozzle geometry on the fluid dynamics of thin liquid films flowing down vertical strings in the Rayleigh-Plateau regime". In: *Langmuir* 33 (2017), pp. 6292–6299.

[55] A. Sadeghpour et al. "Water vapor capturing using an array of traveling liquid beads for desalination and water treatment". In: *Science advances* 5 (2019), p. 4.

[56] I Mohammed Rizwan Sadiq and R Usha. "Thin Newtonian film flow down a porous inclined plane: stability analysis". In: *Physics of Fluids* 20.2 (2008), p. 022105.

[57] L. W. Schwartz and E. E. Michaelides. "Gravity flow of a viscous liquid down a slope with injection". In: *The Physics of fluids* 32.10 (1988), pp. 2739–2741.

[58] LW Schwartz, D Roux, and JJ Cooper-White. "On the shapes of droplets that are sliding on a vertical wall". In: *Physica D: Nonlinear Phenomena* 209.1-4 (2005), pp. 236–244.

[59]   Sanat A Shetty and Ramon L Cerro. "Spreading of liquid point sources over inclined solid surfaces". In: *Industrial & engineering chemistry research* 34.11 (1995), pp. 4078–4086.

[60]   D. Slepčev. "Linear stability of self-similar solutions of unstable thin-film equations". In: *Interfaces and free boundaries* 11.3 (2009), pp. 375–398.

[61]   D. Slepčev and M. Pugh. "Self-similar blowup of unstable thin-film equations ". In: *Indiana University Mathematics Journal* 54.6 (2005), pp. 1697–1738.

[62]   Linda B. Smolka. "Dynamics of a thermally driven film climbing the outside of a vertical cylinder". In: *Phys. Rev. E* 96 (4 Oct. 2017), p. 043107. DOI: 10.1103/PhysRevE.96.043107. URL: https://link.aps.org/doi/10.1103/PhysRevE.96.043107.

[63]   Heishichiro Takahama and Seizo Kato. "Longitudinal flow characteristics of vertically falling liquid films without concurrent gas flow". In: *International Journal of Multiphase Flow* 6.3 (1980), pp. 203–215.

[64]   R. Taranets and M. Chugunova. "Thin film flow dynamics on fiber nets". In: *Communications in Mathematical Sciences* 16.3 (2018), pp. 763–775.

[65]   Yu Trifonov et al. "Steady-state traveling waves on the surface of a viscous liquid film falling down on vertical wires and tubes". In: *AIChE journal* 38.6 (1992), pp. 821–834.

[66]   A. Tudorasku. "Lubrication approximation for thin viscous films: asymptotic behavior of non-negative solutions". In: *Communications in Partial Differential Equations* 32.7 (2007), pp. 1147–1172.

[67]   Thomas Ward et al. "Experimental study of gravitation effects in the flow of a particle-laden thin film on an inclined plane". In: *Physics of Fluids* 21.8 (2009), p. 083305.

[68]   A Wierschem and N Aksel. "Instability of a liquid film flowing down an inclined wavy plane". In: *Physica D: Nonlinear Phenomena* 186.3-4 (2003), pp. 221–237.